RADIAL POINT INTERPOLATION METHOD FOR

STATIC AND DYNAMIC ANALYSIS OF

THREE-DIMENSIONAL SOLIDS

HUANG HAI TAO

NATIONAL UNIVERSITY OF SINGAPORE

2005

RADIAL POINT INTERPOLATION METHOD FOR

STATIC AND DYNAMIC ANALYSIS OF

THREE-DIMENSIONAL SOLIDS

HUANG HAI TAO

(B. Eng. SJTU, China)

A THESIS SUBMITTED

FOR THE DEGREE OF MASTER OF ENGINEERING

DEPARTMENT OF MECHANICAL ENGINEERING

NATIONAL UNIVERSITY OF SINGAPORE

2005

Acknowledgement

When I am writing this acknowledgement, I have mixed feelings of regret and gratitude. Being a part-time student, I changed jobs three times and was assigned oversea for long time during the study in NUS. Between study and career, I weighted on the latter unfortunately. I feel regret to say that I did not contribute enough energy to this study even though being pushed by my supervisor, Associate Professor **Liu Gui-Rong** many times. This is exactly the reason why I have the strongest feeling of gratitude to Prof. Liu for his dedicated support, invaluable guidance, continuous encouragement and especially his magnanimity in the duration of this research project. I am astonished at so many papers he published, while I am still struggling for only one thesis. I think his wisdom and dedication to research will inspire me in my future jobs.

Many thanks are also given to Dr. **Lu Chun** and Dr. **Gu Yuan-Tong** for their helpful advices.

I am grateful to the National University of Singapore for granting me the part-time study in the Department of Mechanical Engineering.

TABLE OF CONTENTS

Summary

Meshfree methods have recently become attractive alternatives for mechanical simulations. Many MFree methods have been proposed and developed in order to overcome the drawbacks coming with finite element method, which is presently the most popular numerical tool for various kinds of engineering problems. Among all these MFree methods, Point Interpolation Method (PIM) proposed by Liu G.R. and Gu Y.T. (1999) has achieved remarkable progress and exhibited an outstanding performance due to its excellent numerical stability and easy imposition of boundary conditions. PIM has been successfully used to solve a wide range of engineering problems in two dimensions. The objective of this research project is to extend the application of Radial Point Interpolation Method (RPIM), the PIM based on radial basis functions, to those engineering problems with the nature of three-dimension. A complete 3D-RPIM analysis package, which includes pre-processor and post-processor, is developed using Fortran language, as the final product of this research project.

The project started from the RPIM 3D shape function formation, followed by incorporation of RPIM shape functions into the Galerkin weak form to formulate the system equations for 3D solids and ended with examples of RPIM application to some selected structural problems. The detail description for each part of work is as follows:

- The Point Interpolation Method (PIM) with radial-polynomial basis is employed to construct MFree shape functions using only field nodes scattered arbitrarily within each local domain without any predefined mesh to provide the connectivity among these nodes. RPIM is found to be numerically stable for both regular and irregular nodal distributions with the created shape functions possessing the Kronecker delta function property. Through the example of 3-D function fitting, it is shown that radial basis functions of EXP and MQ could be used in the RPIM formation to produce good fitting

quality, as long as the preferred ranges of shape parameters are used in the interpolation. It is concluded that shape functions with radial-polynomial basis that are obtained by PIM are qualified for the MFree analysis.

- RPIM shape functions are incorporated into the Galerkin procedure to formulate the analysis method for 3D solid mechanics. Numerical procedures to perform linear static analysis, modal analysis and transient dynamic analysis for 3D solids are developed in detail.

- The accuracy and efficiency of the RPIM solver are verified through static analyses of 3D solids, via patch test and a benchmark example of cantilever beam. It is found that various analysis parameters will affect the performance of RPIM to some extent. By a complete parametric study of all these factors, the preferred range of different analysis parameters is recommended.

- The excellent performance of RPIM is demonstrated again through the modal analysis and transient dynamic analysis of 3D solids, via the same benchmark example of cantilever beam. The Newmark method (constant-average acceleration method) is recommended for the various kinds of transient dynamic analysis after a comparison study among several direct integration schemes.

- Finally, the RPIM is shown to be of practical use through much more complex examples from industries. An advantage of RPIM to deal with inconsistent meshes is also demonstrated.

By comparing RPIM with FEM and other MFree methods, the main advantages of this technique are summarized as follows:

- It has an excellent numerical stability against the irregularity of nodes, with its solver being so robust that it has never failed to generate the analysis solution with desired accuracy provided that the correct input is given.

- Its performance is compatible or faster than that of FEM. Moreover, there is much room for RPIM to be improved on its numerical implementation.

- It supports the control of solution accuracy through the adjustment of different analysis parameters.

- It can handle the geometrical and physical complexity similar to FEM.

- It simplifies the model preparation by imposing the minimum requirements on the consistency and quality of integration cells (meshes).

It should be noted that 3D-RPIM is still under development and its potential has not yet been explored fully. With the future improvements on several aspects, the performance of RPIM will go beyond FEM.

Nomenclature

A	eigenvector
a, **b**	coefficient vector for basis functions
b	body force vector
B	strain matrix
C	damping matrix
D	material matrix
d_c	average nodal spacing
E	Young's modulus
f	frequency
f	local force vector
F	global force vector
G	overall structural damping coefficient
G	combined moment matrix
k	local stiffness matrix
K	global stiffness matrix
L	differential operator
L	Lagrangian functional
m	number of polynomial terms
m	local mass matrix
M	global mass matrix
n	number of nodes in local domain
N	shape matrix

P	point load
$\mathbf{P}_0$	polynomial moment matrix
P($\mathbf{x}$)	polynomial basis
P($\mathbf{x}$)	vector of polynomial basis
q	local displacement vector
Q	global displacement vector
r	distance
r_i	radius of influence domain
r_s	radius of support domain
$\mathbf{R}_0$	radial moment matrix
R($\mathbf{x}$)	radial basis
R($\mathbf{x}$)	vector of radial basis
t	surface traction
T	kinetic energy
u	displacement vector
U	strain energy
$\mathbf{u}_0$	vector of function values
W	work done by external forces
x, x, y, z	spatial coordinates
$\mathbf{x}_Q$	quadrature point
α, β	Newmark parameters
α_c, q	RBF shape parameters
α_i	influence domain size parameter
α_s	support domain size parameter
Δt	time step
ε	strain vector

$\varepsilon_x, \varepsilon_y, \varepsilon_z$	normal strains
$\gamma_{yz}, \gamma_{xz}, \gamma_{xy}$	shear strains
$\phi(x)$	shape function
$\boldsymbol{\Phi(x)}$	matrix of shape functions
Γ	domain boundary
λ	eigenvalue
ν	Poisson's ratio
ρ	material density
$\boldsymbol{\sigma}$	stress tensor
σ_{vm}	Von Mises stress
$\sigma_x, \sigma_y, \sigma_z$	normal stresses
$\tau_{yz}, \tau_{xz}, \tau_{xy}$	shear stresses
ω	circular frequency
Ω	domain
Π	total potential energy

List of Figures

List of Tables

Chapter 1 Introduction

1.1 Background

Virtually all phenomena in nature can be described as mathematical equations with the aid of the laws of physics. However, the analytical solution of these governing equations, most often differential equations relating various quantities of interest, is a formidable task. In such cases, approximate methods of analysis provide alternative means of finding solutions. Among these approximate methods, the finite element method (FEM) is the most powerful tool for the numerical solution of a wide range of engineering problems. In this method of analysis, a complex region defining a continuum is discretized into simple geometric shapes called finite elements. The material properties and the governing relationships are considered over these elements and expressed in terms of unknown values at element corners. An assembly process, duly considering the loading and constraints, results in a set of algebraic equations. Solution of these equations gives us the approximate behavior of the continuum.

With the increasing applications in different industries, the following shortcomings inherent in FEM are also becoming more and more evident.

- When handling large deformations, considerable accuracy is lost due to element distortions.

- It is difficult to simulate the crack growth with arbitrary paths that do not coincide with the original mesh lines of elements.

- It is difficult to simulate the breakage of material into a large number of fragments.

- It is difficult to solve the dynamic contact problems with moving boundary.

A close examination on these difficulties associated with FEM reveals that they are all related to the use of "element" or "mesh", which is the fundamental component of FEM. As long as elements or meshes are used in the numerical solution of the governing equations, the

above-mentioned troubles coming with FEM will remain. For example, some re-mesh approaches or adaptive mesh schemes have been proposed to deal with these troubles caused by FEM. Due to the dependence on elements or meshes as before, none of these modified methods could completely solve these problems for FEM without any negative side-effects. Moreover, meshing process in FEM is the most time-consuming part of the analysis and requires considerable effort from the analyst. Therefore, the idea of eliminating elements or meshes has evolved naturally and many element-free methods or meshless methods have been proposed. To avoid confusion, all these methods are categorized as meshfree (MFree) method hereafter.

MFree method is a numerical tool to transform the partial differential equations governing physical phenomena into a set of algebraic equations without use of elements and meshes. In MFree method, the problem domain is firstly represented by a set of nodes scattered within the domain and on its boundaries. Unlike FEM, these nodes will not be used to build elements. In other words, there is no connectivity between any two nodes. After the node generation, the approximate solution over a sub-domain which consists of a few nodes is assumed to be a combination of appropriately chosen interpolation functions and undetermined coefficients (usually nodal values). Then the algebraic relations among these undetermined coefficients are obtained by satisfying the governing equations in strong form or weak form over each sub-domain. Finally, these discrete algebraic relations are assembled into a set of algebraic equations for the whole problem domain.

MFree method has great potential to overcome the disadvantages of FEM. Because there is no mesh, hence no connectivity among nodes, adaptive schemes can be easily implemented. This gives flexibility to add and delete nodes whenever and wherever necessary. In stress analysis of solids, for example, additional nodes can be freely added in areas of stress concentration without providing their relationship with other existing nodes. In crack growth problems, one can easily put more nodes around the crack tip to capture the stress concentration with desired accuracy. In addition, the time spent for meshing in FEM can be

saved by use of MFree methods, thus the overall efficiency of analysis and simulation projects can be greatly improved.

1.2 Literature Review

Realizing the advantage and potential of MFree method, a lot of research efforts in computational mechanics have been devoted to it recently.

The earliest MFree method is Smooth Particle Hydrodynamics (SPH) based on an integral form of kernel interpolation (Lucy, 1977; Gingold and Monaghan, 1977). SPH discretizes the state of a system into arbitrarily distributed particles and then applies the kernel approximation techniques together with the strong form of governing equations.

MFree methods had not gained significant progress until Nayroles et al. (1992) used the Moving Least Squares (MLS) approximation to construct shape functions for their Diffuse Element Method (DEM).

Based on DEM, Belytschko et al. (1994) proposed and developed the Element Free Galerkin (EFG) method in which the MLS approximation was incorporated into the Galerkin procedure. In the EFG method, the problem domain is discretized into a set of scattered points. The MLS approximation is employed to construct shape functions over a group of points. A background cell structure is required to evaluate the integrals in the global Galerkin weak forms. Due to the need of background cells for integration, the EFG method is actually a "half" MFree method.

On the contrary, a "truly" MFree method called Meshless Local Petrov-Galerkin (MLPG) method was originated by Atluri and Zhu (1998). In this method, local weak form of the Petrov-Galerkin residual formulation is used together with the MLS approximation to generate the system equations without the need of a background mesh.

Since MFree methods are relative new compared with the well-developed finite element method, they still have some technical problems to be solved. For example, SPH method suffers from difficulties to enforce essential boundary conditions. The same problem also

happens on EFG method and MLPG method due to the use of MLS approximation. In order to ease the imposition of boundary conditions, the Point Interpolation Method (PIM) was proposed by Liu G.R. and Gu Y.T. (1999). In this method, the interpolation function using polynomial basis or radial basis is forced to pass through each node within the sub-domain. Algebraic relations among nodal values are then obtained by satisfying the weak form or local weak form of the governing equations over each sub-domain before the final assembly process. Because the shape functions created by PIM possess the Kronecker delta property, the imposition of essential boundary conditions is as easy as that in FEM.

In order to make Point Interpolation Method numerically stable for arbitrarily distributed points, two significant advances have been achieved over the past years. The first is the use of radial basis functions for the shape function construction (Wang and Liu, 2000). The second is the invention of a two-stage Matrix Triangularization Algorithm (MTA) (Liu G.R. and Gu Y.T., 2001), which can automatically exclude the nodes and the terms of polynomial basis to create a nonsingular moment matrix.

PIM has been successfully used to solve a wide range of engineering problems, such as static and free vibration analysis of thin plates (Liu G.R. and Chen X.L., 2001), static and dynamic analysis of thin beams (Gu Y.T. and Liu G.R., 2001), numerical analysis of Biot's consolidation process (Wang J.G. et al., 2002), static and frequency analysis of two-dimensional piezoelectric structures (Liu G.R. et al., 2002), incompressible flow simulation (Wu Y.L. and Liu G.R., 2003).

Table 1.1 Characteristics of Typical MFree Methods

Method	Interpolation Technique	Governing Equation
SPH	Integral representation	Strong form
EFG	MLS	Weak form
MLPG	MLS	Local weak form
PIM	Point interpolation	Weak form or local weak form

The characteristics of different MFree methods are summarized in Table 1.1 for clarity.

1.3 Objectives

As shown in the previous section, the Point Interpolation Method using radial basis functions, so-called Radial Point Interpolation Method (RPIM), has an excellent numerical stability and has been successfully tested by many examples in two-dimension. The main objective of this research project is to extend the application of RPIM to those engineering problems in three dimensions.

The ultimate goal of any numerical method is to become an efficient tool which is widely accepted and used by engineers from industries. Hence, another objective of this research project is to make the 3D-RPIM as user-friendly as FEM.

In order to achieve these two objectives, the following tasks are accomplished.

- Formulate the Radial Point Interpolation Method based on Galerkin weak form of governing equations for three-dimensional solids

- Develop the procedure to perform the static analysis for 3D solids using RPIM

- Develop the procedure to perform the modal analysis for 3D solids using RPIM

- Develop the procedure to perform the transient dynamic analysis for 3D solids using RPIM

- Fine-tune the analysis parameters of RPIM to achieve the desired accuracy and efficiency

- Develop the pre-processor and post-processor for the structural analysis of 3D solids using RPIM

1.4 Analysis Procedure of RPIM

Applications of MFree methods range from deformation and stress analysis for various kinds of structures to field analysis of heat flux, fluid flow, magnetic flux, seepage, and other flow problems. With the advances in computer technology and CAD system, complex problems can be modeled with relative ease. In this research project, static and dynamic

analyses for three-dimensional solids of complex shapes are used to demonstrate the basic

procedure of RPIM.

1.4.1 Geometry Modeling

With a help of commercial three-dimensional CAD systems like SolidWorks, any 3D

solid geometry with complex shapes can be easily created and used as the problem domain for

MFree analysis.

Actually FEM does this step in a similar way. The complicated solid model is drawn by

use of commercial CAD packages, and then exported to a file in a specific geometry format.

The popular geometry formats include ACIS solid model file format (*.SAT File), Parasolid

solid model format (*.X_T File), STEP, IGES, DXF and numerous CAD native formats.

Finally, this geometry file is imported into the pre-processor of FEM packages for subsequent

meshing process.

1.4.2 Node Generation

In MFree method, the solid geometry should be represented by a set of nodes scattered

inside its body and on its surfaces. This step is often called node generation. There is almost

no dedicated node generator available commercially. Fortunately, the pre-processor of many

commercial FEM packages can be used to do this job very well.

In FEM, meshing is performed to discretize the geometry into small elements that are

connected at nodes. The output of the meshing process includes the element connectivity data

and nodal-coordinate data. The latter is exactly what we want for the MFree methods. On the

contrary, the element connectivity data can be safely discarded at this stage. However, in this

research project, the elements are kept for other purposes also, such as stress contour plots.

There are two kinds of solid mesh in FEM – hexahedral mesh and tetrahedral mesh. Not

all solids are hex meshable, so the most important and difficult step in the hex meshing

process involves dividing the whole solid (often with complex shapes) into simple hex

meshable parts. In contrast, the tetrahedral mesh can be generated almost automatically for

solids with any complexity. However, the FEM results via tetrahedral mesh are very poor

because of the constant stress field within the element. In other words, a large number of tetrahedral elements are required to achieve the same accuracy as hexahedral mesh with much fewer elements.

Because the basic concept of MFree methods is not to use elements, the element shape used in the step of node generation will not affect the MFree results theoretically. Therefore, the MFree methods can take the full advantage of the automatic Tet-mesher to generate the nodes without losing any computational accuracy. In this research project, both Hex-mesher and Tet-mesher are used with the former for simple solids and the latter for complex solids.

1.4.3 Local Domain Construction

In FEM, the local algebraic equations are obtained by satisfying the governing equations, often in a weight-integral sense, over each element. For MFree methods, the formation of local algebraic equations has to be carried out over a group of nodes around each specific point because there is no element can be used. These nodes as a group can be called the local domain of a specific point. Actually the main task of local domain construction is to determine how many nodes and which nodes to be included in the local domain of each point of interest.

One simple way to carry out this process of node selection is to assume that each point has a support domain around it. All nodes fall inside its support domain are simply selected as its local domain. The support domain of a point is usually a ball centered at this point with the radius defined as

$$r_s = \alpha_s\, d_c \tag{1.1}$$

where α_s is the support domain size parameter and d_c is the average nodal spacing near the point. The bigger the support domain size parameter is, the more nodes are included in the local domain. Thus the value of support domain size parameter will greatly affect the efficiency and accuracy of MFree analysis. According to numerical experiments later, $\alpha_s = 1.5 \sim 2.0$ for MFree analysis using RPIM will generally yield the satisfactory results.

As shown in Equation (1.1), the average nodal spacing d_c should be evaluated first before we can get the size of support domain. In this research project, a simple method is used to estimate the average nodal spacing as

$$d_c = \frac{\sqrt[3]{V_s}}{\sqrt[3]{n_s} - 1} \qquad (1.2)$$

where V_s is an estimated volume that is covered by the support domain, and n_s is the number of nodes within the estimated volume.

The concept of support domain works well if the nodal density does not vary too drastically within the problem domain. Practically, it is possible that the nodal density does vary drastically, like solving problems with stress singularity, for example. In such cases, the use of support domain may lead to an unbalanced selection of nodes for the shape function construction. In the extreme, all the nodes selected could be located on one side relative to a point, and the shape functions based on this nodal distribution could result in serious error. To avoid errors caused by highly irregular nodal distribution, the concept of influence domain can be used.

The influence domain is defined as the extent of influence a node exerts. For a specific point of interest, all nodes with influence domains covering this point will be selected as the local domain of this point. The influence domain of a node is usually a ball centered at this node with the radius calculated as

$$r_i = \alpha_i \left(\frac{1}{n} \sum_{j=1}^{n} V_j \right)^{1/3} \qquad (1.3)$$

where α_i is the influence domain size parameter, n is the number of elements adjacent to the node, and V_j is the volume of each adjacent element. Normally the influence domain size for each node is computed immediately after the node generation as a by-product of the meshing process. The size of influence domain by this approach varies reasonably in accordance with the local nodal density. The higher the nodal density is, the smaller the influence domain size becomes. Therefore, nodes near the area of high nodal density are unlikely to be included in

the local domain of a specific point. On the contrary, nodes near an area of low nodal density

are likely to be selected due to bigger size of influence domain. By this way, unbalanced

nodal distribution within the local domain can be avoided.

Similar to the support domain size parameter, the value of influence domain size

parameter also affects the results of MFree analysis. This will be discussed in detail later.

Note that three types of domain have been mentioned here. They are support domain,

influence domain and local domain. As per discussion above, the influence domain goes with

a node, while the support domain and local domain go with a point of interest. The differences

among them will be illustrated by Figure 1.1 and Figure 1.2 below.
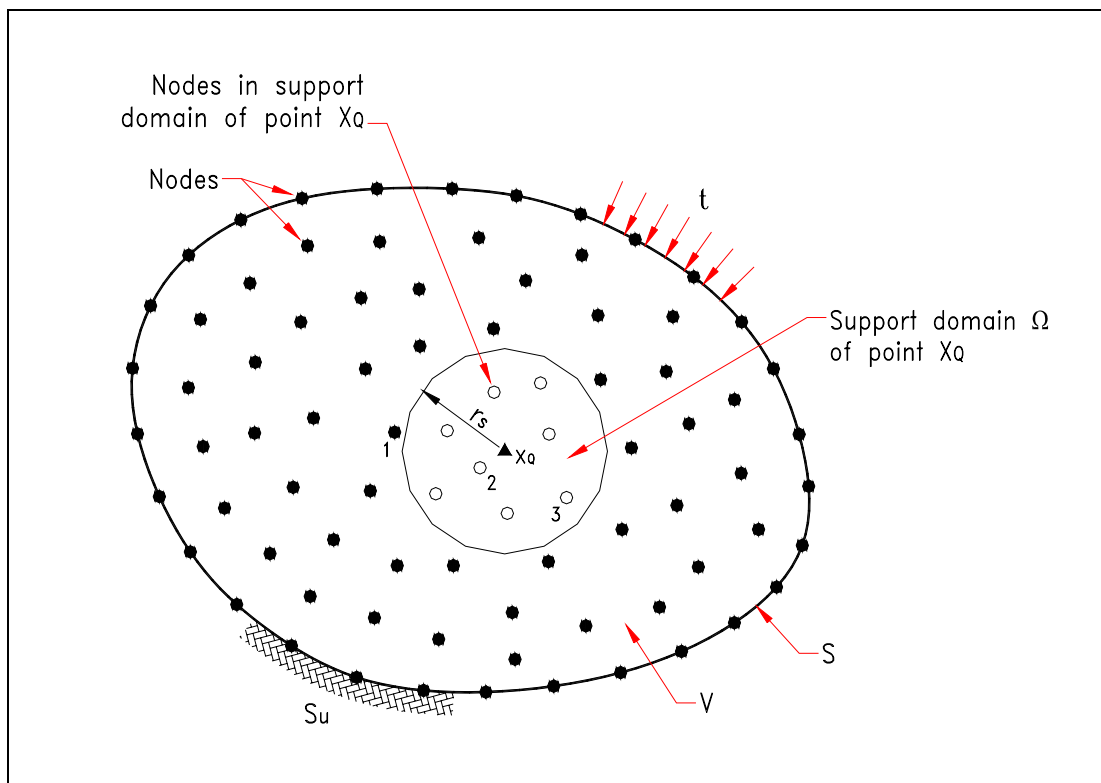
Figure 1.1 Local Domain Construction via Support Domain
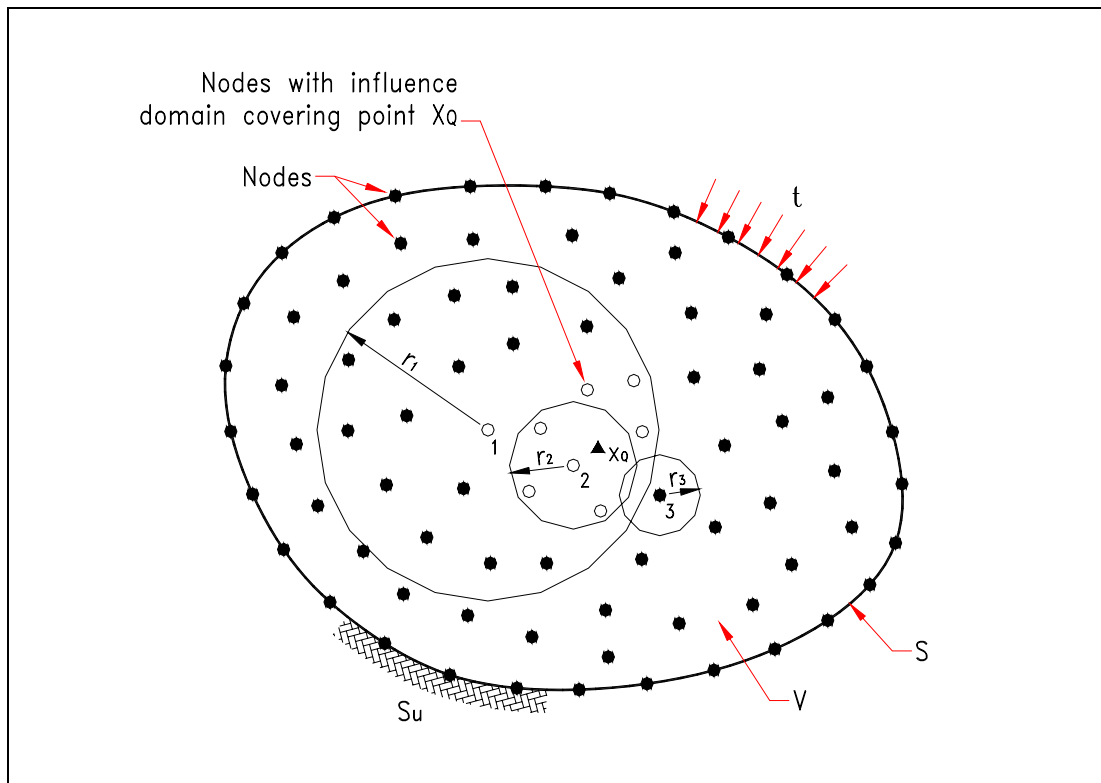
Figure 1.2 Local Domain Construction via Influence Domain

The Figure 1.1 shows the local domain construction for a point $\mathbf{x}_Q$ via the concept of support domain. Point $\mathbf{x}_Q$ has a support domain with radius of r_s. Nodes 2 & 3 are inside the support domain of $\mathbf{x}_Q$, while node 1 is not. So the nodes 2 & 3 are included in the local domain of point $\mathbf{x}_Q$ without node 1.

The Figure 1.2 shows the identical nodal distribution, but the local domain of the point $\mathbf{x}_Q$ is constructed via the concept of influence domain. Node 1 has an influence radius of r_1, node 2 has an influence radius of r_2 and so on. Node 1 & 2 have their influence domains cover the point $\mathbf{x}_Q$, so they are included in the local domain. On the contrary, node 3 is not included even though it is very close to the point $\mathbf{x}_Q$ actually.

Whichever method is used, the collection of nodes selected is called local domain of point $\mathbf{x}_Q$. In order to make our RPIM suitable for any nodal distributions, the concept of influence domain is always used by default in the stress analysis to construct the local domains for each point of interest.

It should be also mentioned that the Gauss quadrature points of all elements are chosen as the points of interest whose local domains to be constructed for the subsequent MFree process. In this research project, all the Gauss points are generated together with the nodes as another by-product of the meshing process.

1.4.4 Displacement Interpolation

After the construction of the local domain for a specific point, the displacement u at any point nearby is assumed to be a linear combination ($u = \sum_{i=1}^{n} u_i \phi_i$) of shape functions ϕ_i and displacement u_i at all n nodes within the local domain. The creation of shape functions is the most important difference between MFree methods and the traditional FEM. The way to formulate the shape function also distinguishes the different MFree methods. In this thesis, the construction of shape functions using RPIM is detailed in Chapter 2.

1.4.5 Formation of System Equations

In the solution of a partial differential equation by MFree Radial Point Interpolation Method, the equation is put into an equivalent weighted-integral form and the approximate solution (field displacement) over the local domain of a specific point is assumed to be a linear combination of shape functions and nodal displacements (as described in the previous step). After that, algebraic relations among the nodal displacements are obtained by satisfying the governing equations in the weighted-integral sense over the local domain of each point. Finally, these local algebraic relations for each point are assembled into the global system equations.

The global system equations are a set of algebraic equations for static analysis, eigenvalue equations for modal analysis, and differential equations with respect to time for general dynamic problems. The procedure for formation of system equations using RPIM is detailed in Chapter 3.

1.4.6 Solution of Global System Equations

For static analysis, the displacements at all nodes in the entire problem domain are firstly obtained by solving the global system equations using a standard subroutine for linear systems. The strains and stresses at all Gauss points and nodes can then be retrieved.

For modal analysis, the eigenvalues and corresponding eigenvectors of the system are obtained using a standard subroutine for eigen systems.

For transient dynamic analysis, the time histories of displacement, velocity and acceleration at all nodes are obtained using direct integration method.

1.4.7 Visualization of Analysis Results

The analysis results generated by MFree methods after solving the system equations are usually in a form of vast volume of digital data. It is not an easy job to interpret these data and verify the structural behavior of the system numerically. Similar to the step of node generation, the post-processor of commercial FEM packages can be used to present the MFree analysis results graphically. Typically, the deformation, mode shapes and stress contour of the 3D solids are displayed and captured at this stage.

For plots of deformation and mode shapes, the nodal displacements from MFree analysis results can be directly imported to the FEM post-processor and be displayed properly. For stress contour plot, additional data transformation is necessary. In FEM, stresses can be treated as a kind of attribute of elements, and they must be parasitized on elements. Hence the post-processor of FEM reads the stress results as a kind of elemental data, and displays the stress contour via the stress interpolation within each element. As we know, MFree methods are element free. In MFree methods, there is no element that can be used to display the stress contour. Therefore the stress results from MFree analysis have to be converted to a format which is readable by FEM post-processor.

As mentioned before, the results of stress and strain can be retrieved by MFree method at all Gauss points and nodes. It is theoretically and numerically sufficient to define the stress distribution within the problem domain, except that this stress distribution can not be

displayed by FEM post-processor. Here the mesh created at the step of node generation can give its contribution again. In this research project, the Von Mises stresses at all Gauss points within a specific element are averaged as per weights of Gauss points. This average Von Mises stress can be thought as the equivalent stress for that element, and can be imported to FEM post-processor for stress contour plots. In the following chapters, many stress contour plots are presented with the mesh lines being displayed also. It does not mean that MFree methods calculate the stresses via elements. The meshes (or elements) are just used to display the stress contour instead.

Another reason to present stress in this way is to facilitate the comparison with FEM. In the following chapters, FEM results are frequently used to verify the accuracy of MFree methods. If both MFree method and FEM can present their stress results in the same interface and in the same manner, it will make the comparison more straightforward.

1.4.8   Comparison with FEM

The comparison with FEM serves as an important evidence to verify the accuracy and efficiency of MFree RPIM. There are some well-known FEM packages available on the market. In this research project, the MSC-Nastran version 70.5 is always used, and all analysis runs by RPIM and Nastran are performed on the same computer with configuration as follows:

Model   Fujitsu C Series LifeBook

CPU   Inter Pentium III Mobile CPU 1133 MHz

RAM   256 MB

1.5   Organization of the Thesis

In Chapter 1, a brief historical background of MFree methods is given and the fundamental concepts of Radial Point Interpolation Method are introduced.

In Chapter 2, the procedure to construct MFree shape functions using RPIM is developed in detail. The quality of interpolation by RPIM is examined via examples of 3-D function fitting.

In Chapter 3, the formulation of stress analysis for 3D solids using RPIM is produced, and the numerical procedure for different types of analysis solutions is described step by step.

In Chapter 4 and 5, the accuracy and efficiency of RPIM are verified via static analysis and dynamic analysis of 3D solids respectively.

In Chapter 6, RPIM is proved to be of practical use through some real engineering examples. A technical advantage of 3D-RPIM to deal with mesh inconsistencies is demonstrated by the way.

In Chapter 7, conclusions of this project and recommendations for future research are given.

Chapter 2   RPIM Shape Function

In the MFree procedure, construction of shape functions using only field nodes scattered arbitrarily within each local domain without any predefined mesh to provide the connectivity among these nodes is the most important step where MFree methods differ from the traditional FEM principally.

The Point Interpolation Method (PIM) gets the approximation of a continuous function by forcing the interpolation function pass through each scattered node within a local domain. In this chapter, shape functions with radial-polynomial basis that are obtained by PIM are proved to be qualified for the MFree analysis.

2.1 PIM Formation using Radial-Polynomial Basis

Consider a continuous function u($\mathbf{x}$) defined in a domain Ω, which is represented by a set of field nodes. Radial PIM with polynomial basis can be employed to interpolate this function around a known point $\mathbf{x}_Q$ using the nodal values at the surrounding nodes that are referred to as the local domain of point $\mathbf{x}_Q$ collectively.

$$u(\mathbf{x}) = \sum_{i=1}^{n} R_i(\mathbf{x})a_i + \sum_{j=1}^{m} P_j(\mathbf{x})b_j = \mathbf{R}^T(\mathbf{x})\mathbf{a} + \mathbf{P}^T(\mathbf{x})\mathbf{b} \tag{2.1}$$

where a_i is the coefficient for the radial basis $R_i(\mathbf{x})$ and b_j is the coefficient for the polynomial basis $P_j(\mathbf{x})$. These basis functions are defined in the Cartesian coordinate space $\mathbf{x} = [x, y, z]^T$. n is the number of nodes in the local domain of point $\mathbf{x}_Q$, while m is the number of terms used for polynomial basis. Usually m < n.

Vectors shown in Equation (2.1) are defined as follows:

$$\mathbf{a} = [a_1, a_2, a_3, \cdots, a_n]^T \tag{2.2}$$

15

$$\mathbf{b} = [b_1, b_2, b_3, \cdots, b_m]^T$$

$$\mathbf{R}^T(\mathbf{x}) = [R_1(\mathbf{x}), R_2(\mathbf{x}), \cdots, R_n(\mathbf{x})]$$

$$\mathbf{P}^T(\mathbf{x}) = [P_1(\mathbf{x}), P_2(\mathbf{x}), \cdots, P_m(\mathbf{x})]$$

Radial basis $R_i(\mathbf{x})$ is a function of distance r_i defined as below:

$$R_i(\mathbf{x}) = R_i(r_i)$$

$$r_i = \sqrt{(x - x_i)^2 + (y - y_i)^2 + (z - z_i)^2} \qquad i = 1, 2, \cdots, n \qquad (2.3)$$

There are several forms of radial basis functions widely used by the mathematics community, and two of them (Multiquadrics form and Gaussian form) are used to test the 3D RPIM in this research project. In order to standardize the shape parameters of radial basis functions for Radial Point Interpolation Method, the modified forms of radial basis functions with dimensionless shape parameters are adopted as per Table 2.1.

Table 2.1   Radial Basis Functions with Dimensionless Shape Parameters

Name	Expression [1]	Shape Parameters
Multiquadrics (MQ)	$R_i(x, y, z) = [\, r_i^2 + (\alpha_c d_c)^2 \,]^q$	$\alpha_c \geq 0$, q
Gaussian (EXP)	$R_i(x, y, z) = \exp[\, -\alpha_c (\, r_i / d_c \,)^2 \,]$	α_c

[1] d_c denotes the average nodal spacing among all nodes in the local domain.

The polynomial basis is built as per Pascal triangle in 3D domain.

$$\mathbf{P}^T(\mathbf{x}) = \mathbf{P}^T(x, y, z) = [1, x, y, z, xy, yz, zx, x^2, y^2, z^2, \cdots] \qquad (2.4)$$

The vectors of coefficients $\mathbf{a}$ and $\mathbf{b}$ in Equation (2.1) are determined by enforcing the interpolation to pass through all n nodes within the local domain.

$$u_k = u(x_k, y_k, z_k) = \sum_{i=1}^{n} R_i(x_k, y_k, z_k) a_i + \sum_{j=1}^{m} P_j(x_k, y_k, z_k) b_j \qquad k = 1, 2, \cdots, n \qquad (2.5)$$

In order to guarantee a unique approximation of the function, the following constraints are usually imposed also.

$$\sum_{i=1}^{n} P_j(x_i, y_i, z_i) a_i = 0 \qquad j = 1, 2, \cdots, m \qquad (2.6)$$

Equations (2.5) and (2.6) can be expressed in matrix form as

$$\begin{bmatrix} \mathbf{R}_0 & \mathbf{P}_0 \\ \mathbf{P}_0^T & \mathbf{0} \end{bmatrix} \begin{Bmatrix} \mathbf{a} \\ \mathbf{b} \end{Bmatrix} = \mathbf{G} \begin{Bmatrix} \mathbf{a} \\ \mathbf{b} \end{Bmatrix} = \begin{Bmatrix} \mathbf{u}_0 \\ \mathbf{0} \end{Bmatrix} \tag{2.7}$$

where $\mathbf{u}_0$ is the vector of function values at all n nodes in the local domain.

$$\mathbf{u}_0 = [u_1, u_2, u_3, \cdots, u_n]^T \tag{2.8}$$

The radial moment matrix $\mathbf{R}_0$ is defined as

$$\mathbf{R}_0 = \begin{bmatrix} R_1(x_1, y_1, z_1) & R_2(x_1, y_1, z_1) & \cdots & R_n(x_1, y_1, z_1) \\ R_1(x_2, y_2, z_2) & R_2(x_2, y_2, z_2) & \cdots & R_n(x_2, y_2, z_2) \\ \vdots & \vdots & \vdots & \vdots \\ R_1(x_n, y_n, z_n) & R_2(x_n, y_n, z_n) & \cdots & R_n(x_n, y_n, z_n) \end{bmatrix}_{n \times n} \tag{2.9}$$

The polynomial moment matrix $\mathbf{P}_0$ is defined as

$$\mathbf{P}_0 = \begin{bmatrix} P_1(x_1, y_1, z_1) & P_2(x_1, y_1, z_1) & \cdots & P_m(x_1, y_1, z_1) \\ P_1(x_2, y_2, z_2) & P_2(x_2, y_2, z_2) & \cdots & P_m(x_2, y_2, z_2) \\ \vdots & \vdots & \vdots & \vdots \\ P_1(x_n, y_n, z_n) & P_2(x_n, y_n, z_n) & \cdots & P_m(x_n, y_n, z_n) \end{bmatrix}_{n \times m} \tag{2.10}$$

Because $R_k(x_i, y_i, z_i) = R_i(x_k, y_k, z_k)$, both radial moment matrix $\mathbf{R}_0$ and the combined moment matrix $\mathbf{G}$ are symmetric. The unique solution of Equation (2.7) can be obtained if the inverse of matrix $\mathbf{G}$ exists.

$$\begin{Bmatrix} \mathbf{a} \\ \mathbf{b} \end{Bmatrix} = \mathbf{G}^{-1} \begin{Bmatrix} \mathbf{u}_0 \\ \mathbf{0} \end{Bmatrix} \tag{2.11}$$

On substitution for $\mathbf{a}$ and $\mathbf{b}$, the Equation (2.1) can be re-written as

$$u(\mathbf{x}) = \begin{bmatrix} \mathbf{R}^T(\mathbf{x}) & \mathbf{P}^T(\mathbf{x}) \end{bmatrix} \begin{Bmatrix} \mathbf{a} \\ \mathbf{b} \end{Bmatrix} = \begin{bmatrix} \mathbf{R}^T(\mathbf{x}) & \mathbf{P}^T(\mathbf{x}) \end{bmatrix} \mathbf{G}^{-1} \begin{Bmatrix} \mathbf{u}_0 \\ \mathbf{0} \end{Bmatrix} = \mathbf{\Phi}(\mathbf{x}) \mathbf{u}_0 = \sum_{k=1}^{n} \phi_k(\mathbf{x}) u_k \tag{2.12}$$

The matrix of shape functions $\mathbf{\Phi}(\mathbf{x})$ is defined as

$$\mathbf{\Phi}(\mathbf{x}) = [\phi_1(\mathbf{x}), \phi_2(\mathbf{x}), \cdots, \phi_k(\mathbf{x}), \cdots, \phi_n(\mathbf{x})] \tag{2.13}$$

where each shape function is

$$\phi_k(\mathbf{x}) = \sum_{i=1}^{n} R_i(\mathbf{x}) \mathbf{G}^{-1}{}_{i,k} + \sum_{j=1}^{m} P_j(\mathbf{x}) \mathbf{G}^{-1}{}_{n+j,k} \qquad k = 1,2,\cdots,n \qquad (2.14)$$

The derivatives of function u(**x**) can be represented similarly as

$$\frac{\partial u}{\partial x} = \sum_{k=1}^{n} \frac{\partial \phi_k}{\partial x} u_k$$

$$\frac{\partial u}{\partial y} = \sum_{k=1}^{n} \frac{\partial \phi_k}{\partial y} u_k \qquad (2.15)$$

$$\frac{\partial u}{\partial z} = \sum_{k=1}^{n} \frac{\partial \phi_k}{\partial z} u_k$$

where the derivatives of shape functions are

$$\frac{\partial \phi_k}{\partial x} = \sum_{i=1}^{n} \frac{\partial R_i}{\partial x} \mathbf{G}^{-1}{}_{i,k} + \sum_{j=1}^{m} \frac{\partial P_j}{\partial x} \mathbf{G}^{-1}{}_{n+j,k}$$

$$\frac{\partial \phi_k}{\partial y} = \sum_{i=1}^{n} \frac{\partial R_i}{\partial y} \mathbf{G}^{-1}{}_{i,k} + \sum_{j=1}^{m} \frac{\partial P_j}{\partial y} \mathbf{G}^{-1}{}_{n+j,k} \qquad k = 1,2,\cdots,n \qquad (2.16)$$

$$\frac{\partial \phi_k}{\partial z} = \sum_{i=1}^{n} \frac{\partial R_i}{\partial z} \mathbf{G}^{-1}{}_{i,k} + \sum_{j=1}^{m} \frac{\partial P_j}{\partial z} \mathbf{G}^{-1}{}_{n+j,k}$$

For EXP radial basis function shown in Table 2.1, its partial derivatives can be obtained as follows:

$$\frac{\partial R_i}{\partial x} = -\frac{2\alpha_c}{d_c^2} R_i(x,y,z)(x-x_i)$$

$$\frac{\partial R_i}{\partial y} = -\frac{2\alpha_c}{d_c^2} R_i(x,y,z)(y-y_i) \qquad i = 1,2,\cdots,n \qquad (2.17)$$

$$\frac{\partial R_i}{\partial z} = -\frac{2\alpha_c}{d_c^2} R_i(x,y,z)(z-z_i)$$

Similarly for MQ radial basis function shown in Table 2.1, its partial derivatives can be obtained as follows:

$$\frac{\partial R_i}{\partial x} = 2q\left[r_i^2 + (\alpha_c d_c)^2\right]^{q-1}(x-x_i) \qquad i = 1,2,\cdots,n \qquad (2.18)$$

18

$$\frac{\partial R_i}{\partial y} = 2q\left[r_i^2 + (\alpha_c d_c)^2\right]^{q-1}(y - y_i)$$

$$\frac{\partial R_i}{\partial z} = 2q\left[r_i^2 + (\alpha_c d_c)^2\right]^{q-1}(z - z_i)$$

2.2 Advantage of RPIM with Polynomial Reproduction

There is a crucial assumption that the combined moment matrix $\mathbf{G}$ is invertible in the formation process of RPIM shape functions. Mathematicians have proved that the radial moment matrix $\mathbf{R}_0$ is always invertible for arbitrary scattered nodes, as long as some specific shape parameters are not used. It implies that RPIM without polynomial terms (m = 0, $\mathbf{G} = \mathbf{R}_0$) might perform the task of interpolation very well. However, it is also found that PIM with radial basis alone can not produce the linear polynomials exactly, although it can approach the polynomials in desired accuracy when the nodes are refined. This can be seen by the fitting example in Section 2.4.1 later. In stress analysis for 3D solids, the MFree methods based on RPIM without polynomial basis cannot ensure that the states of constant strain and rigid body displacement are correctly represented. Therefore, it will not pass the standard patch test, which has been widely used to verify the performance of finite element methods.

In order to let RPIM pass the patch test, Wang and Liu (2001) suggested adding polynomial terms up to linear order (m = 4) as basis functions for PIM formation together with the radial basis functions. Fitting example in Section 2.4.1 also shows that PIM using radial-polynomial basis can approximate linear functions in high accuracy.

Accordingly, polynomial basis in Equation (2.4) can be simplified as

$$\mathbf{P}^T(\mathbf{x}) = \mathbf{P}^T(x, y, z) = [1, x, y, z] \tag{2.19}$$

The polynomial moment matrix $\mathbf{P}_0$ in Equation (2.10) can also be re-written as

$$\mathbf{P}_0 = \begin{bmatrix} 1 & x_1 & y_1 & z_1 \\ 1 & x_2 & y_2 & z_2 \\ \vdots & \vdots & \vdots & \vdots \\ 1 & x_n & y_n & z_n \end{bmatrix}_{n \times 4} \tag{2.20}$$

In general, the combined moment matrix **G** based on radial moment matrix **R**$_0$ in Equation (2.9) and polynomial moment matrix **P**$_0$ in Equation (2.20) is invertible for all practical situations. The excellent stability of RPIM against the irregularity of nodes is one of its advantages.

2.3 Properties of RPIM Shape Functions

As long as the moment matrix **G** is invertible, the RPIM shape functions $\phi_i(\mathbf{x})$ depend uniquely on the distribution of scattered nodes within the local support domain. The RPIM shape functions have the following properties:

1. RPIM shape functions are linearly independent in the local support domain because the basis functions are linearly independent and **G**$^{-1}$ is assumed to exist.

2. RPIM shape functions possess the Kronecker delta function property, which can be stated as

$$\phi_i\left(\mathbf{x}=\mathbf{x}_j\right)=\begin{cases}1 & i=j & j=1,2,\cdots,n \\ 0 & i\neq j & i,j=1,2,\cdots,n\end{cases} \tag{2.21}$$

This property can be proven as follows:

Assume

$$\mathbf{u}_0=\left[0,0,\cdots,u_i,\cdots,0\right]^T \tag{2.22}$$

Substituting the above equation into Equation (2.12) yields

$$u\left(\mathbf{x}=\mathbf{x}_j\right)=\sum_{k=1}^{n}\phi_k\left(\mathbf{x}_j\right)u_k=\phi_i\left(\mathbf{x}_j\right)u_i \tag{2.23}$$

When i = j, we have

$$u_i=\phi_i\left(\mathbf{x}_i\right)u_i \tag{2.24}$$

which leads to

$$\phi_i\left(\mathbf{x}_i\right)=1 \tag{2.25}$$

When i ≠ j, we have

$$u_j = 0 = \phi_i(\mathbf{x}_j)u_i \tag{2.26}$$

which requires

$$\phi_i(\mathbf{x}_j) = 0 \tag{2.27}$$

Equations (2.25) and (2.27) indicate that RPIM shape functions possess the Kronecker delta function property, which is very important for handling the essential boundary conditions.

3. $\phi_i(\mathbf{x})$ is the partition of unity.

$$\sum_{i=1}^{n} \phi_i(\mathbf{x}) = 1 \tag{2.28}$$

As mentioned in Section 2.2, the PIM using radial-polynomial basis can reproduce the linear polynomials exactly. Assume a linear function u(**x**) = c, where c is a constant. We should have

$$\mathbf{u}_0 = c[1,1,\cdots,1]^T \tag{2.29}$$

Substituting the above equation into Equation (2.12) yields

$$u(\mathbf{x}) = c = \sum_{i=1}^{n} \phi_i(\mathbf{x})u_i = c\sum_{i=1}^{n} \phi_i(\mathbf{x}) \tag{2.30}$$

which leads to the Equation (2.28).

4. RPIM shape functions usually possess higher continuity due to the high continuity of the radial basis functions.

2.4 3-D Function Fitting

The quality of interpolation by RPIM is examined via examples of 3-D function fitting, with due considerations of the following factors:

- Complexity of 3-D functions to be fitted

- With or without polynomial basis

- Different types of radial basis functions (EXP and MQ)

- Different shape parameters of radial basis functions

- Regularity of field nodes distribution

- Number of nodes in the local support domain

All these factors are taken into account through the fitting example as described below:

Consider a cubic domain of $(x, y, z) \in [0, 1]$ x $[0, 1]$ x $[0, 1]$, upon which two functions are fitted. The first of them is a linear function defined as

$$f_1(x, y, z) = 0.5 + x + 2y + 3z \tag{2.31}$$

The other is a nonlinear function defined as

$$f_2(x, y, z) = \sin(x) \cos(y) \, e^z \tag{2.32}$$

In order to investigate the effect of node distribution on the fitting accuracy, the cubic domain is discretized into a set of field nodes in the following patterns:

Pattern 1   27 (3 x 3 x 3) nodes evenly distributed

Pattern 2   27 (3 x 3 x 3) nodes randomly distributed

Pattern 3   27 (3 x 3 x 3) nodes randomly distributed

Pattern 4   27 (3 x 3 x 3) nodes randomly distributed

Pattern 5   512 (8 x 8 x 8) nodes evenly distributed

For each pattern of node distribution, the average nodal spacing d_c among all nodes in this cubic domain is evaluated as per Equation (1.2).

The fitting of 3-D functions is carried out in the following steps:

1. Define the sampling grid with 1331 (11 x 11 x 11) sample points evenly distributed within the cubic domain

2. Calculate the function values and derivatives at all sample points as per function's definition

3. Loop over all the sample points

   a) Construct the local support domain for each sample point based on the support domain size $\alpha_s d_c$

b) Calculate function values at all nodes within each local support domain as per function's definition and construct the vector of function values $\mathbf{u}_0$

c) Construct the vector of radial basis $\mathbf{R}^T(\mathbf{x})$ according to the relationship between the sample point and each node in the local support domain – Equations (2.2) and (2.3)

d) Construct the vector of polynomial basis $\mathbf{P}^T(\mathbf{x})$ for this sample point as per Equation (2.19)

e) Construct the radial moment matrix $\mathbf{R}_0$ based on all nodes within the local support domain and calculate its condition number – Equation (2.9)

f) Construct the polynomial moment matrix $\mathbf{P}_0$ based on all nodes within the local support domain as per Equation (2.20)

g) Get the combined moment matrix $\mathbf{G}$ and calculate its condition number

h) Get the inverse of the combined moment matrix, i.e. $\mathbf{G}^{-1}$

i) Approximate the function value at the sample point as per Equation (2.12)

j) Approximate the derivatives of function at the sample point using the similar procedure

4. Statistical analysis of the fitting accuracy at all sample points

a) Output the average condition number of the radial moment matrix $\mathbf{R}_0$

b) Output the average condition number of the combined moment matrix $\mathbf{G}$

c) Calculate the overall fitting error as per formula below

$$error = \frac{\sum_{i=1}^{1331}\left|f_i - \widetilde{f}_i\right|}{\sum_{i=1}^{1331}\left|f_i\right|} \tag{2.33}$$

where f_i and $\widetilde{f}_i$ are function values (or its derivatives) at the sample point i obtained by the analytical method and the interpolation method respectively.

2.4.1 Fitting of a Linear Function

The linear function $f_l(x, y, z)$ is approximated by RPIM over the cubic domain, which is discretized as per nodal pattern 1. A very large value of support domain size parameter is assumed so that all 27 nodes are always included in the local support domain of every sample point. Both EXP and MQ radial basis functions are used with some typical shape parameters to interpolate this linear function. The fitting errors of the function itself and its derivatives are summarized in Table 2.2 and Table 2.3. The Table 2.2 shows the fitting quality by RPIM without linear polynomial terms, while the Table 2.3 shows the fitting quality by RPIM with linear polynomial terms.

Table 2.2 Fitting of a Linear Function by RPIM without Polynomial Terms

Radial Basis			Condition	Fitting Error			
Type	α_c	q	Number R	f	$\partial f/\partial x$	$\partial f/\partial y$	$\partial f/\partial z$
EXP	0.6	-	4.73E+02	6.40E-02	5.88E-01	4.08E-01	3.85E-01
EXP	0.2	-	1.97E+05	2.26E-02	1.67E-01	1.63E-01	1.63E-01
MQ	0.5	1.3	3.30E+03	6.18E-03	6.65E-02	4.35E-02	3.81E-02
MQ	1.5	1.9	2.95E+05	1.22E-03	1.06E-02	9.60E-03	9.39E-03

Table 2.3 Fitting of a Linear Function by RPIM with Polynomial Terms

Radial Basis			Condition	Fitting Error			
Type	α_c	q	Number G	f	$\partial f/\partial x$	$\partial f/\partial y$	$\partial f/\partial z$
EXP	0.6	-	1.39E+03	9.86E-07	5.46E-06	4.35E-06	2.71E-06
EXP	0.2	-	2.88E+05	1.29E-03	2.15E-03	1.35E-03	5.31E-04
MQ	0.5	1.3	3.62E+03	7.31E-06	7.04E-05	2.63E-05	1.29E-05
MQ	1.5	1.9	3.65E+05	2.30E-04	1.09E-03	4.19E-04	8.46E-04

By comparing Table 2.2 and Table 2.3, it can be seen that the fitting error when linear polynomial terms are included is at least five times smaller than the corresponding fitting error when linear polynomial terms are not included. This indicates that the RPIM without linear polynomial terms can not ensure the reproduction of linear polynomials. In other words, the linear polynomial terms should be included in the RPIM basis so that the RPIM can

approximate the linear functions accurately. The polynomial terms up to linear order (m = 4) are always included in the function fittings and stress analyses hereafter unless otherwise noted.

2.4.2   Fitting of a Complicated Nonlinear Function

Through the fitting of a complicated function $f_2(x, y, z)$ with the inclusion of all 27 nodes in the local support domain of each sample point, the effect of EXP shape parameter is investigated firstly, followed by that of MQ shape parameters. Finally, the effect of domain size on the fitting quality is also studied.

Effect of EXP shape parameter

The effect of EXP shape parameter on fitting quality is illustrated in Figures 2.1 to 2.4. The findings from these figures are summarized as follows:

- The condition number of matrix **G** is close to that of matrix **R**. This implies that the condition of the combined moment matrix **G** is largely determined by that of the radial moment matrix **R**.

- The condition number of moment matrix decreases monotonically with the shape parameter α_c. A large value of α_c leads to a small condition number.

- The fitting error for the function itself reaches the minimum when the shape parameter α_c around 0.1. However, the condition number of moment matrix is quite large at this time. Moment matrix with too large condition number might be ill-conditioned, and might lead to large numerical errors when inversed. From the viewpoint of condition number only, the shape parameter α_c should be big enough to produce a small condition number. The preferred range of shape parameter α_c can be from 0.2 to 0.6, after a compromise between fitting error and condition number.
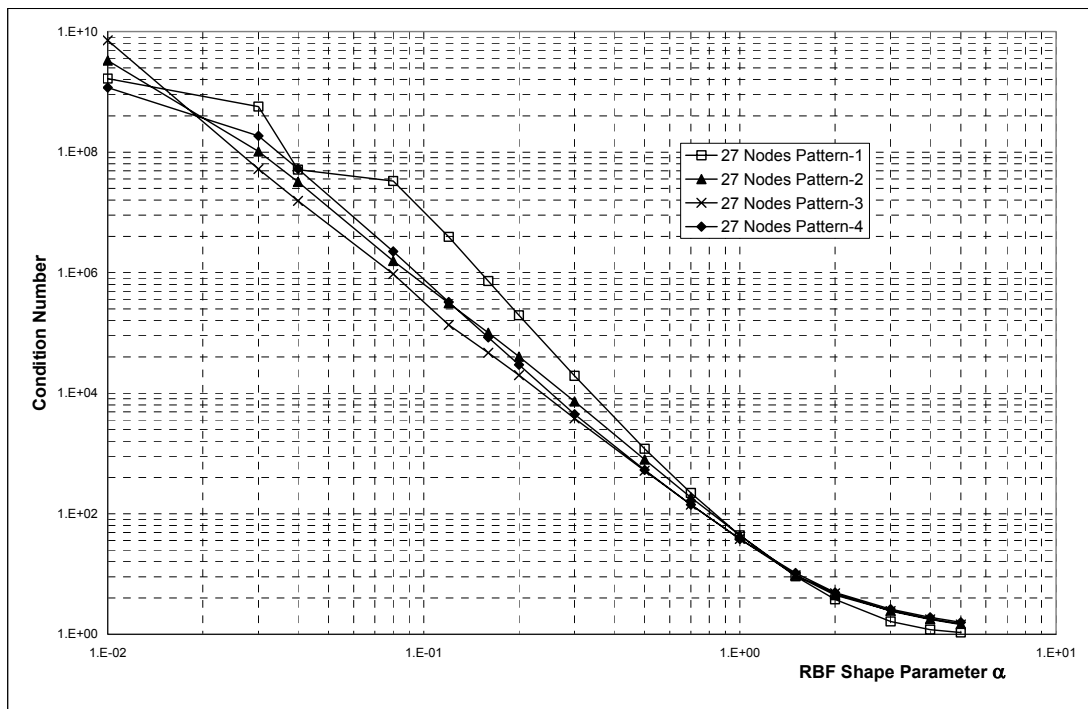
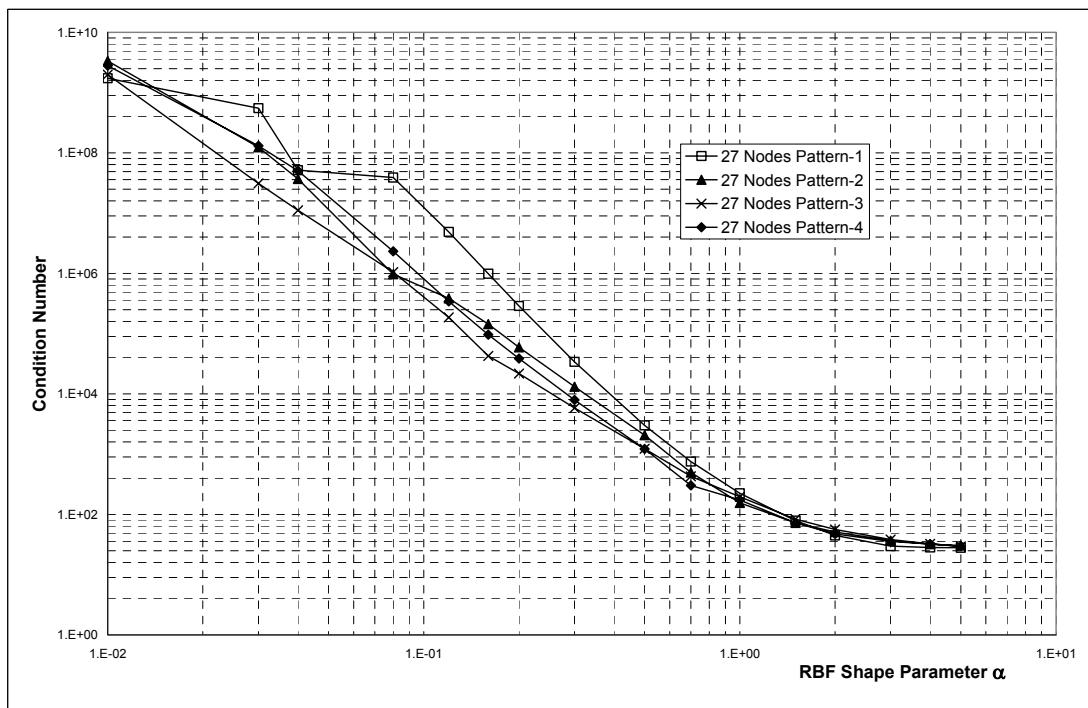**Figure 2.1**   Effect of EXP Shape Parameter on Condition Number of Moment Matrix **R**

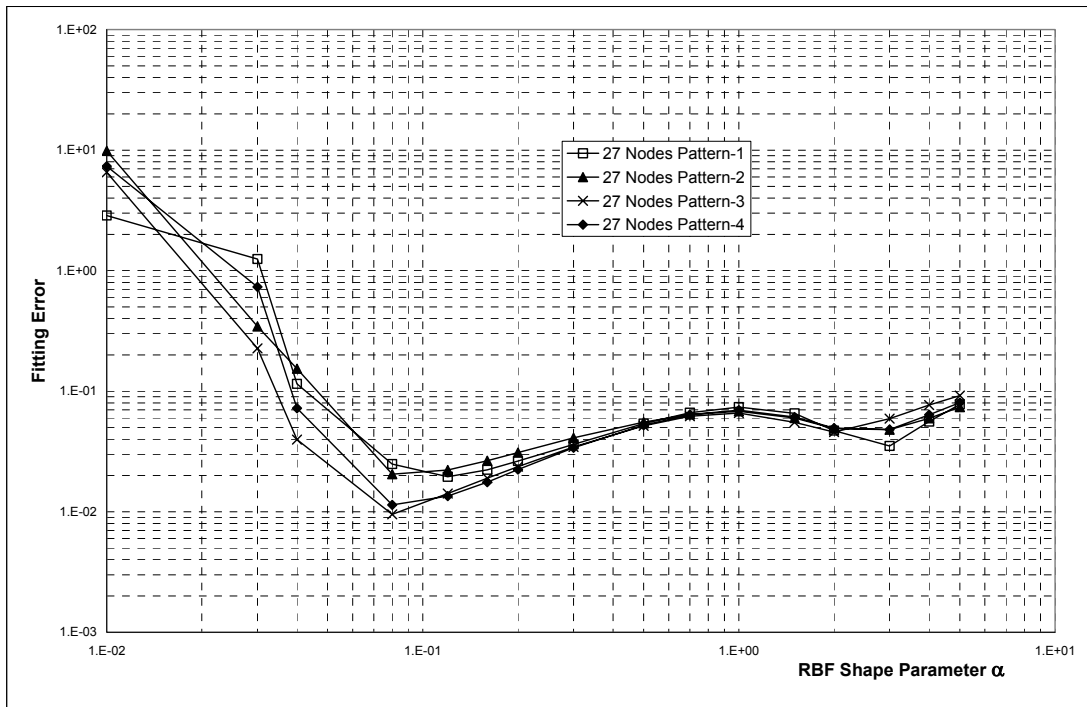**Figure 2.2**   Effect of EXP Shape Parameter on Condition Number of Moment Matrix **G**

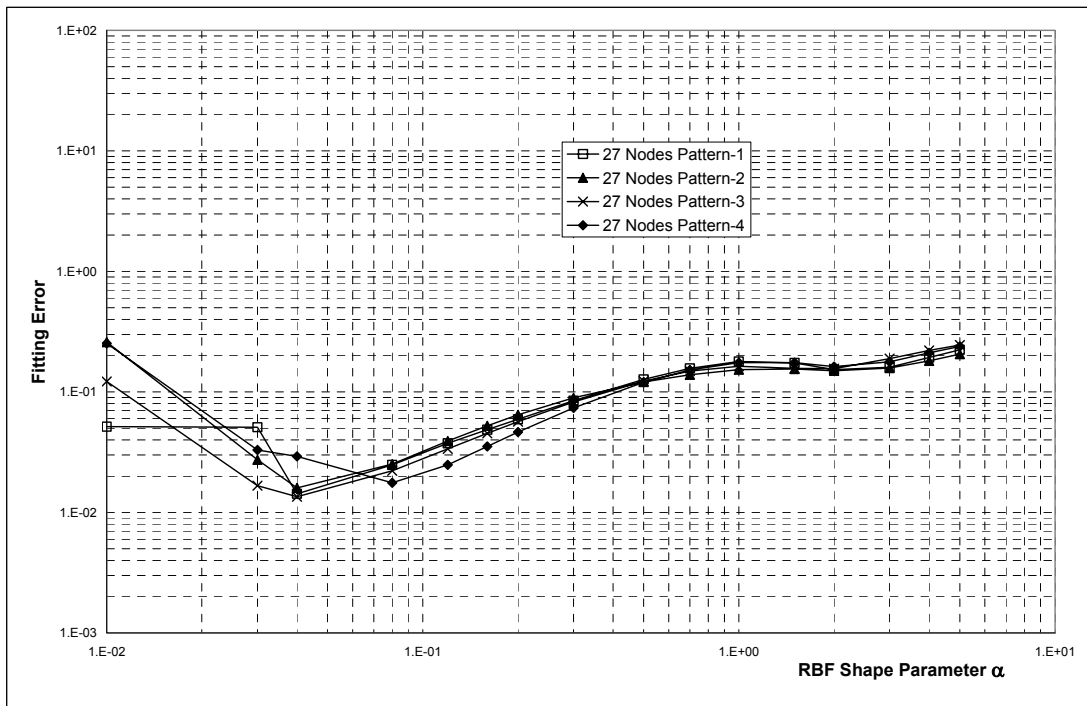**Figure 2.3**   Effect of EXP Shape Parameter on Fitting Error of Function f

Figure 2.4   Effect of EXP Shape Parameter on Fitting Error of Derivative ǝf/ǝx

- The fitting error for derivatives of the function varies with the shape parameter α_c similarly as the fitting error for the function itself does.

- The nodal distribution pattern has little effect on the fitting quality.

Effect of MQ shape parameters

The effect of MQ shape parameters on fitting quality is illustrated in Figures 2.5 to 2.10. The findings from these figures are summarized as follows:

- The condition number of matrix **G** is close to that of matrix **R**. This implies again that the condition of the combined moment matrix **G** is largely determined by that of the radial moment matrix **R**.

- The moment matrix **G** and **R** are singular when q equals an integer.

- The condition number varies little with shape parameter q, except when q is near an integer.

- The shape parameter α_c has a vital effect on the condition number. When α_c changes from 0.5 to 2.5, the condition number increases about 10^3 times.

- The fitting error for the function itself and its derivatives varies with the MQ shape parameters in the similar manner as the condition number does, except that the fitting error is not that sensitive to the shape parameter α_c.

- The fitting error reaches the minimum when shape parameter q is near but not equal to 2.0. Similar to the condition number of the moment matrix, the fitting error does not change much with the shape parameter q, a wide range of q from 0.0 to 3.5 will give reasonable fitting accuracy, as long as integers (singularity of the moment matrix) within this range are avoided.

- A bigger value of shape parameter α_c will give better fitting accuracy but bigger condition number, which might cause a large numerical error when the moment matrix is inversed. The preferred range of shape parameter α_c can be from 0.5 to 2.0, after a compromise between fitting error and condition number.

- The nodal distribution pattern has little effect on the fitting quality.
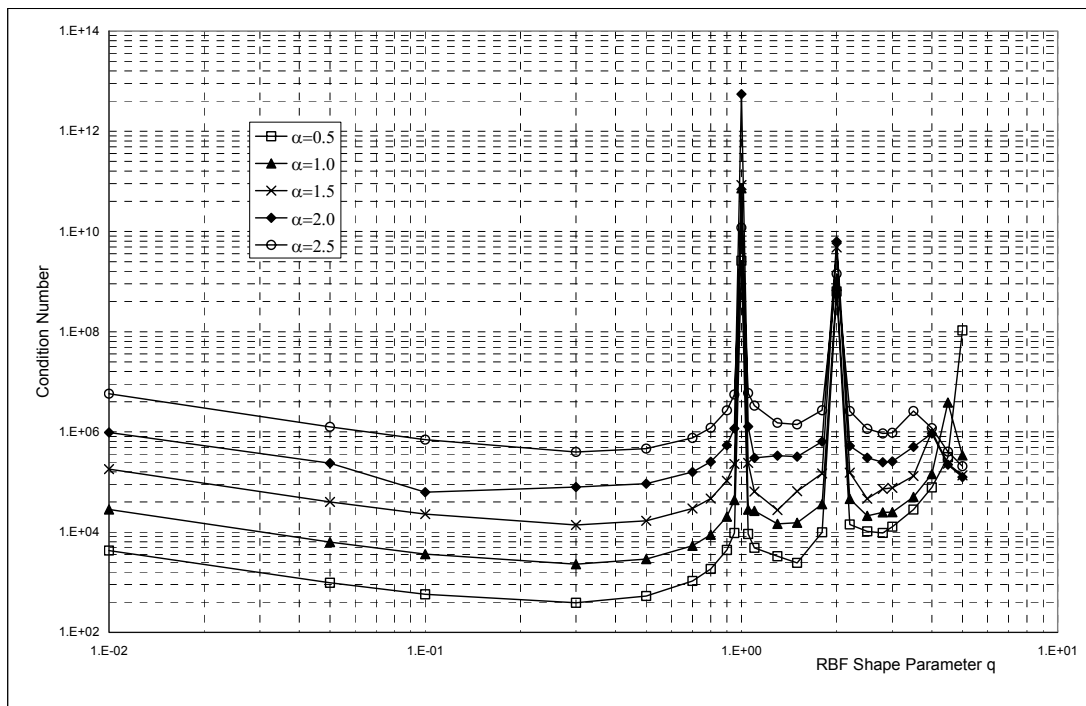
Figure 2.5 Effect of MQ Shape Parameters on Condition Number of Moment Matrix **R**
(based on regular nodal distribution pattern 1)
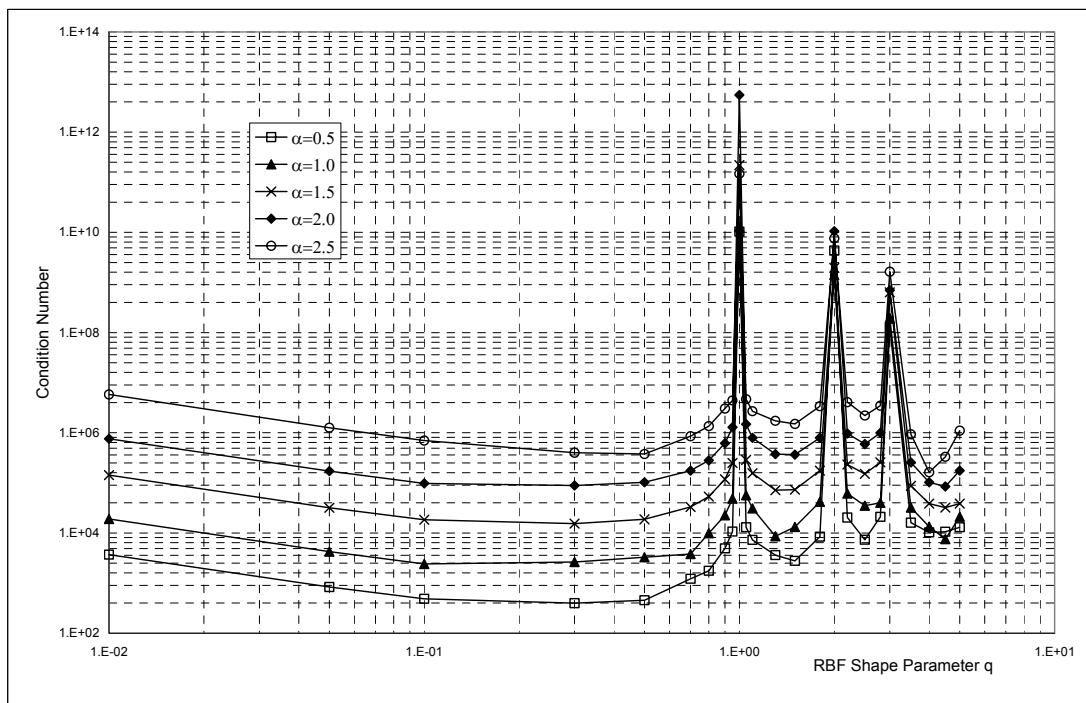
Figure 2.6 Effect of MQ Shape Parameters on Condition Number of Moment Matrix **G**
(based on regular nodal distribution pattern 1)
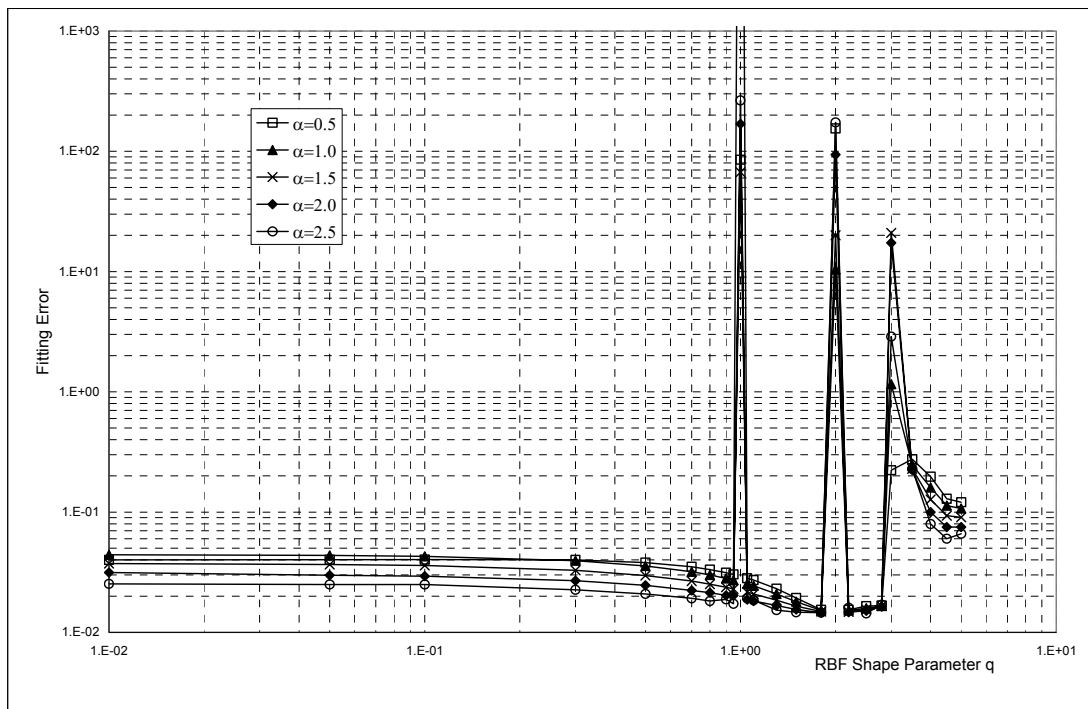
Figure 2.7   Effect of MQ Shape Parameters on Fitting Error of Function f
(based on regular nodal distribution pattern 1)
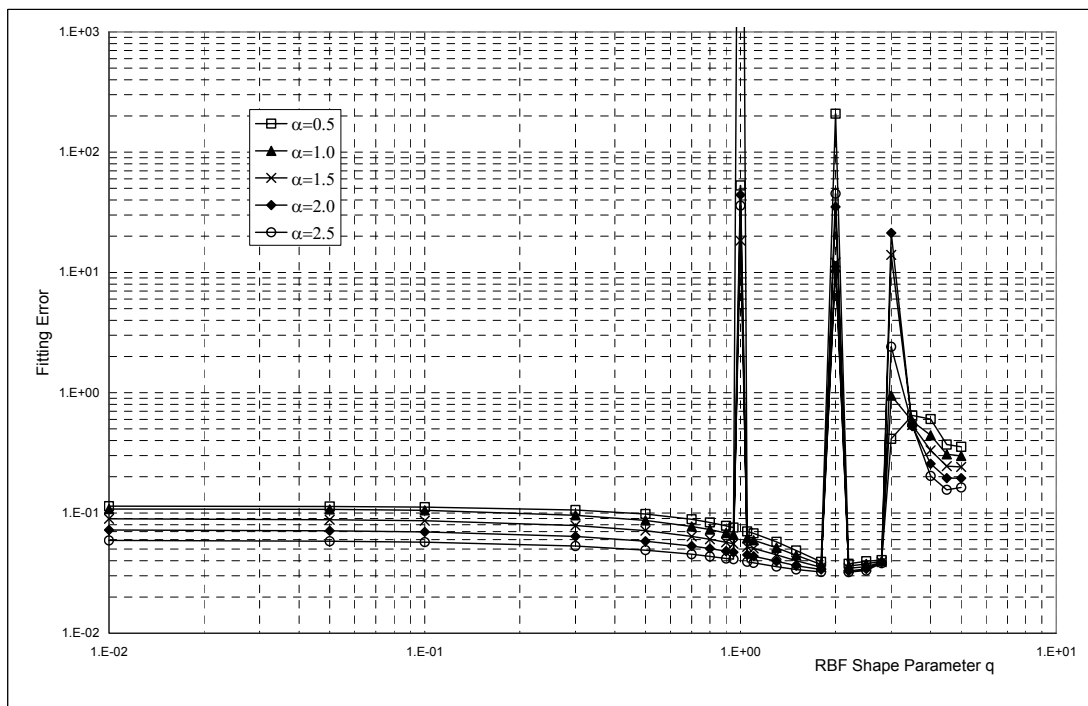
Figure 2.8   Effect of MQ Shape Parameters on Fitting Error of Derivative ∂f/∂x
(based on regular nodal distribution pattern 1)
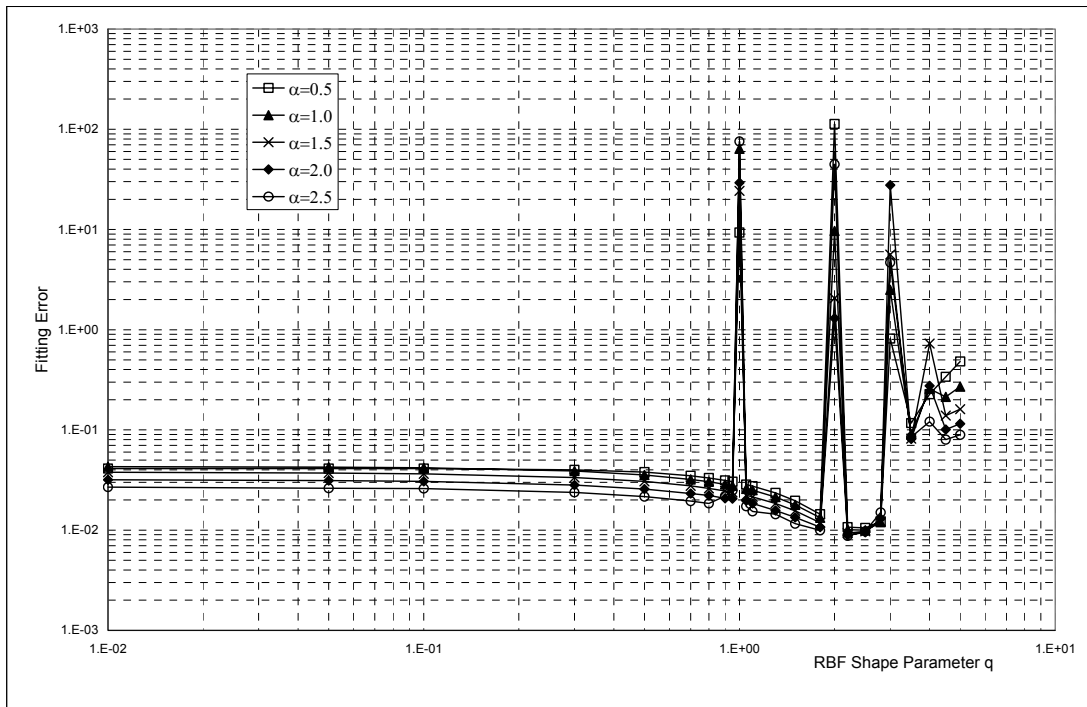
Figure 2.9   Effect of MQ Shape Parameters on Fitting Error of Function f

(based on irregular nodal distribution pattern 2)
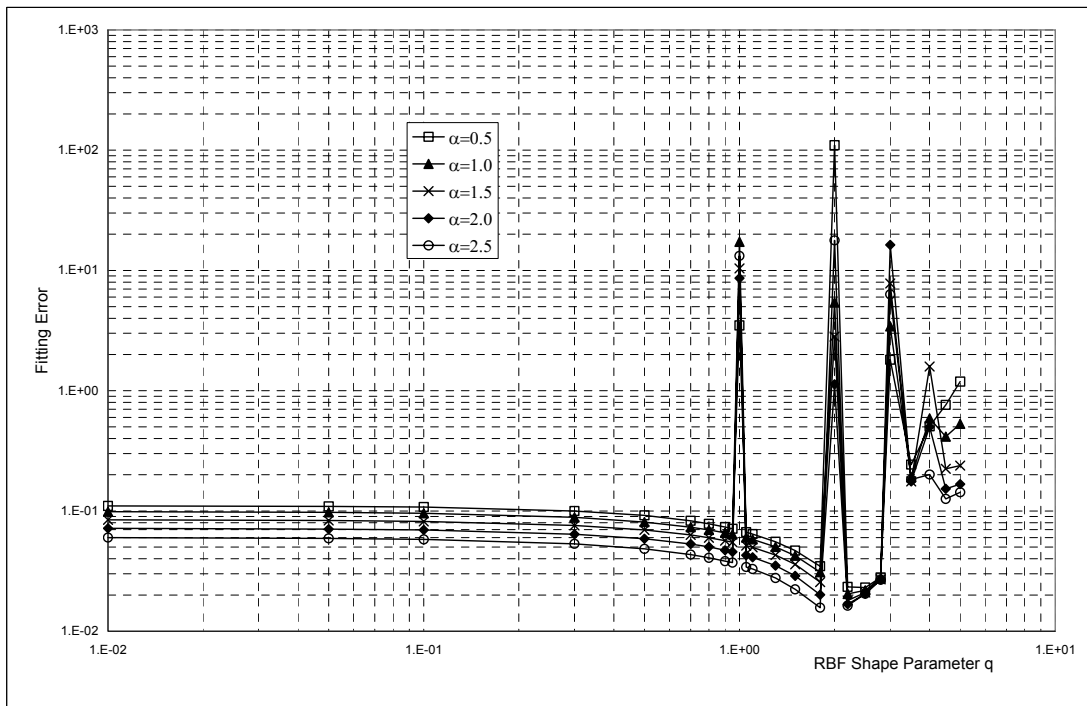
Figure 2.10   Effect of MQ Shape Parameters on Fitting Error of Derivative ∂f/∂x

(based on irregular nodal distribution pattern 2)

Effect of domain size

Through the fitting of the complicated function $f_2(x, y, z)$ over the cubic domain that is discretized into 512 evenly distributed nodes as per Pattern 5, the effect of domain size on the fitting quality is investigated with some typical values of RBF shape parameters. The fitting results are illustrated in Figures 2.11 and 2.12, from which the findings are summarized as follows:

- The bigger the domain size parameter is, the more nodes are included in the local domain for each sample point, and hence the more computer time is necessary for interpolation.

- The condition number of moment matrix **G** increases monotonically with the domain size parameter.

- The fitting accuracy does not increase with the domain size parameter. The extra fitting error coming with the bigger domain size might be from two sources. Firstly, more nodes are included for the interpolation with the increase of domain size, thus more numerical operations are necessary. The extra numerical error could be caused by the increased number of numerical operations. Secondly, the condition number of moment matrix also increases with the domain size, and extra numerical error could be caused when the moment matrix is inversed.

- The preferred range of support domain size parameter, with due consideration of both fitting error and condition number, is between 1.5 and 1.9.

- The domain size is a dominant parameter that decides how many nodes will be included in the local support domain. The preferred range of nodes number in the local domain is from 10 to 30. It will be seen in the following chapters that this recommended range of nodes number will yield good results in the stress analysis for 3D solids.
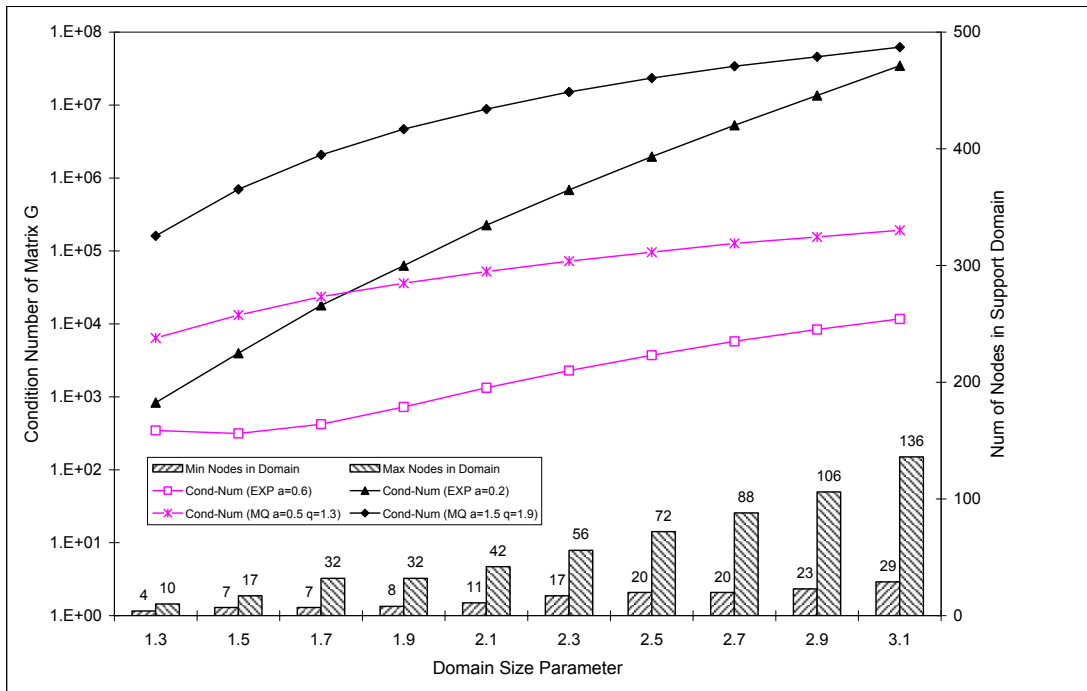
Figure 2.11   Effect of Domain Size on Condition Number of Moment Matrix **G**
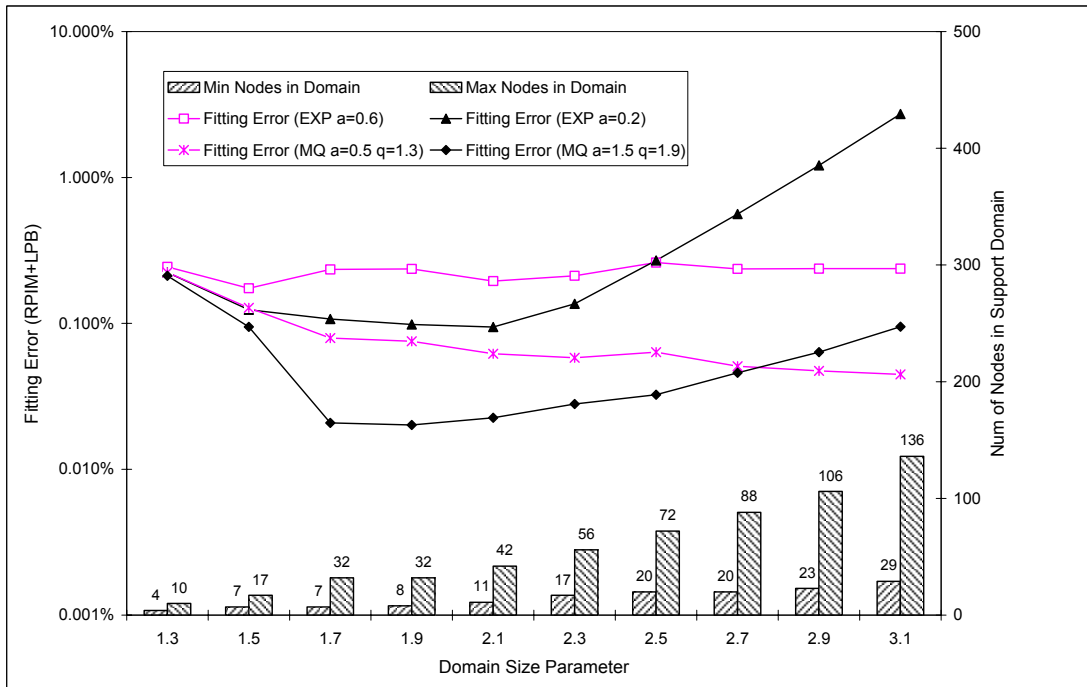
Figure 2.12   Effect of Domain Size on Fitting Error of Function f

2.4.3 Conclusions from Function Fitting

The following conclusions can be drawn from the above example of 3D function fitting.

- The linear polynomial basis should be included in the formation of RPIM shape functions.

- The RPIM is numerically stable for both regular and irregular nodal distributions.

- The preferred number of nodes included in the local domain is from 10 to 30.

- Both radial basis functions of EXP and MQ could be employed to produce good fitting quality, as long as the preferred ranges of shape parameters are used in the interpolation. For EXP, the shape parameter is $\alpha_c = 0.2 \sim 0.6$. For MQ, the shape parameter is $\alpha_c = 0.5 \sim 2.0$, $q = 0 \sim 3.5$ except integers.

Chapter 3   Radial Point Interpolation Method

The Radial Point Interpolation Method (RPIM) can be employed to solve a wide range of engineering problems governed by differential equations. In this chapter, static and dynamic analyses of three-dimensional solids are used to demonstrate the formulation and procedure of RPIM.

3.1 RPIM for Solid Mechanics

3.1.1 Stress and Strain

A three-dimensional body occupying a volume V and having a surface S. Points in the body are located by x, y, z coordinates. The boundary is constrained on some region, where displacement is specified. On part of the boundary, distributed force per unit area **t**, also called traction, is applied. The body deforms under the force.

The deformation of a point $\mathbf{x} = [x, y, z]^T$ is given by the three components of its displacement.

$$\mathbf{u} = [u, v, w]^T \tag{3.1}$$

The distributed force per unit volume, for example, the weight per unit volume, is the vector **b** given by

$$\mathbf{b} = [b_x, b_y, b_z]^T \tag{3.2}$$

The surface traction **t**, for example, distributed contact force and action of pressure, is given by its component values at points on the surface.

$$\mathbf{t} = [t_x, t_y, t_z]^T \tag{3.3}$$

A load **P** acting at a point i is represented by its three components.

$$\mathbf{P}_i = [P_x, P_y, P_z]_i^T \tag{3.4}$$

The stress is represented by its six independent components as

$$\boldsymbol{\sigma} = \left[\sigma_x, \sigma_y, \sigma_z, \tau_{yz}, \tau_{xz}, \tau_{xy}\right]^T \tag{3.5}$$

where σ_x, σ_y, σ_z are normal stresses and τ_{yz}, τ_{xz}, τ_{xy} are shear stresses.

The Von Mises stress which serves as a criterion in determining the onset of failure in ductile materials is given by

$$\sigma_{VM} = \sqrt{\left(\sigma_x + \sigma_y + \sigma_z\right)^2 - 3\left(\sigma_x\sigma_y + \sigma_y\sigma_z + \sigma_z\sigma_x - \tau_{yz}^2 - \tau_{xz}^2 - \tau_{xy}^2\right)} \tag{3.6}$$

The strain is also represented in a vector form that corresponds to the stresses.

$$\boldsymbol{\varepsilon} = \left[\varepsilon_x, \varepsilon_y, \varepsilon_z, \gamma_{yz}, \gamma_{xz}, \gamma_{xy}\right]^T \tag{3.7}$$

where ε_x, ε_y, ε_z are normal strains and γ_{yz}, γ_{xz}, γ_{xy} are shear strains.

3.1.2 Strain-Displacement Relations

The strain-displacement relations hold for small deformations as

$$\boldsymbol{\varepsilon} = \left[\frac{\partial u}{\partial x}, \frac{\partial v}{\partial y}, \frac{\partial w}{\partial z}, \frac{\partial v}{\partial z} + \frac{\partial w}{\partial y}, \frac{\partial u}{\partial z} + \frac{\partial w}{\partial x}, \frac{\partial u}{\partial y} + \frac{\partial v}{\partial x}\right]^T = \mathbf{L}\mathbf{u} \tag{3.8}$$

where $\mathbf{L}$ is a differential operator defined as

$$\mathbf{L} = \begin{bmatrix} \partial/\partial x & 0 & 0 \\ 0 & \partial/\partial y & 0 \\ 0 & 0 & \partial/\partial z \\ 0 & \partial/\partial z & \partial/\partial y \\ \partial/\partial z & 0 & \partial/\partial x \\ \partial/\partial y & \partial/\partial x & 0 \end{bmatrix} \tag{3.9}$$

3.1.3 Stress-Strain Relations

Properties of isotropic material include density ρ, Young's modulus E and Poisson's ratio ν.

For linear elastic materials, the stress-strain relations come from the generalized Hooke's law, which gives

$$\boldsymbol{\sigma} = \mathbf{D}\boldsymbol{\varepsilon} \tag{3.10}$$

where $\mathbf{D}$ is the symmetric (6 x 6) material matrix given by

$$\mathbf{D} = \frac{E}{(1+v)(1-2v)} \begin{bmatrix} 1-v & v & v & 0 & 0 & 0 \\ v & 1-v & v & 0 & 0 & 0 \\ v & v & 1-v & 0 & 0 & 0 \\ 0 & 0 & 0 & 0.5-v & 0 & 0 \\ 0 & 0 & 0 & 0 & 0.5-v & 0 \\ 0 & 0 & 0 & 0 & 0 & 0.5-v \end{bmatrix} \tag{3.11}$$

3.1.4 Energy Principle

In mechanics of solids, our problem is to determine the displacement $\mathbf{u}$ of the body described above, satisfying the equilibrium equations. Note that stresses are related to strains, which, in turn, are related to displacements. This leads to requiring solution of second-order partial differential equations. For problems of complex geometries, general boundary and loading conditions, variational methods based on energy principle are usually employed to solve the partial differential equations.

We define the Lagrangian functional as

$$\mathbf{L} = \mathbf{T} - \mathbf{U} + \mathbf{W} \tag{3.12}$$

where $\mathbf{T}$ is the kinetic energy, $\mathbf{U}$ is the strain energy and $\mathbf{W}$ is the work done by external forces.

The kinetic energy is given by

$$\mathbf{T} = \frac{1}{2} \int_V \rho \dot{\mathbf{u}}^T \dot{\mathbf{u}} dV \tag{3.13}$$

For solid body of elastic materials, the strain energy is given by

$$\mathbf{U} = \frac{1}{2} \int_V \boldsymbol{\varepsilon}^T \boldsymbol{\sigma} dV \tag{3.14}$$

The work done by external forces is given by

$$\mathbf{W} = \int_V \mathbf{u}^T \mathbf{b} dV + \int_S \mathbf{u}^T \mathbf{t} dS + \sum_i \mathbf{u}_i^T \mathbf{P}_i \tag{3.15}$$

Substituting Equations (3.13), (3.14) and (3.15) into (3.12) yields

$$\mathbf{L} = -\frac{1}{2}\int_V \boldsymbol{\varepsilon}^T \boldsymbol{\sigma} dV + \int_V \mathbf{u}^T \mathbf{b} dV + \int_S \mathbf{u}^T \mathbf{t} dS + \sum_i \mathbf{u}_i^T \mathbf{P}_i + \frac{1}{2}\int_V \rho \dot{\mathbf{u}}^T \dot{\mathbf{u}} dV \qquad (3.16)$$

According to the Hamilton's principle, for an arbitrary time interval from t_1 to t_2, the state of motion of a body extremizes the functional

$$\mathbf{I} = \int_{t_1}^{t_2} \mathbf{L} dt \qquad (3.17)$$

Mathematically, Hamilton's principle states

$$\delta \int_{t_1}^{t_2} \mathbf{L} dt = 0 \qquad (3.18)$$

Substituting for **L** from Equation (3.16) yields

$$\int_{t_1}^{t_2}\left[-\int_V \delta\boldsymbol{\varepsilon}^T \boldsymbol{\sigma} dV + \int_V \delta\mathbf{u}^T \mathbf{b} dV + \int_S \delta\mathbf{u}^T \mathbf{t} dS + \sum_i \delta\mathbf{u}_i^T \mathbf{P}_i - \int_V \rho \delta\mathbf{u}^T \ddot{\mathbf{u}} dV \right] dt = 0 \qquad (3.19)$$

Thus, the well-known Galerkin weak form can be obtained as

$$\int_V \delta\boldsymbol{\varepsilon}^T \boldsymbol{\sigma} dV - \int_V \delta\mathbf{u}^T \mathbf{b} dV - \int_S \delta\mathbf{u}^T \mathbf{t} dS - \sum_i \delta\mathbf{u}_i^T \mathbf{P}_i + \int_V \rho \delta\mathbf{u}^T \ddot{\mathbf{u}} dV = 0 \qquad (3.20)$$

3.1.5 Formulation of RPIM

As per discussion in Chapter 2, the displacement **u** at any point of interest $\mathbf{x}_Q$ can be expressed as a linear combination of shape functions ϕ_i and nodal displacements $\mathbf{u}_i$ at all n nodes within the local support domain of point $\mathbf{x}_Q$.

$$\mathbf{u} = [u, v, w]^T = \mathbf{Nq} \qquad (3.21)$$

where **q** is the nodal displacement vector for all nodes in the local support domain.

$$\mathbf{q} = [u_1, v_1, w_1, u_2, v_2, w_2, \cdots, u_n, v_n, w_n]^T \qquad (3.22)$$

Shape matrix **N** is defined as

$$\mathbf{N} = \begin{bmatrix} \phi_1 & 0 & 0 & \phi_2 & 0 & 0 & & \phi_n & 0 & 0 \\ 0 & \phi_1 & 0 & 0 & \phi_2 & 0 & \cdots & 0 & \phi_n & 0 \\ 0 & 0 & \phi_1 & 0 & 0 & \phi_2 & & 0 & 0 & \phi_n \end{bmatrix} \tag{3.23}$$

Substituting Equation (3.21) into Equation (3.8) yields

$$\boldsymbol{\varepsilon} = \mathbf{Lu} = \mathbf{LNq} = \mathbf{Bq} \tag{3.24}$$

where $\mathbf{B}$ is strain matrix defined as

$$\mathbf{B} = \mathbf{LN} \tag{3.25}$$

Substituting Equation (3.24) into Equation (3.10) yields

$$\boldsymbol{\sigma} = \mathbf{D}\boldsymbol{\varepsilon} = \mathbf{DBq} \tag{3.26}$$

The term corresponding to the point loads in Equation (3.20) can be re-written as $\sum_i \delta\mathbf{q}^T \mathbf{P}_i$

where the point load vector $\mathbf{P}_i$ should also be re-defined as

$$\mathbf{P}_i = \left[0,0,0,\cdots,P_{ix},P_{iy},P_{iz},\cdots,0,0,0\right]^T \tag{3.27}$$

The Galerkin weak form is applied over the local support domain Ω (with part of boundary Γ on the surface S where surface traction $\mathbf{t}$ is applied) by substituting Equations (3.21), (3.24) and (3.26) into Equation (3.20). This gives

$$\delta\mathbf{q}^T \left[\int_\Omega \mathbf{B}^T \mathbf{DB} d\Omega \mathbf{q} - \int_\Omega \mathbf{N}^T \mathbf{b} d\Omega - \int_\Gamma \mathbf{N}^T \mathbf{t} d\Gamma - \sum_i \mathbf{P}_i + \int_\Omega \rho \mathbf{N}^T \mathbf{N} d\Omega \ddot{\mathbf{q}} \right] = 0 \tag{3.28}$$

For any possible values of $\mathbf{q}$ consistent with the boundary conditions, the equation above can be satisfied only if

$$\int_\Omega \rho \mathbf{N}^T \mathbf{N} d\Omega \ddot{\mathbf{q}} + \int_\Omega \mathbf{B}^T \mathbf{DB} d\Omega \mathbf{q} = \int_\Omega \mathbf{N}^T \mathbf{b} d\Omega + \int_\Gamma \mathbf{N}^T \mathbf{t} d\Gamma + \sum_i \mathbf{P}_i \tag{3.29}$$

which leads to a set of local algebraic equations as

$$\mathbf{m}\ddot{\mathbf{q}} + \mathbf{kq} = \mathbf{f} \tag{3.30}$$

where the local mass matrix is

$$\mathbf{m} = \int_\Omega \rho \mathbf{N}^T \mathbf{N} d\Omega \qquad (3.31)$$

The local stiffness matrix is

$$\mathbf{k} = \int_\Omega \mathbf{B}^T \mathbf{D} \mathbf{B} d\Omega \qquad (3.32)$$

The local force vector is

$$\mathbf{f} = \int_\Omega \mathbf{N}^T \mathbf{b} d\Omega + \int_\Gamma \mathbf{N}^T \mathbf{t} d\Gamma + \sum_i \mathbf{P}_i \qquad (3.33)$$

In short, algebraic equations shown in Equation (3.30) among nodal displacements are obtained by satisfying the governing equations in Galerkin weak form over the local support domain Ω of each point $\mathbf{x}_Q$. Hence the local mass matrix $\mathbf{m}$, stiffness matrix $\mathbf{k}$ and force vector $\mathbf{f}$ are functions of coordinates of point $\mathbf{x}_Q$, and need to be integrated over the entire problem domain V. Usually this integration is carried out via Gauss quadrature scheme. As mentioned in Chapter 1, all Gauss points are generated together with the nodes as a by-product of the meshing process using commercial FEM packages. After that, the formation of local algebraic equations is performed over the local support domain of all these Gauss quadrature points. Finally, local algebraic equations for each Gauss point can be assembled into a set of global system equations, which is expressed as

$$\mathbf{M}\ddot{\mathbf{Q}} + \mathbf{K}\mathbf{Q} = \mathbf{F} \qquad (3.34)$$

where $\mathbf{M}$ is global mass matrix, $\mathbf{K}$ is global stiffness matrix, $\mathbf{F}$ is global force vector and $\mathbf{Q}$ is global displacement vector.

Equation (3.34) can be used to perform various kinds of stress analysis that are discussed in the next section.

3.2 Type of Analysis Solutions

3.2.1 Linear Static Analysis

Linear static analysis represents the most basic type of analysis. The term "linear" means that the computed response – displacement or stress for example, is linearly related to the applied

force. The term "static" means that the forces do not vary with time, or the time variation is insignificant and can therefore be safely ignored.

The system equations for static analysis can be obtained by removing terms related to time from Equation (3.34) as

$$\mathbf{KQ} = \mathbf{F} \tag{3.35}$$

Before solving the equation above, the essential boundary conditions are usually considered first. Similarly to FEM, the boundary condition of specified displacements can be easily handled by the penalty approach.

Assume a boundary condition

$$Q_1 = a_1 \tag{3.36}$$

where a_1 is a known specified displacement along the Degree Of Freedom (DOF) No.1 of the system. The penalty approach for handling this boundary condition is as follows:

A spring with a large stiffness C is used to model the support. In this case, one end of the spring is displaced by an amount a_1. The displacement Q_1 along DOF 1 will be approximately equal to a_1, owing to the relatively small resistance offered by the structure. Consequently, the net extension of the spring is equal to $(Q_1 - a_1)$. The strain energy in the spring equals

$$\mathbf{U_S} = \frac{1}{2}C(Q_1 - a_1)^2 \tag{3.37}$$

This strain energy contributes to the total potential energy **Π**. As a result,

$$\mathbf{\Pi} = \frac{1}{2}\mathbf{Q}^T\mathbf{KQ} + \frac{1}{2}C(Q_1 - a_1)^2 - \mathbf{Q}^T\mathbf{F} \tag{3.38}$$

The minimization of **Π** can be carried out by setting $\partial\Pi/\partial Q_i = 0$, i = 1, 2, …, N, where N is the total number of DOFs in the system. The resulting global system equations are

$$\begin{bmatrix} (K_{11} + C) & K_{12} & \cdots & K_{1N} \\ K_{21} & K_{22} & \cdots & K_{2N} \\ \vdots & \vdots & & \vdots \\ K_{N1} & K_{N2} & \cdots & K_{NN} \end{bmatrix} \begin{Bmatrix} Q_1 \\ Q_2 \\ \vdots \\ Q_N \end{Bmatrix} = \begin{Bmatrix} F_1 + Ca_1 \\ F_2 \\ \vdots \\ F_N \end{Bmatrix} \tag{3.39}$$

Here, the only modification to handle $Q_1 = a_1$ is that a large number C gets added on to the first diagonal element of $\mathbf{K}$ and that Ca_1 gets added on to F_1.

After repeating the above procedure for all DOFs where displacement boundary conditions are specified, the global system equations can be re-written as

$$\hat{\mathbf{K}}\mathbf{Q} = \hat{\mathbf{F}} \tag{3.40}$$

where $\hat{\mathbf{K}}$ and $\hat{\mathbf{F}}$ are global stiffness matrix and global force vector after penalty approach respectively.

Standard subroutine LSASF for solution of high accuracy linear system is used to solve the Equation (3.40). This standard subroutine provided by Visual Fortran Professional V6.5 can solve the real symmetric system of linear equations with iterative refinement.

Solution of Equation (3.40) yields the global displacement vector $\mathbf{Q}$. Substituting this $\mathbf{Q}$ into Equation (3.35) gives

$$\overline{\mathbf{F}} = \mathbf{K}\mathbf{Q} \tag{3.41}$$

The reaction forces can be extracted from this modified force vector $\overline{\mathbf{F}}$ in corresponding DOFs where displacement boundary conditions are specified.

Upon knowing of displacements at all nodes in the system, the strains and stresses can be obtained as per Equations (3.24) and (3.26) respectively.

3.2.2 Modal Analysis

Modal analysis computes the natural frequencies and mode shapes of a structure. The natural frequencies are the frequencies at which a structure will tend to vibrate if subjected to a disturbance. The deformed shape at a specific natural frequency is called the mode shape. Modal analysis is also called eigenvalue analysis.

In modal analysis, there is no applied load and the structure has no damping properties. Hence, the equation of motion is of the form

$$\mathbf{M}\ddot{\mathbf{Q}} + \mathbf{K}\mathbf{Q} = 0 \tag{3.42}$$

For the steady-state condition, starting from the equilibrium state, we set

$$\mathbf{Q} = \mathbf{A}\sin\omega t \tag{3.43}$$

where $\mathbf{A}$ is the vector of nodal amplitudes of vibration and ω (rad/s) is the circular frequency. Substituting Equation (3.42) for $\mathbf{Q}$ yields

$$\mathbf{KA} = \omega^2\mathbf{MA} \tag{3.44}$$

This is the generalized eigenvalue problem

$$\mathbf{KA} = \lambda\mathbf{MA} \tag{3.45}$$

where $\mathbf{A}$ is the eigenvector, representing the vibrating mode, corresponding to the eigenvalue $\lambda = \omega^2$. The frequency f in hertz (cycles per second) is obtained from $f = \omega / (2\pi)$.

Before solving Equation (3.45), boundary conditions should be incorporated. Unlike penalty approach, the rows and columns corresponding to DOFs where boundary conditions are specified can be simply eliminated from the matrix $\mathbf{K}$ & $\mathbf{M}$, which gives

$$\widetilde{\mathbf{K}}\mathbf{A} = \lambda\widetilde{\mathbf{M}}\mathbf{A} \tag{3.46}$$

where $\widetilde{\mathbf{K}}$ and $\widetilde{\mathbf{M}}$ are global stiffness matrix and global mass matrix after removing the constrained DOFs respectively.

Standard subroutine GVCSP for eigensystem analysis is used to solve the Equation (3.46). This standard subroutine provided by Visual Fortran Professional V6.5 can compute all of the eigenvalues and eigenvectors of the generalized real symmetric eigenvalue problem $\mathbf{Az} = \lambda\mathbf{Bz}$, with $\mathbf{B}$ symmetric positive definite.

3.2.3 Transient Dynamic Analysis

Transient dynamic analysis is the most general method for computing forced dynamic response. The purpose of a transient dynamic analysis is to compute the behavior of a structure subjected to time-varying excitation, which is explicitly defined in the time domain. It means that all of the forces applied to the structure are known at each instant in time.

Depending upon the structure and the nature of the loading, two different numerical methods can be used for a transient response analysis: direct and modal. In direct transient dynamic analysis, structural response is computed by solving a set of coupled equations using direct numerical integration.

Damping factor in direct transient dynamic analysis represents the energy dissipation characteristics of a structure. In this research project, a damping matrix $\mathbf{C}$ is assumed as

$$\mathbf{C} = \frac{G}{w}\mathbf{K} \tag{3.47}$$

where $\mathbf{K}$ is the global stiffness matrix, G is the overall structural damping coefficient, w is the frequency of interest in radians per unit time for the conversion of overall structural damping into equivalent viscous damping.

Adding the term of structural damping to the Equation (3.34) gives

$$\mathbf{M}\ddot{\mathbf{Q}} + \mathbf{C}\dot{\mathbf{Q}} + \mathbf{K}\mathbf{Q} = \mathbf{F} \tag{3.48}$$

Similarly to modal analysis, the boundary conditions should be considered by eliminating the rows and columns corresponding to the constrained DOFs from the matrix $\mathbf{M}$, $\mathbf{C}$, $\mathbf{K}$ and vector $\mathbf{F}$, which yields

$$\widetilde{\mathbf{M}}\ddot{\mathbf{Q}} + \widetilde{\mathbf{C}}\dot{\mathbf{Q}} + \widetilde{\mathbf{K}}\mathbf{Q} = \widetilde{\mathbf{F}} \tag{3.49}$$

where

$\widetilde{\mathbf{M}}$:   Global mass matrix after consideration of boundary conditions

$\widetilde{\mathbf{C}}$:   Global damping matrix after consideration of boundary conditions

$\widetilde{\mathbf{K}}$:   Global stiffness matrix after consideration of boundary conditions

$\widetilde{\mathbf{F}}$:   Global force vector after consideration of boundary conditions

$\mathbf{Q}$:   Global displacement vector without constrained DOFs

Structural responses such as system displacement $\mathbf{Q}_n$, velocity $\dot{\mathbf{Q}}_n$ and acceleration $\ddot{\mathbf{Q}}_n$ at discrete times (n·Δt), typically with a fixed integration time step Δt, can be computed by

solving the hyperbolic equation (3.49) via Newmark integration scheme. In order to start this integration scheme, the initial condition $\mathbf{Q}_0$ and $\dot{\mathbf{Q}}_0$ at time t = 0 is usually given.

Newmark Method

The Newmark method is a generalization of the linear acceleration method, which assumes that the acceleration varies linearly within the time interval of (t, t+Δt). It is stated as

$$\mathbf{Q}_{n+1} = \mathbf{Q}_n + \Delta t \dot{\mathbf{Q}}_n + \frac{\Delta t^2}{2}\left[(1-2\beta)\ddot{\mathbf{Q}}_n + 2\beta\ddot{\mathbf{Q}}_{n+1}\right]$$

$$\dot{\mathbf{Q}}_{n+1} = \dot{\mathbf{Q}}_n + \Delta t\left[(1-\alpha)\ddot{\mathbf{Q}}_n + \alpha\ddot{\mathbf{Q}}_{n+1}\right]$$

(3.50)

The above equations can be simplified as

$$\ddot{\mathbf{Q}}_{n+1} = a_3\left(\mathbf{Q}_{n+1} - \mathbf{Q}_n\right) - a_4\dot{\mathbf{Q}}_n - a_5\ddot{\mathbf{Q}}_n$$

$$\dot{\mathbf{Q}}_{n+1} = \dot{\mathbf{Q}}_n + a_2\ddot{\mathbf{Q}}_n + a_1\ddot{\mathbf{Q}}_{n+1}$$

(3.51)

where

$$a_1 = \alpha\Delta t$$

$$a_2 = (1-\alpha)\Delta t$$

$$a_3 = \frac{1}{\beta\Delta t^2}$$

$$a_4 = \frac{1}{\beta\Delta t}$$

$$a_5 = \frac{1}{2\beta} - 1$$

(3.52)

Equation (3.49) at time t = (n+1)Δt is

$$\widetilde{\mathbf{M}}\ddot{\mathbf{Q}}_{n+1} + \widetilde{\mathbf{C}}\dot{\mathbf{Q}}_{n+1} + \widetilde{\mathbf{K}}\mathbf{Q}_{n+1} = \widetilde{\mathbf{F}}_{n+1}$$

(3.53)

Substituting Equation (3.51) into Equation (3.53) yields

$$\left(\widetilde{\mathbf{K}} + a_3\widetilde{\mathbf{M}} + a_6\widetilde{\mathbf{C}}\right)\mathbf{Q}_{n+1}$$

(3.54)

$$= \widetilde{\mathbf{F}}_{n+1} + \left(a_3 \mathbf{Q}_n + a_4 \dot{\mathbf{Q}}_n + a_5 \ddot{\mathbf{Q}}_n\right)\widetilde{\mathbf{M}} + \left(a_6 \mathbf{Q}_n + a_7 \dot{\mathbf{Q}}_n + a_8 \ddot{\mathbf{Q}}_n\right)\widetilde{\mathbf{C}}$$

where

$$a_6 = \frac{\alpha}{\beta \Delta t}$$

$$a_7 = \frac{\alpha}{\beta} - 1 \tag{3.55}$$

$$a_8 = \frac{\Delta t}{2}\left(\frac{\alpha}{\beta} - 2\right)$$

The procedure to perform the Newmark integration scheme is as follows:

1. $\mathbf{Q}_0$ and $\dot{\mathbf{Q}}_0$ are known as initial condition

2. Compute $\ddot{\mathbf{Q}}_0$ as per $\widetilde{\mathbf{M}}\ddot{\mathbf{Q}}_0 + \widetilde{\mathbf{C}}\dot{\mathbf{Q}}_0 + \widetilde{\mathbf{K}}\mathbf{Q}_0 = \widetilde{\mathbf{F}}_0$

3. Assume $\mathbf{Q}_n$, $\dot{\mathbf{Q}}_n$ and $\ddot{\mathbf{Q}}_n$ are known with n = 0

4. Compute $\mathbf{Q}_{n+1}$ as per Equation (3.54)

5. Compute $\ddot{\mathbf{Q}}_{n+1}$ and $\dot{\mathbf{Q}}_{n+1}$ as per Equation (3.51)

6. Repeat steps 2 ~ 5 for the next time step

In Newmark method, the parameter α and β determine the stability and accuracy of the integration scheme.

Table 3.1 Special Schemes of Newmark Method

α	β	Scheme	Stability
1/2	1/4	Constant-average acceleration method	Stable
1/2	1/6	Linear acceleration method	Conditionally stable
1/2	0	Central difference method	Conditionally stable
3/2	4/5	Galerkin method	Stable
3/2	1	Backward difference method	Stable

In this research project, the Central Difference Method (CDM) and the constant-average acceleration method are used to solve the dynamic equation of motion.

3.3 Numerical Implementation of RPIM

1. Read analysis parameters

    a) Type of Radial Basis Function to be used for RPIM (EXP/MQ)

    b) RBF shape parameters

    c) Influence domain size parameter

    d) Number of Gauss points per element (for hexahedral elements only)

    e) Newmark parameters (for transient dynamic analysis only)

2. Read analysis model

    a) Analysis title

    b) Analysis type (Static / Modal / Transient dynamic)

    c) Number of mode shapes to be outputted (for modal analysis only)

    d) Time per step (solution interval), number of steps, output interval and damping coefficients (for transient dynamic analysis only)

    e) Material properties (Young's modulus / Poisson's ratio / Density)

    f) Nodal coordinates

    g) Element connectivity

    h) Boundary conditions

    i) Static nodal loads (for static analysis only) or dynamic nodal loads (for transient dynamic analysis only)

    j) DOFs in which time history to be outputted (for transient dynamic analysis only)

3. Generate Gauss points for each element and calculate weight of each Gauss point

4. Compute radius of influence domain for each node as per Equation (1.3)

5. Create material matrix **D** as per Equation (3.11)

6. Loop over all Gauss points

    a) Construct the local domain for each Gauss point to include all nodes whose influence domains cover this Gauss point

b) If the total number of nodes included in the local domain is equal or less than 10, the radius of influence domain for all nodes will be increased by 50% temporarily and go back Step a)

c) Calculate the average nodal spacing d_c as per Equation (1.2)

d) Construct shape matrix **N** as per Equation (3.23)

e) Construct strain matrix **B** as per Equation (3.25)

f) Construct local mass matrix **m** as per Equation (3.31)

g) Construct local stiffness matrix **k** as per Equation (3.32)

h) Put contribution from local mass matrix **m** into global mass matrix **M**

i) Put contribution from local stiffness matrix **k** into global mass matrix **K**

7. For modal analysis

a) Eliminate rows and columns corresponding to DOFs in which boundary conditions are specified from the global matrix **M & K**

b) Compute eigenvalues and eigenvectors using standard subroutine

c) Recover the full-dimension eigenvectors by putting back DOFs in which boundary conditions are specified

d) Output eigenvalues and eigenvectors required

8. For transient dynamic analysis

a) Eliminate rows and columns corresponding to DOFs in which boundary conditions are specified from the global matrix **M & K**

b) Construct the global damping matrix **C** as per Equation (3.47)

c) Perform the Newmark integration scheme and output the displacement time history in DOFs of interest

9. For static analysis

a) Construct the global force vector **F**

b) Modify the global stiffness matrix **K** and global force vector **F** as per penalty approach

c) Solve the global system equations and get the global displacement vector **Q** using standard subroutine

d) Calculate the total strain energy of the system

e) Compute Von Mises stresses at all Gauss points

f) Compute the average Von Mises stress for each element

g) Compute reaction forces at boundary conditions

h) Output displacements, stresses and reaction forces

The analysis procedure shown above is coded using Visual Fortran Professional v6.5 and is compiled as a solver for the basic class of linear structural analysis problems. Moreover, the pre-processor and post-processor for this analysis solver are also developed using Fortran language.

Chapter 4   RPIM for Static Analysis of 3D Solids

In this chapter, the Radial Point Interpolation Method (RPIM) is verified as an efficient tool for static analysis of 3D solids with high accuracy, via patch test and a benchmark example of cantilever beam. Meanwhile, the effect of different analysis parameters on the performance of RPIM is also investigated thoroughly. Finally, a comparison is made between RPIM and traditional finite element method.

4.1 Patch Test

Patch test has been widely used to test the performance of finite element methods. Passing the patch test serves as a sufficient requirement for a numerical method to be qualified for solid mechanics problems. The patch has at least one interior node and a linear displacement is imposed on all boundaries of the patch in the absence of body force. Satisfaction of the patch test requires that displacement at any interior node be given by the same linear function and that the strain and stress be constant in the entire patch.
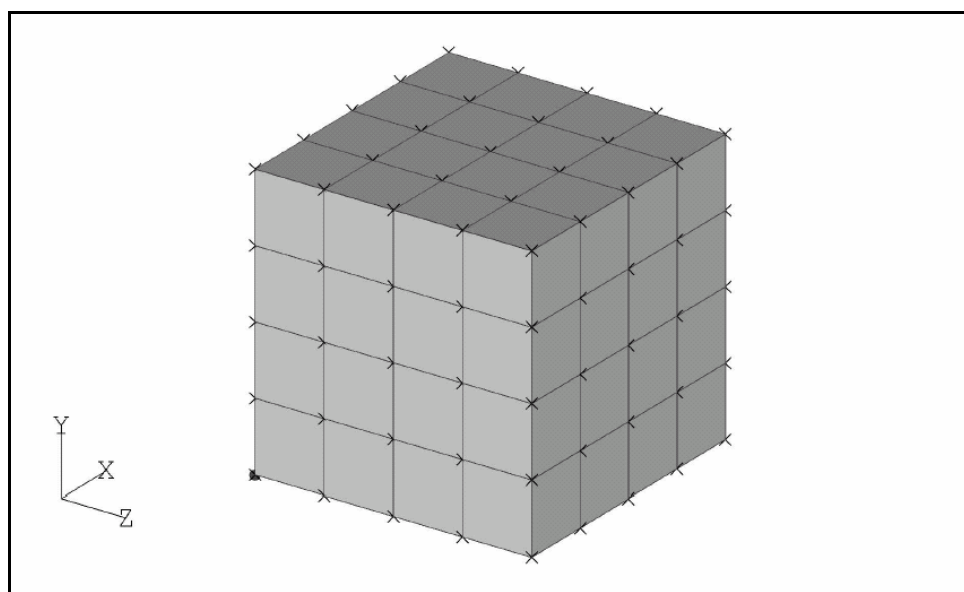

Figure 4.1   A Cubic Patch with Evenly Distributed Nodes

As shown in Figure 4.1, a three-dimensional cubic patch is used to test our Radial Point Interpolation Method. The patch size is 2 x 2 x 2 in three principal directions with the origin at one corner. The displacements are prescribed on all outside boundaries by a linear function as

$$u(x, y, z) = \begin{Bmatrix} 0.2x \\ 0.4y \\ 0.6z \end{Bmatrix} \tag{4.1}$$

The patch is discretized into 125 (= 5 x 5 x 5) nodes evenly distributed over the cube, which is assumed to be made of steel material with Young's modulus $E = 2.0 \times 10^5$, Poisson's ratio $\nu = 0.32$.

Two sets of analysis parameters are used to perform this patch test.

Set 1 - Patch Test via EXP

Type of Radial Basis Function   EXP

RBF shape parameters $\alpha_c = 0.2$

Influence domain size parameter   1.9

Set 2 - Patch Test via MQ

Type of Radial Basis Function   MQ

RBF shape parameters $\alpha_c = 1.5$ $q = 1.9$

Influence domain size parameter   1.9

Table 4.1 shows that the displacements at interior nodes are very close to the theoretical displacements defined by the linear function in Equation (4.1) with small tolerances. Table 4.2 shows that the Von Mises stress is almost constant over the whole patch with minor fluctuations. However, the errors in displacements and stresses show that RPIM does not pass the standard 3D patch test exactly.

Table 4.1   Displacements of Interior Nodes in Patch Test

Interior Node	Nodal Coordinates			Theoretical Deflection			RPIM - EXP (α = 0.2)				RPIM - MQ (α = 1.5 q = 1.9)			
	X	Y	Z	X	Y	Z	X	Y	Z	Error	X	Y	Z	Error
32	0.5	0.5	0.5	0.1	0.2	0.3	0.10268	0.20212	0.30155	0.83%	0.09696	0.19626	0.29573	1.67%
33	1	0.5	0.5	0.2	0.2	0.3	0.20074	0.20312	0.30525	1.38%	0.19977	0.19912	0.29929	0.26%
34	1.5	0.5	0.5	0.3	0.2	0.3	0.29754	0.20069	0.30156	0.06%	0.30316	0.19612	0.29568	0.50%
37	0.5	1	0.5	0.1	0.4	0.3	0.10272	0.39861	0.30372	0.32%	0.09916	0.39967	0.29895	0.20%
38	1	1	0.5	0.2	0.4	0.3	0.20089	0.40122	0.30139	0.37%	0.20032	0.39990	0.30130	0.14%
39	1.5	1	0.5	0.3	0.4	0.3	0.29830	0.39881	0.30354	0.02%	0.30083	0.39973	0.29911	0.04%
42	0.5	1.5	0.5	0.1	0.6	0.3	0.10079	0.59562	0.30470	0.24%	0.09703	0.60355	0.29605	0.14%
43	1	1.5	0.5	0.2	0.6	0.3	0.19954	0.59932	0.30169	0.00%	0.20041	0.60141	0.29905	0.13%
44	1.5	1.5	0.5	0.3	0.6	0.3	0.29857	0.59752	0.30040	0.33%	0.30318	0.60381	0.29532	0.34%
57	0.5	0.5	1	0.1	0.2	0.6	0.10203	0.20257	0.59786	0.14%	0.09939	0.19939	0.60046	0.02%
58	1	0.5	1	0.2	0.2	0.6	0.19942	0.20252	0.60306	0.51%	0.19964	0.20164	0.60074	0.16%
59	1.5	0.5	1	0.3	0.2	0.6	0.29574	0.20158	0.59955	0.25%	0.30004	0.19944	0.59978	0.05%
62	0.5	1	1	0.1	0.4	0.6	0.10140	0.39968	0.60034	0.04%	0.10116	0.40005	0.60005	0.03%
63	1	1	1	0.2	0.4	0.6	0.20052	0.40108	0.60057	0.16%	0.19991	0.40035	0.59947	0.03%
64	1.5	1	1	0.3	0.4	0.6	0.29872	0.39984	0.60091	0.02%	0.29853	0.40054	0.60001	0.04%
67	0.5	1.5	1	0.1	0.6	0.6	0.10236	0.59742	0.60076	0.12%	0.09978	0.60049	0.60020	0.05%
68	1	1.5	1	0.2	0.6	0.6	0.20152	0.59948	0.59907	0.07%	0.20014	0.59842	0.60003	0.12%
69	1.5	1.5	1	0.3	0.6	0.6	0.29955	0.59776	0.59730	0.38%	0.30122	0.60112	0.59984	0.12%
82	0.5	0.5	1.5	0.1	0.2	0.9	0.10165	0.20129	0.89516	0.46%	0.09704	0.19610	0.90408	0.30%
83	1	0.5	1.5	0.2	0.2	0.9	0.20141	0.20139	0.90025	0.09%	0.20055	0.19895	0.90156	0.15%
84	1.5	0.5	1.5	0.3	0.2	0.9	0.30135	0.20206	0.89780	0.12%	0.30384	0.19611	0.90392	0.42%
87	0.5	1	1.5	0.1	0.4	0.9	0.10104	0.39957	0.89619	0.36%	0.09986	0.39989	0.90137	0.12%
88	1	1	1.5	0.2	0.4	0.9	0.19978	0.39934	0.89998	0.03%	0.20029	0.39992	0.89873	0.11%
89	1.5	1	1.5	0.3	0.4	0.9	0.29872	0.39933	0.89838	0.20%	0.30087	0.40005	0.90133	0.14%
92	0.5	1.5	1.5	0.1	0.6	0.9	0.09966	0.59819	0.89700	0.32%	0.09635	0.60382	0.90436	0.50%
93	1	1.5	1.5	0.2	0.6	0.9	0.19654	0.59816	0.89640	0.42%	0.20010	0.60098	0.90130	0.15%
94	1.5	1.5	1.5	0.3	0.6	0.9	0.29303	0.59582	0.89397	0.79%	0.30293	0.60367	0.90442	0.56%

Table 4.2   Statistical Result of Von Mises Stresses in Patch Test

	EXP (α = 0.2)	MQ (α = 1.5 q = 1.9)
Average VM Stress	52495	52498
Standard Deviation of VM Stresses	591	432

The failure of RPIM to pass the patch test comes from the discontinuity of RPIM shape functions. When local support domains for different Gauss points are constructed, the field nodes are entering or leaving these local domains abruptly. If a Gauss point were shifted a little bit in position, the nodes might jump into or out of its local domain suddenly. Hence the RPIM shape functions based on these local domains could be discontinuous. One possible solution is the use of constrained energy principle to formulate the RPIM. Another way is to use the so-called "nodal integration" techniques (Liu and Zhang, 2005). A simple and practical way to reduce the error caused by the discontinuity of the RPIM shape functions is through the adjustment of the shape parameters of the radial basis functions used (Liu, 2002). Note that passing the standard patch test is a sufficient requirement for a method to be able to converge to the true solution as the nodal spacing approaches zero. It is not a necessary requirement for a numerical method to converge. The convergence of RPIM is proved in Section 4.2.2 via a convergence test instead.

4.2 Effect of Analysis Parameters

Effect of different analysis parameters used in RPIM is investigated through the error analysis actually. The errors introduced into the RPIM solution of static analysis can be attributed to three basic sources:

1. Error due to domain approximation

2. Error due to displacement interpolation

3. Error due to numerical computation

Error due to domain approximation can be greatly reduced by using more nodes to represent the problem domain. As for error due to displacement interpolation, RPIM shape functions play an important role. The radial basis functions used in RPIM have a wide range of shape parameters that may be tuned to minimize the interpolation error. If these parameters are not chosen properly, the accuracy of RPIM will suffer. Besides, the number of nodes included in the local domain will also affect the interpolation accuracy. The round-off errors in the

computation of numbers and errors from the numerical evaluation of integrals are categorized as the error due to numerical computation. In RPIM, the number of Gauss points used for the domain integration will affect this numerical error and thus the performance of RPIM.

In order for RPIM to produce an accurate solution of static analysis with errors as small as possible, effect of analysis parameters mentioned above should be examined carefully, and preferred range of them should be recommended. In this section, all these studies are performed through a benchmark example of cantilever beam, which is described below.
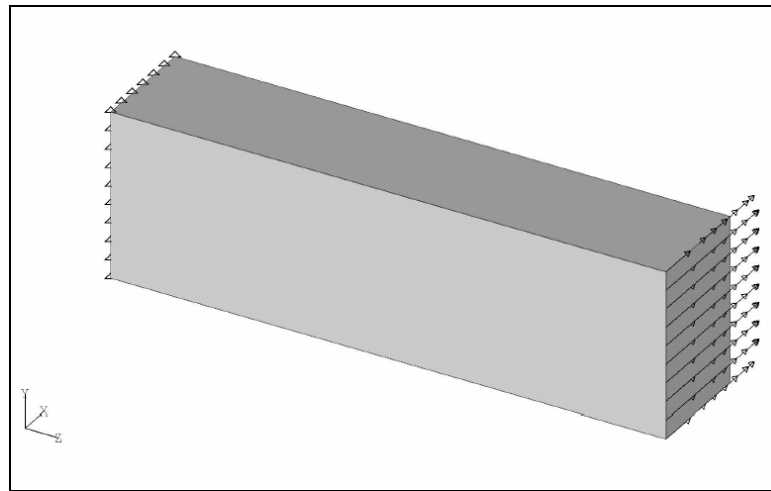
Figure 4.2   Cantilever Beam with Uniform Distributed Load at End

- Geometric size of cantilever beam
  Length in Z direction = 200 mm
  Width in X direction = 40 mm
  Height in Y direction = 60 mm

- Material properties
  Young's modulus $E = 2.0E+5$ N/mm^2
  Poisson's ratio $\nu = 0.32$

- Boundary condition
  Fixed at left end

- Loading condition
  $F_x = 12.0$ KN at right end

In order to investigate the effect of nodal distribution on the accuracy of RPIM, this cantilever beam is discretized into a set of field nodes in the following patterns:

 H132-R   132 (3 x 4 x 11) evenly distributed nodes by Hex-mesher

 H735-R   735 (5 x 7 x 21) evenly distributed nodes by Hex-mesher

 H735-IR   735 (5 x 7 x 21) unevenly distributed nodes by Hex-mesher

 T735-R   735 (5 x 7 x 21) evenly distributed nodes by Tet-mesher

 H2170-R   2170 (7 x 10 x 31) evenly distributed nodes by Hex-mesher

 H65751-R   65751 (21 x 31 x 101) evenly distributed nodes by Hex-mesher

These patterns of nodal distribution are shown in Table 4.3.

The mesh pattern H65751-R is used only by a typical FEM package – MSC-Nastran ver.70.5 to get a standard solution for the static analysis of this cantilever beam. Due to the super fine mesh of pattern H65751-R, the solution from MSC-Nastran can be used as the exact solution, upon which all the error analyses are performed. Figure 4.3 shows this standard solution with Von Mises stress superimposed on the deflected shape of cantilever beam.

Before the systematic error analysis for different RPIM parameters, the following two sets of analysis parameters are tried to solve this cantilever problem first.
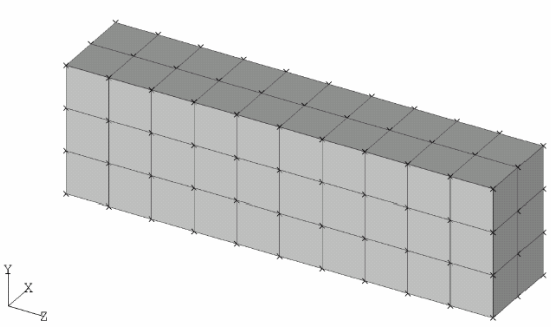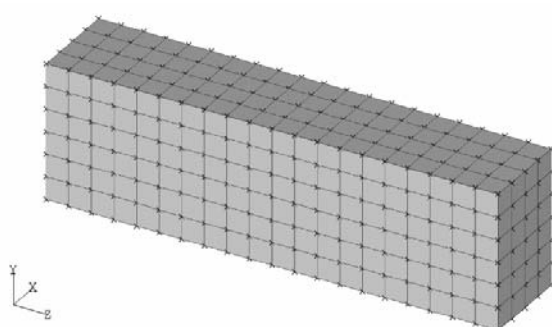
Set 1 - Trial Run via EXP
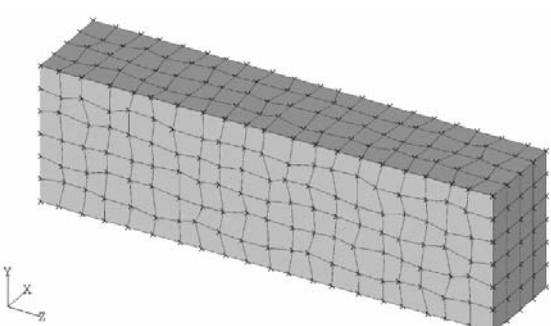
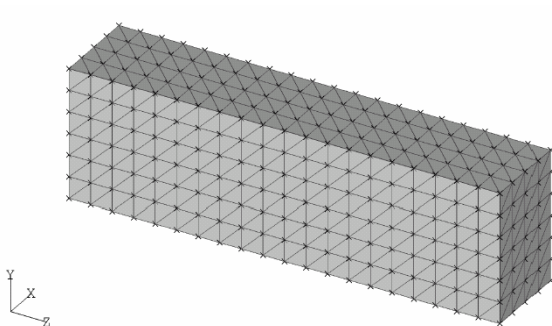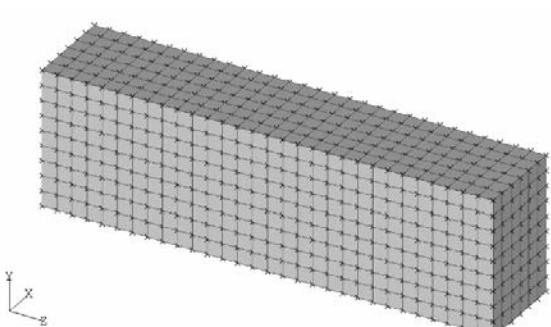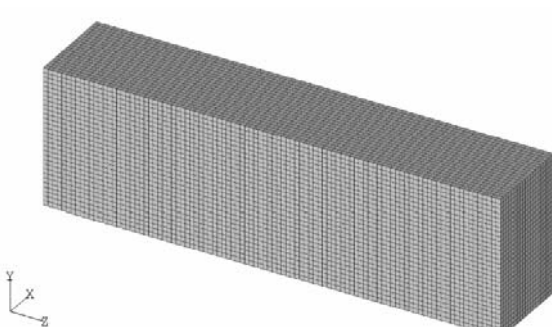 Nodal pattern   H735-R

 Type of Radial Basis Function   EXP

 RBF shape parameters $\alpha_c = 0.2$

 Influence domain size parameter   1.5

Set 2 - Trial Run via MQ

 Nodal pattern   H735-R

 Type of Radial Basis Function   MQ

 RBF shape parameters $\alpha_c = 1.5$ $q = 1.9$

 Influence domain size parameter   1.5

The trial solutions via EXP and MQ are shown in Figure 4.5 and 4.6 respectively. The FEM solution based on mesh pattern H735-R is also shown in Figure 4.4 for reference. Figure 4.7 shows the lateral deflection of cantilever beam according to the standard solution, trial run No.1 and trial run No.2.

Table 4.3   Patterns of Nodal Distribution for Cantilever Beam

H132-R

H735-R

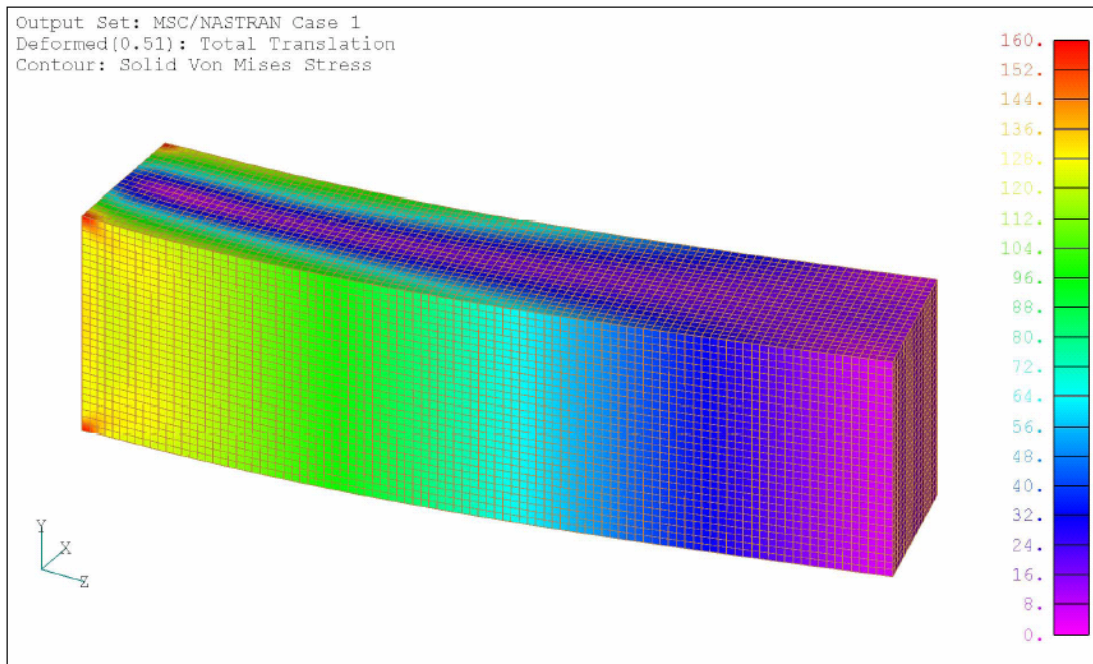H735-IR

T735-R

H2170-R

H65751-R

Figure 4.3   Cantilever Beam Standard Solution by FEM via Super Fine Mesh
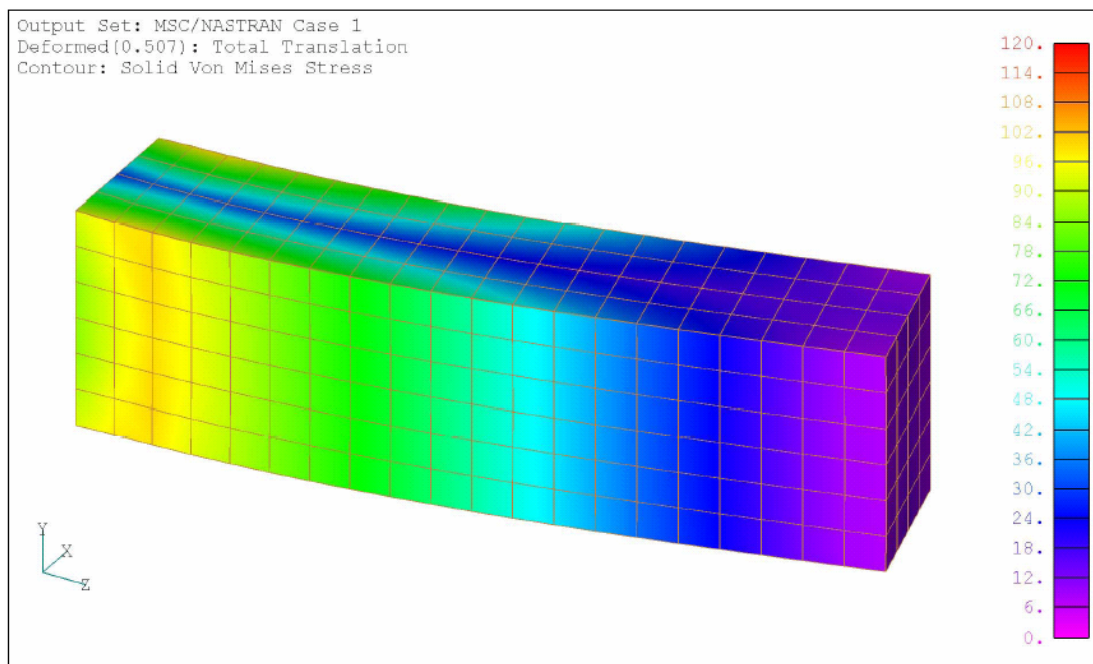

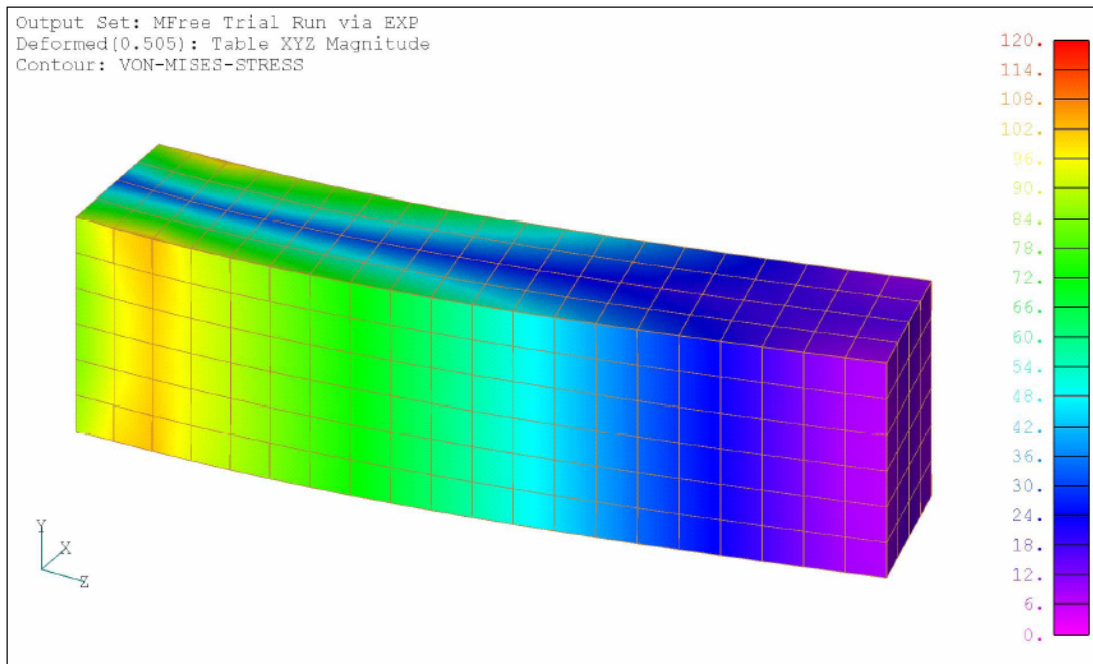**Figure 4.4**   Cantilever Beam FEM Solution via Pattern H735-R

Figure 4.5   Cantilever Beam RPIM Trial Solution via EXP with $\alpha = 0.2$
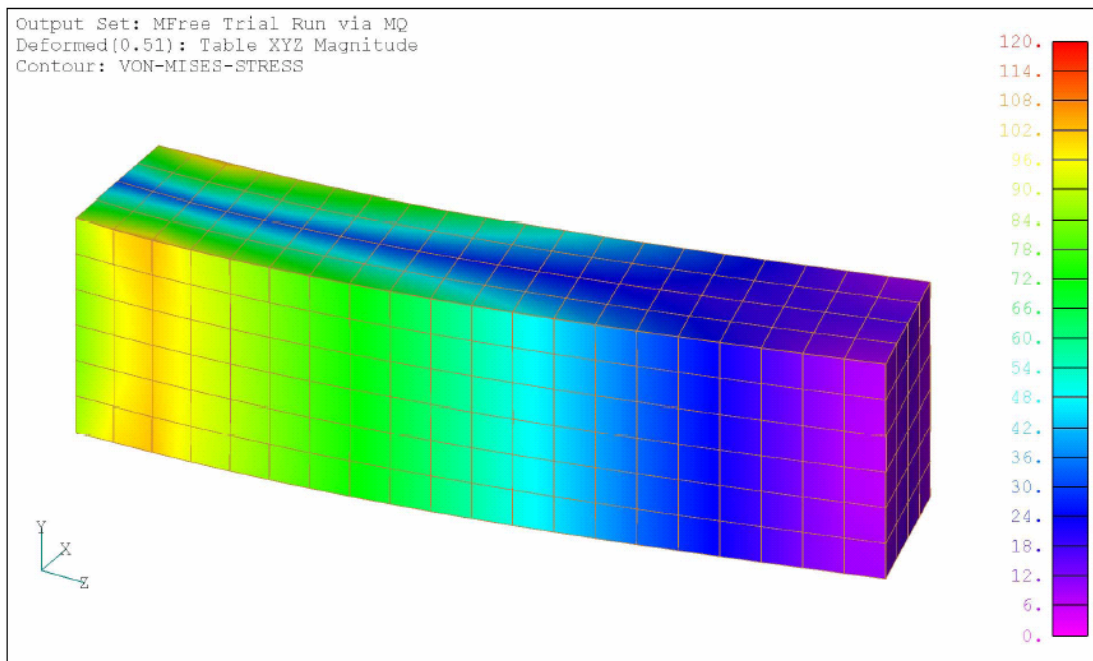

Figure 4.6   Cantilever Beam RPIM Trial Solution via MQ with $\alpha = 1.5$ q = 1.9
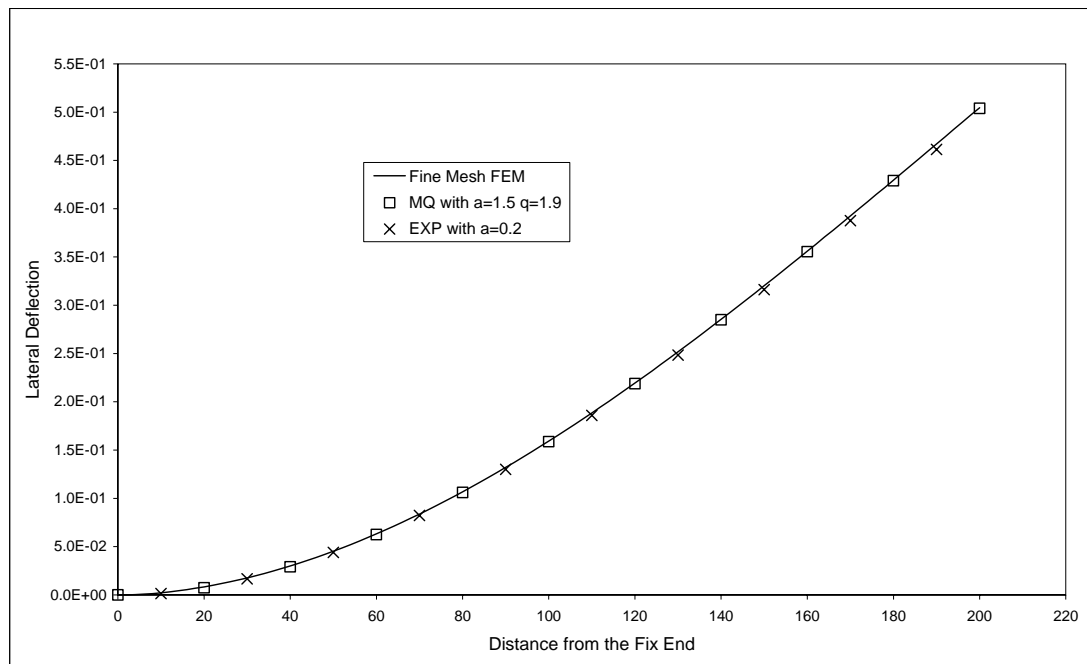
Figure 4.7 Cantilever Beam Lateral Deflection by FEM and RPIM

It can be seen from Figure 4.4 ~ 4.6 that RPIM via EXP, RPIM via MQ, and FEM almost generate the identical stress contour and deflection plot. Similar situation also happens on the lateral deflection of cantilever beam shown in Figure 4.7. This indicates that the RPIM can produce the static analysis solutions as good as that by FEM. On the other hand, it is almost impossible to distinguish the effect of different RPIM analysis parameters through the stress contour and deflection plots. Therefore, the system strain energy instead is used as the measure for the following error analysis. For the example of this cantilever beam, the exact value of system strain energy under loads at end is 3.028E+3 N-mm as per FEM solution via super fine mesh.

4.2.1 RBF Shape Parameters

In order to investigate the effect of RBF shape parameters on the accuracy of RPIM without influences from other analysis parameters, those parameters are fixed as follows:

Nodal pattern   H735-R or H735-IR

Influence domain size parameter   1.5

Number of Gauss points per Hex-element   8

Shape parameter for EXP is studied first, followed by that for MQ.

EXP Shape Parameter

The effect of EXP shape parameter on RPIM accuracy is illustrated in Figure 4.8. The findings from this figure are summarized as follows:

- For regular nodal distribution, analysis results are not sensitive to the EXP shape parameter α_c when $\alpha_c > 0.03$. The analysis results worsen rapidly when α_c decreases beyond 0.03.

- For irregular nodal distribution, α_c has a similar effect on the analysis results except that the critical value of α_c is around 0.12.

- Further studies indicate that this critical value of EXP shape parameter α_c increases with the level of irregularity of nodal distribution.

- The preferred range of EXP shape parameter α_c is from 0.2 to 1.0. This is close to the range recommended by 3D function fitting in Chapter 2.

MQ Shape Parameters

The effect of MQ shape parameters on RPIM accuracy is illustrated in Figures 4.9 and 4.10. The findings from these figures are summarized as follows:

- For regular nodal distribution, small errors are observed when q is around 2.0 for all values of α_c examined. However, q = 2.0 can not be chosen due to singularity of moment matrix. Similar findings can be seen from the 3D function fitting in Chapter 2.

- For irregular nodal distribution, the optimal value of q changes with α_c.

- The preferred range of MQ shape parameters is $\alpha_c = 0.5 \sim 2.0$, q = 0.4 $\sim$ 2.2 except integers. This is also close to the range recommended by 3D function fitting.
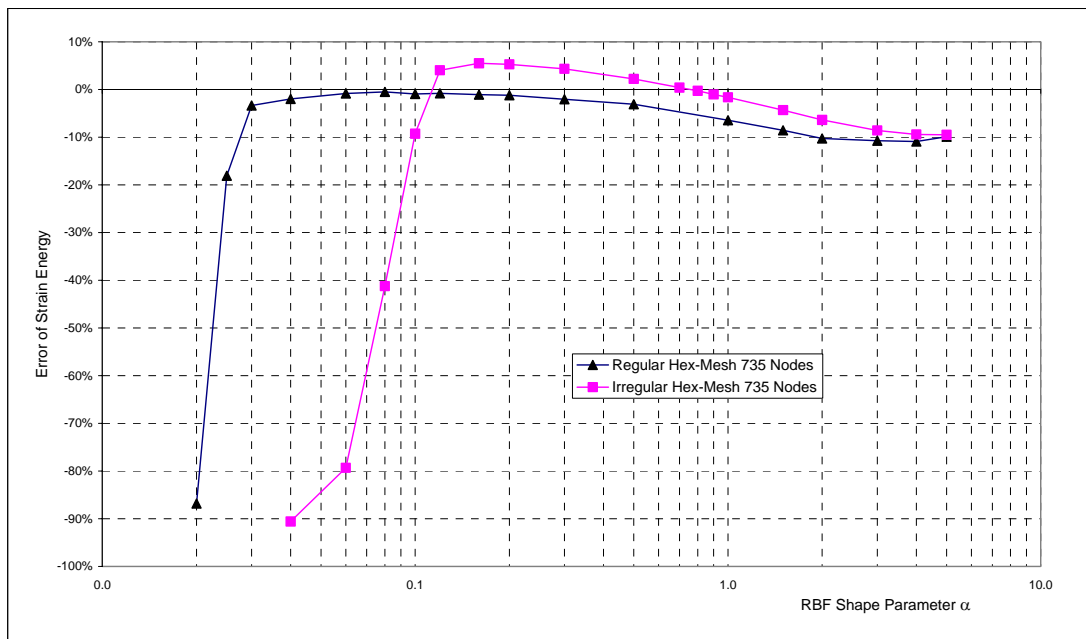
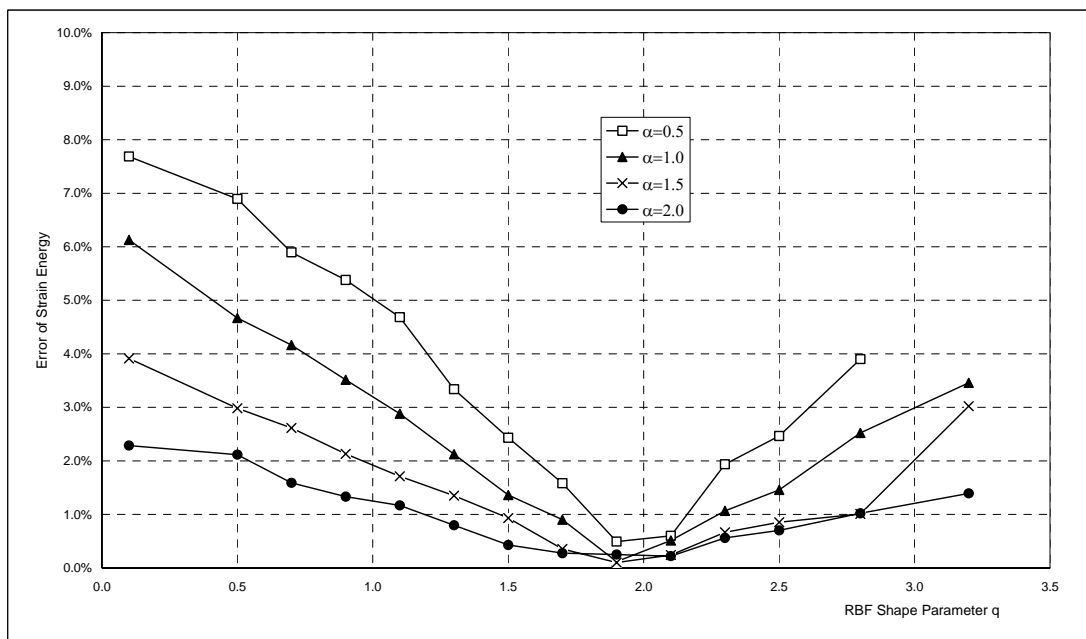**Figure 4.8**   Effect of EXP Shape Parameter α on RPIM Accuracy

Figure 4.9   Effect of MQ Shape Parameters α and q on RPIM Accuracy

(based on regular nodal distribution)
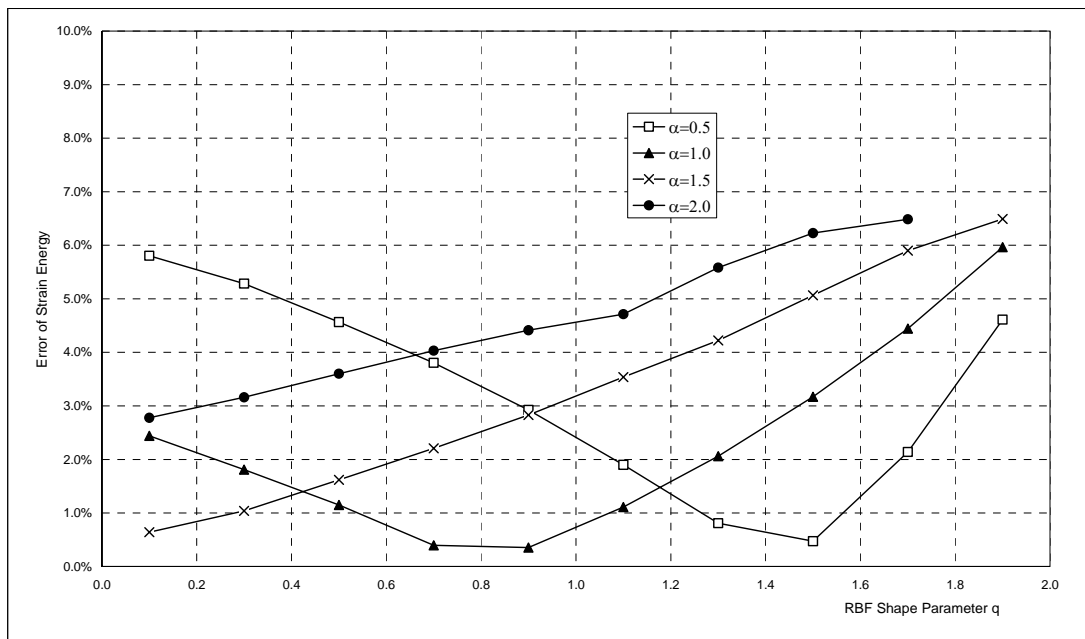
Figure 4.10   Effect of MQ Shape Parameters α and q on RPIM Accuracy

(based on irregular nodal distribution)

4.2.2 Nodal Density – Convergence of Solution

The nodal pattern H132-R, H735-R and H2170-R that have different nodal densities are used together with four typical settings of RBF shape parameters and a fixed influence domain size parameter of 1.5 to solve this static problem of cantilever beam. The variation in error of strain energy with the characteristic nodal spacing h is plotted on Figure 4.11. It indicates that the RPIM solution is convergent to the true solution with the increase of nodal density. However, the convergence rate depends on the RBF shape parameters.

Figure 4.11   Effect of Nodal Density on RPIM Accuracy

Figure 4.12   Effect of Influence Domain Size Parameter on RPIM Accuracy
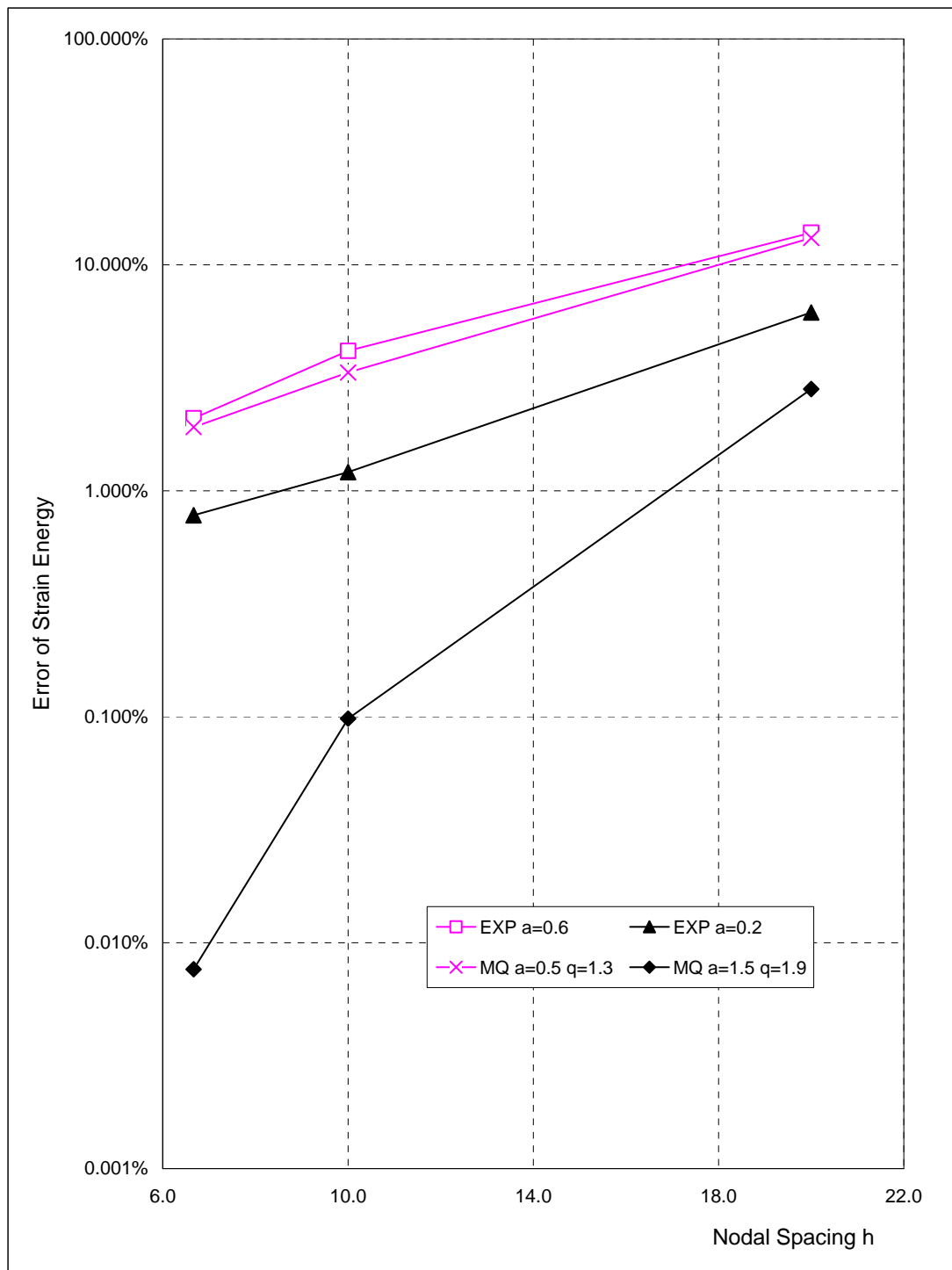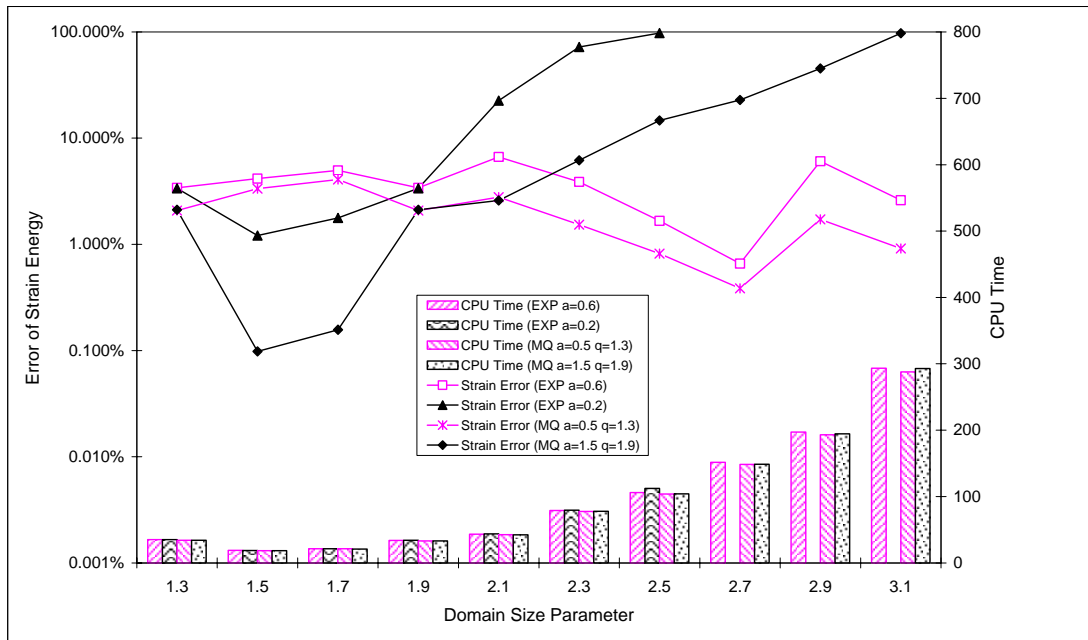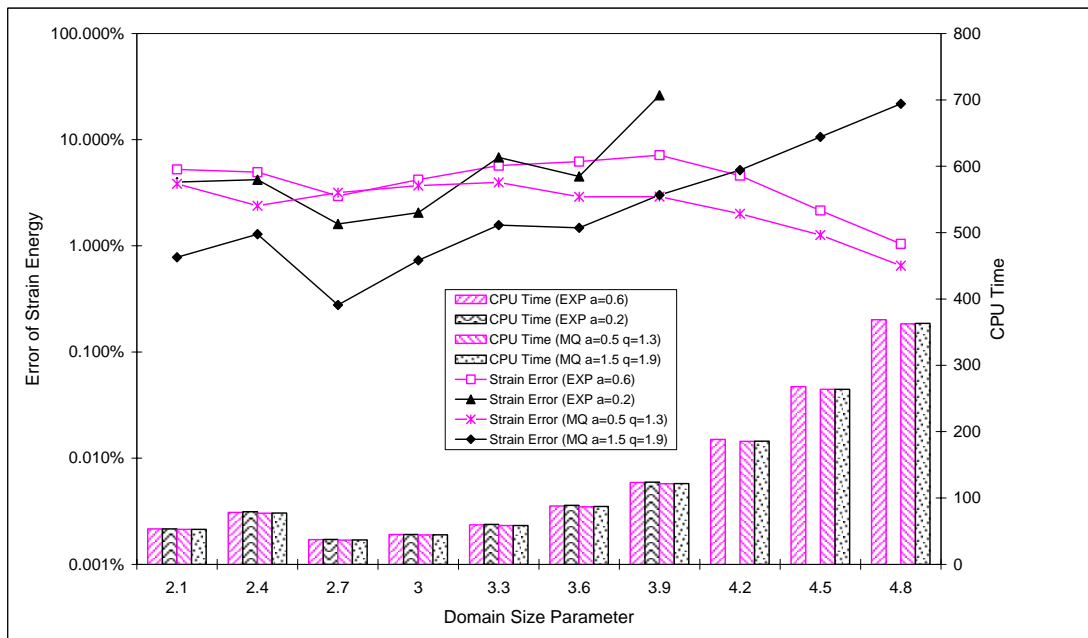
(nodes generated by Hex-mesher)

Figure 4.13   Effect of Influence Domain Size Parameter on RPIM Accuracy

(nodes generated by Tet-mesher)

4.2.3 Influence Domain Size Parameter

A series of influence domain size parameters are used together with four typical settings of RBF shape parameters and two nodal patterns (H735-R and T735-R) to produce the RPIM solutions for this cantilever example. The effect of influence domain size parameter on the accuracy and efficiency of RPIM is shown in Figure 4.12 and 4.13. The findings from these figures are summarized as follows:

- Bigger value of influence domain size parameter does not ensure better accuracy, but does cause longer computer time and thus lower efficiency. Similar effect of support domain size parameter on fitting quality of 3D functions is observed in Chapter 2 also. This phenomenon can partially be attributed to the bigger numerical error caused by more numerical operations when influence domain size parameter increases.

- Because the influence domain size of all nodes may have to be increased so as to ensure that at least 11 nodes can be included in the local domain of all Gauss points, a little bit more CPU time is spent to adjust the influence domain size temporarily when the influence domain size parameter is very small (1.3 for Hex-mesh and 2.1~2.4 for Tet-mesh).

- The optimal values of influence domain size parameter are 1.5 and 2.7 for Hex-mesh and Tet-mesh respectively. As a result, about $11 \sim 30$ nodes will be included in the local domain of Gauss points for both cases. According to Equation (1.3) that is used to calculate the radius of influence domain, larger value of influence domain size parameter is needed for Tet-mesh case than that is needed for Hex-mesh case.

- The contributive factor underlie the influence domain size parameter is the number of nodes included in the local domain of Gauss points actually.
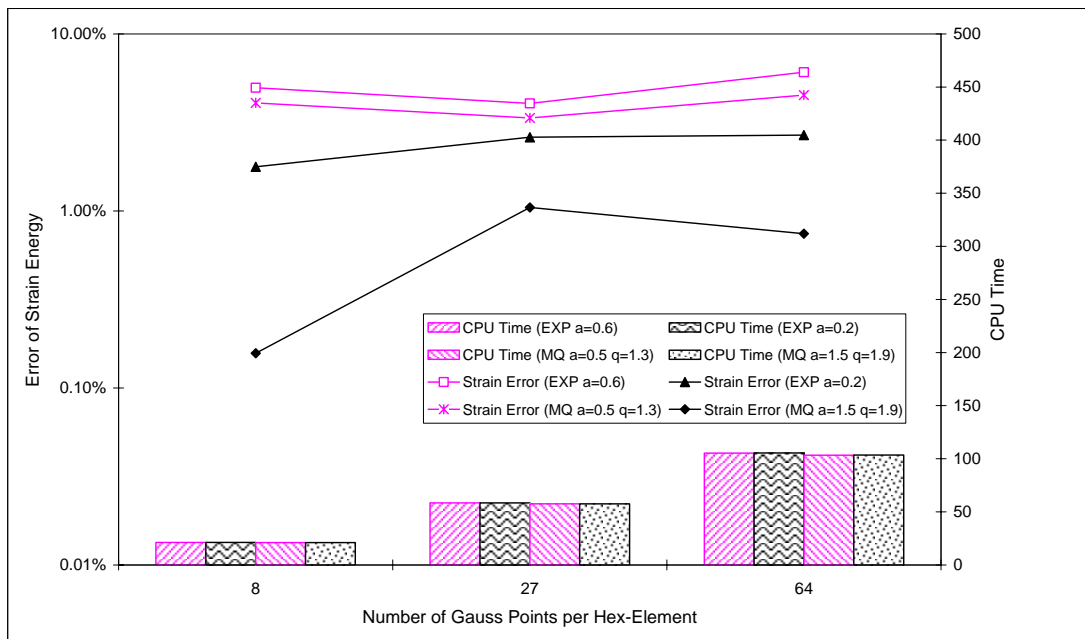
Figure 4.14   Effect of Number of Gauss Points on RPIM Accuracy

4.2.4 Number of Gauss Points per Element

In order to investigate the effect of the number of Gauss points per element on the accuracy and efficiency of RPIM without disturbances from other analysis parameters, those parameters are fixed as follows:

Nodal pattern   H735-R

RBF shape parameters   Typical settings

Influence domain size parameter   1.7

The error of strain energy and total CPU time are plotted with different number of Gauss points per Hex-element on Figure 4.14. It shows that more Gauss points per Hex-element does not ensure better accuracy, but does cause longer computer time and thus lower efficiency. This phenomenon might be well explained by the increased number of numerical operations during the domain integration using more Gauss points. In this research project, 8 Gauss points and 4 Gauss points are recommended for Hex-element and Tet-element respectively.

4.3 Comparison between RPIM and FEM

FEM is presently the most popular numerical tool for mechanical simulations. It is being commonly recognized and widely used by engineers from almost all industries. In order to have a direct evaluation of RPIM, it is compared with FEM via the same example of cantilever beam.

Table 4.4 Comparison between RPIM and FEM for Cantilever Beam Static Analysis

Mesh Pattern	MSC-Nastran V70.5		EXP ($\alpha = 0.6$)		MQ ($\alpha = 1.5$ q = 1.9)	
	Energy Error	CPU Time	Energy Error	CPU Time	Energy Error	CPU Time
H132-R	1.65%	25.12 s	13.88%	0.92 s	2.82%	0.90 s
H735-R	0.66%	26.43 s	4.16%	18.74 s	0.10%	18.60 s
H735-IR	1.06%	26.49 s	1.23%	22.16 s	6.49%	22.26 s
T735-R	19.88%	27.18 s	2.95%	37.20 s	0.28%	36.78 s
H2170-R	0.35%	30.57 s	2.09%	241.2 s	0.01%	243.1 s
H65751-R	0.00%	5708.2 s	-	-	-	-

Note: Influence domain size parameters are 1.5 and 2.7 for Hex-mesh and Tet-mesh respectively.

RPIM and FEM are used to solve this static problem of cantilever beam. The error of strain energy and CPU time are listed in Table 4.4, from which the following are observed.

- RPIM produces the analysis results with similar level of accuracy as FEM does when Hex-mesh is used.

- RPIM produces much more accurate results than FEM does when Tet-mesh (T735-R) is used.

- For small model with fewer nodes, the RPIM spends less CPU time than MSC-Nastran does. However, it is also noticed in Table 4.4 that the CPU time of MSC-Nastran only increases from 25.12s to 30.57s when the number of nodes increases by 16 times (from 132 to 2170). It indicates that MSC-Nastran might spend a part of CPU time to do other jobs, like creating database. For small models, this part of CPU time may be significantly longer than that used in solving the model, and hence the total CPU time used by MSC-Nastran for small models are longer than that used by RPIM. Therefore, it

is appropriate to conclude that RPIM and FEM have compatible efficiency in solving small models.

- The RPIM speed drops rapidly when the total number of nodes increases beyond about 1000. It does not mean that RPIM is slower for big model size. We once studied the constitution of the global stiffness matrix for a typical analysis problem and found that the global stiffness matrix is a 2D sparse matrix with more than 99% of its elements are zeros. Global matrices usually have huge size and take up a large amount of computer memory. Hence, none of commercial FEM software (including MSC-Nastran) will store the global matrices directly in the memory. They normally make some modifications to the numerical methods and store only non-zero elements of global matrices in the memory. Actually the same thing could be done in our RPIM, but it is out of the scope of this research project. Instead, we make use of hard disk space to compensate the computer memory so that RPIM can carry out the analysis for big-size model. The numerical operations through hard disk are much slower than that within computer memory. When the model is so big that computer memory cannot hold all the data (especially global matrices) used by analysis program, RPIM will shift a considerable amount of data to the hard disk and perform the numerical operations by frequently hard disk reading and writing. This is exactly the reason why RPIM seems slower for analysis with big model size. If some numerical modifications were made on RPIM, its speed would be faster than that shown in Table 4.4.

Chapter 5   RPIM for Dynamic Analysis of 3D Solids

As described in Chapter 3, RPIM can be used for dynamic analysis of 3D solids as well as static analysis. In this chapter, the accuracy of RPIM for dynamic analysis is verified through the same benchmark example of cantilever beam. Because of the identical procedure to construct the global stiffness matrix by RPIM for both static analysis and dynamic analysis, the most analysis parameters recommended by RPIM static analysis in Chapter 4 will be directly used for dynamic analysis without any optimization.

5.1 Modal Analysis

First of all, a standard solution of modal analysis for the cantilever beam is obtained by running MSC-Nastran over the fine mesh H65751-R. Mode shapes of the first six orders are plotted on Figure 5.1, from which the different vibration modes can be identified as

Mode 1   Bending about Y-axis with single wave

Mode 2   Bending about X-axis with single wave

Mode 3   Twist about Z-axis

Mode 4   Bending about Y-axis with two waves

Mode 5   Bending about X-axis with two waves

Mode 6   Elongation (lengthen or shorten) along Z-axis

Modal analysis results by RPIM using some typical settings of analysis parameters are summarized in Table 5.1 and 5.2, with Table 5.1 for results via mesh pattern H735-R and Table 5.2 for results via mesh pattern T735-R. Besides, the results by MSC-Nastran are also included for comparison.
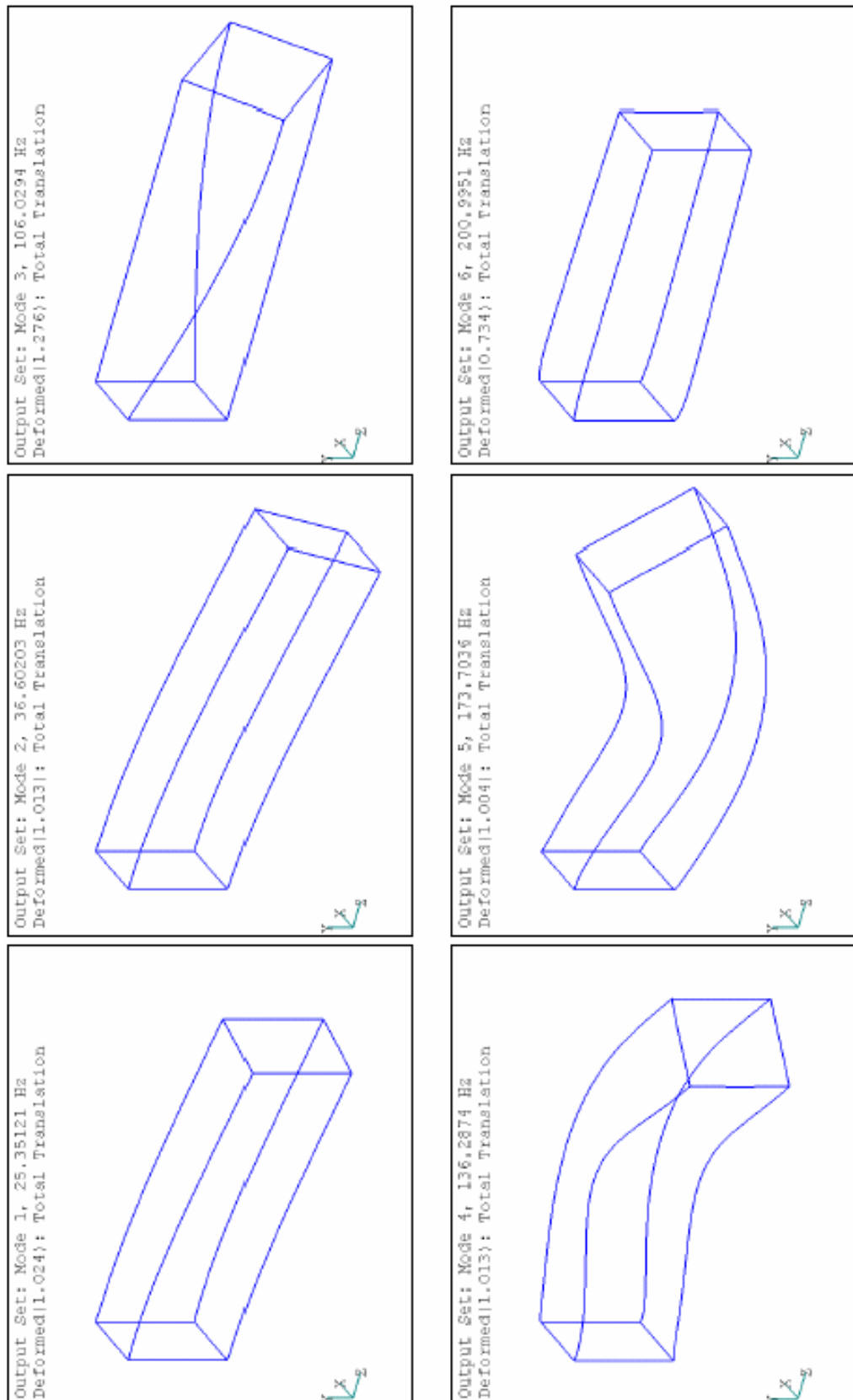
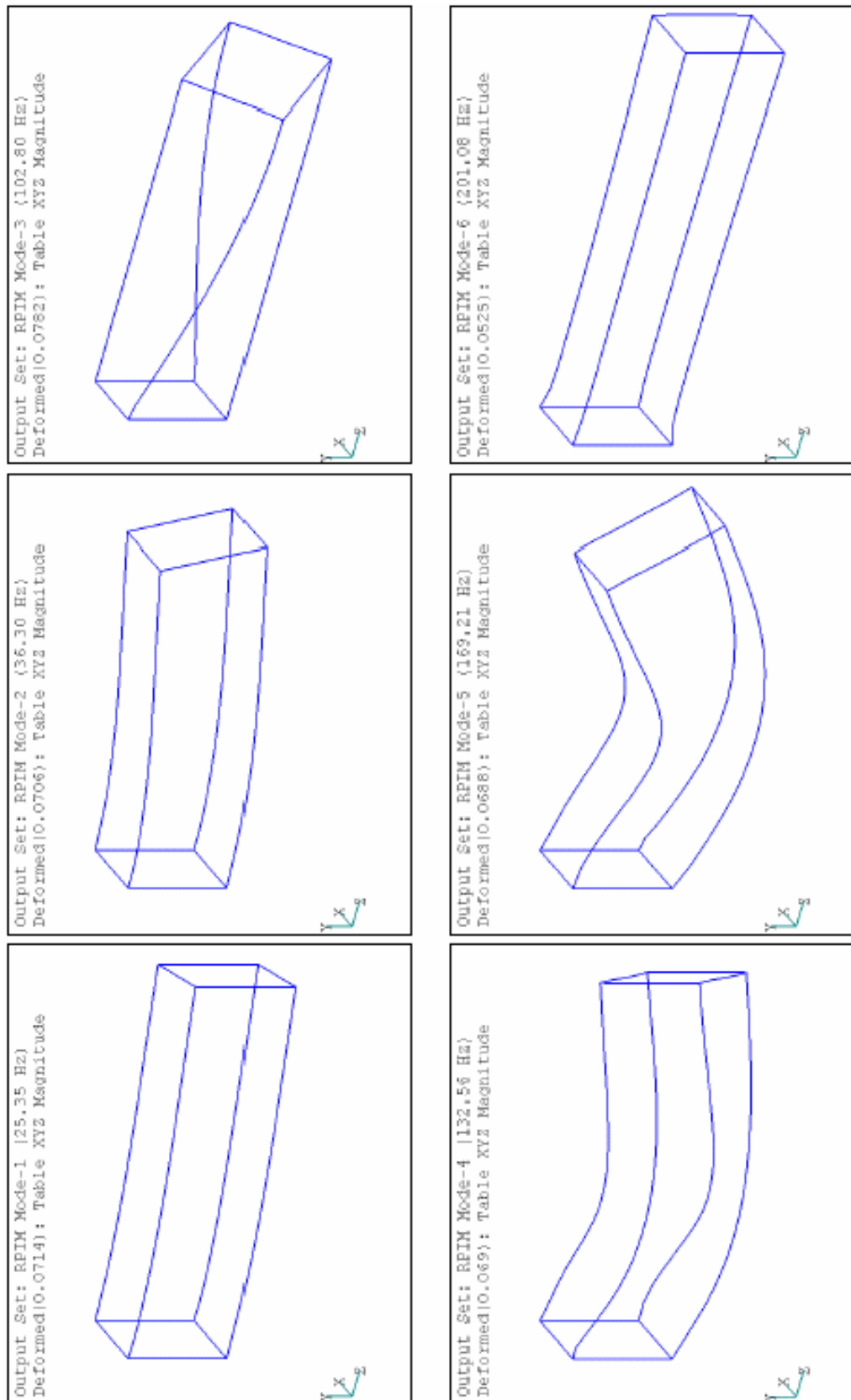**Figure 5.1**   Mode Shapes of Cantilever Beam by Fine Mesh FEM (standard solution)

Figure 5.2   Mode Shapes of Cantilever Beam by RPIM (MQ $\alpha = 1.5$ $q = 1.9$ Hex-mesh)

Table 5.1   Eigenvalues of Cantilever Beam by RPIM and FEM via Hex-mesh

Mesh Pattern	RBF Parameters			Domain Size Parameter	Normal Modes Analysis Results	Mode 1	Mode 2	Mode 3	Mode 4	Mode 5	Mode 6
	Type	α	q								
H65751-R	Fine Mesh FEM (Standard Results)			-	Eigenvalue	25372	52890	443825	733282	1191180	1594890
					Frequency (Hz)	25.35	36.60	106.03	136.29	173.70	201.00
					Error	-	-	-	-	-	-
H735-R	FEM			-	Eigenvalue	25499	53162	427020	735810	1193528	1598762
					Frequency (Hz)	25.41	36.70	104.00	136.52	173.87	201.24
					Error	0.501%	0.515%	3.787%	0.345%	0.197%	0.243%
H735-R	EXP	0.2	-	1.5	Eigenvalue	25938	52530	423315	699972	1135318	1596021
					Frequency (Hz)	25.63	36.48	103.55	133.16	169.58	201.07
					Error	2.231%	0.680%	4.621%	4.543%	4.690%	0.071%
H735-R	EXP	0.6	-	1.5	Eigenvalue	26377	53938	440585	721579	1153897	1596853
					Frequency (Hz)	25.85	36.96	105.64	135.20	170.96	201.12
					Error	3.960%	1.982%	0.730%	1.596%	3.130%	0.123%
H735-R	MQ	0.5	1.3	1.5	Eigenvalue	26464	53366	441672	722813	1158061	1597540
					Frequency (Hz)	25.89	36.77	105.77	135.31	171.27	201.16
					Error	4.303%	0.901%	0.485%	1.428%	2.780%	0.166%
H735-R	MQ	1.5	1.9	1.5	Eigenvalue	25365	52014	417164	693748	1130401	1596192
					Frequency (Hz)	25.35	36.30	102.80	132.56	169.21	201.08
					Error	0.030%	1.655%	6.007%	5.391%	5.102%	0.082%

Table 5.2   Eigenvalues of Cantilever Beam by RPIM and FEM via Tet-mesh

Mesh Pattern	RBF Parameters			Domain Size Parameter	Normal Modes Analysis Results	Mode 1	Mode 2	Mode 3	Mode 4	Mode 5	Mode 6
	Type	α	q								
H65751-R	Fine Mesh FEM (Standard Results)			-	Eigenvalue	25372	52890	443825	733282	1191180	1594890
					Frequency (Hz)	25.35	36.60	106.03	136.29	173.70	201.00
					Error	-	-	-	-	-	-
T735-R	FEM			-	Eigenvalue	31469	59142	545796	873212	1293377	1609042
					Frequency (Hz)	28.23	38.71	117.58	148.72	181.00	201.88
					Error	24.028%	11.821%	22.975%	19.083%	8.579%	0.887%
T735-R	EXP	0.2	-	2.7	Eigenvalue	25476	53256	426923	719644	1164497	1595418
					Frequency (Hz)	25.40	36.73	103.99	135.01	171.75	201.03
					Error	0.409%	0.692%	3.808%	1.860%	2.240%	0.033%
T735-R	EXP	0.6	-	2.7	Eigenvalue	26414	53573	439359	732277	1174311	1595856
					Frequency (Hz)	25.87	36.84	105.49	136.19	172.47	201.06
					Error	4.108%	1.291%	1.006%	0.137%	1.416%	0.061%
T735-R	MQ	0.5	1.3	2.7	Eigenvalue	26424	53549	443736	736251	1177794	1596571
					Frequency (Hz)	25.87	36.83	106.02	136.56	172.72	201.10
					Error	4.146%	1.246%	0.020%	0.405%	1.124%	0.105%
T735-R	MQ	1.5	1.9	2.7	Eigenvalue	25027	52904	422487	714272	1159624	1595428
					Frequency (Hz)	25.18	36.61	103.45	134.51	171.39	201.03
					Error	1.362%	0.028%	4.808%	2.592%	2.649%	0.034%

Mode shapes of cantilever beam generated by one of the RPIM runs are plotted on Figure 5.2. By a direct comparison between Figure 5.1 and Figure 5.2, it can be concluded that RPIM can generate all mode shapes correctly, except that the cantilever beam may deflect in the opposite direction for some modes.

As for the accuracy of modal analysis via RPIM, Table 5.1 shows that RPIM produces the modal analysis results with similar level of accuracy as FEM does when Hex-mesh is used. However, when Tet-mesh is used, Table 5.2 shows that RPIM is much more accurate than FEM. It confirms the similar conclusion from the static analysis in Chapter 4.

5.2 Transient Dynamic Analysis

Transient dynamic analysis for the cantilever beam that is discretized per mesh pattern H735-R is performed using RPIM and FEM to produce the time-history of displacement, velocity and acceleration at all nodes. Here, only the displacement in X-direction at the center of cantilever end (node 718) is plotted for simplicity.

5.2.1 Cantilever under Harmonic Load (without Damping)

Assume that the load applied at the end of cantilever beam ($F_x = 12$ KN) varies with a function $f(t) = \sin(\omega t)$, where $\omega = 160$ rad/sec is the frequency of the dynamic load. No damping is considered in this case. Both FEM and RPIM are used to solve this dynamic problem. For FEM, the time step is fixed at $\Delta t = 1.0E-4$ sec. For RPIM, the analysis parameters are chosen as

Type of Radial Basis Function	MQ
RBF shape parameters	$\alpha_c = 1.5$ $q = 1.9$
Influence domain size parameter	1.5
Integration scheme	CDM or Newmark
Newmark parameters	$\alpha = 0.5$ $\beta = 0.25$

The time-history of X-displacement at node 718 is plotted on Figure 5.3. It can be seen that CDM with $\Delta t = 5.0E-6$ sec produces results in good agreement with FEM. When $\Delta t > \Delta t_{critical} \approx 1.0E-5$ sec, CDM will become unstable. On the contrary, the Newmark method (constant-average acceleration method) is always stable for any time step. As shown in Figure 5.3, Newmark method with $\Delta t = 5.0E-5$ sec and $\Delta t = 5.0E-4$ sec produces very good results. It indicates that CDM is conditionally stable and Newmark method ($\alpha=0.5$, $\beta=0.25$) is unconditionally stable. However, the numerical error would increase with the time step in Newmark method. It can be seen from Figure 5.3 that the accuracy of Newmark method is not acceptable when the time step is too big (e.g. $\Delta t = 5.0E-3$ sec).

Due to the unconditional stability of Newmark method, a big time step can be used with it for the forced vibration analysis, thus the computer time can be saved. The Newmark method (constant-average acceleration method) is always used by default in the transient dynamic analysis hereinafter.

5.2.2 Cantilever under Harmonic Load (with Damping)

Same harmonic load as before is applied at the cantilever end. However, structural damping is considered at this time. The RPIM is used to solve this dynamic problem with the setting of analysis parameters as follows:

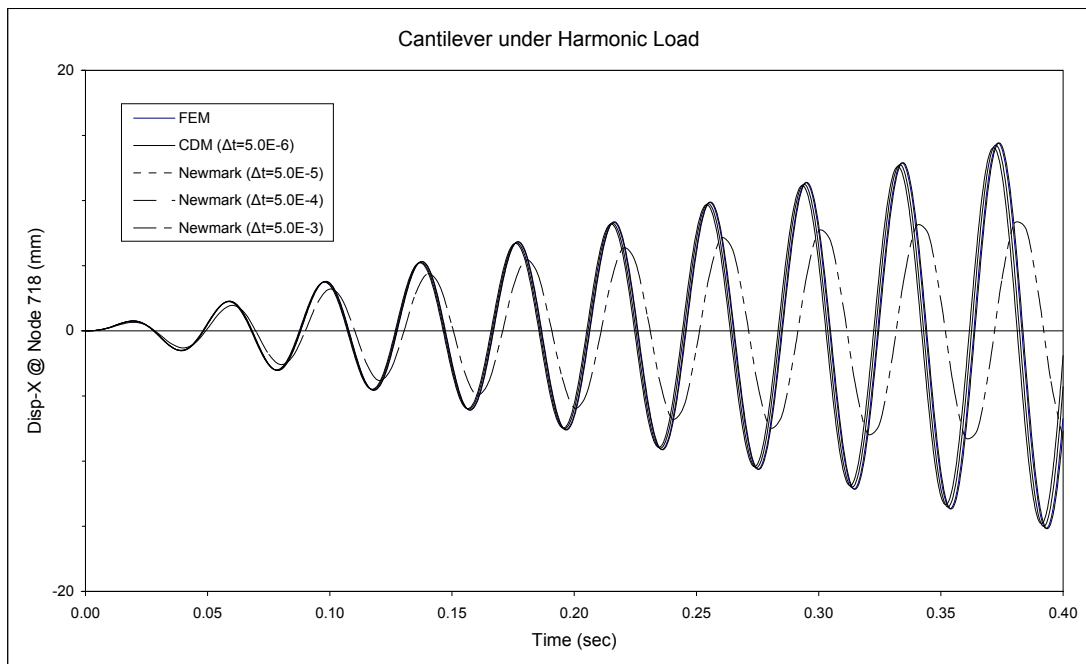|	
Type of Radial Basis Function	EXP
RBF shape parameters	$\alpha_c = 0.2$
Influence domain size parameter	1.5
Integration scheme	Newmark
Newmark parameters	$\alpha = 0.5$ $\beta = 0.25$
Time step	2.0E-4 sec
Overall structural damping coefficient	0.015
Frequency corresponding to damping	157.08 rad/sec

Figure 5.3   Transient Response of Cantilever Beam under Harmonic Load
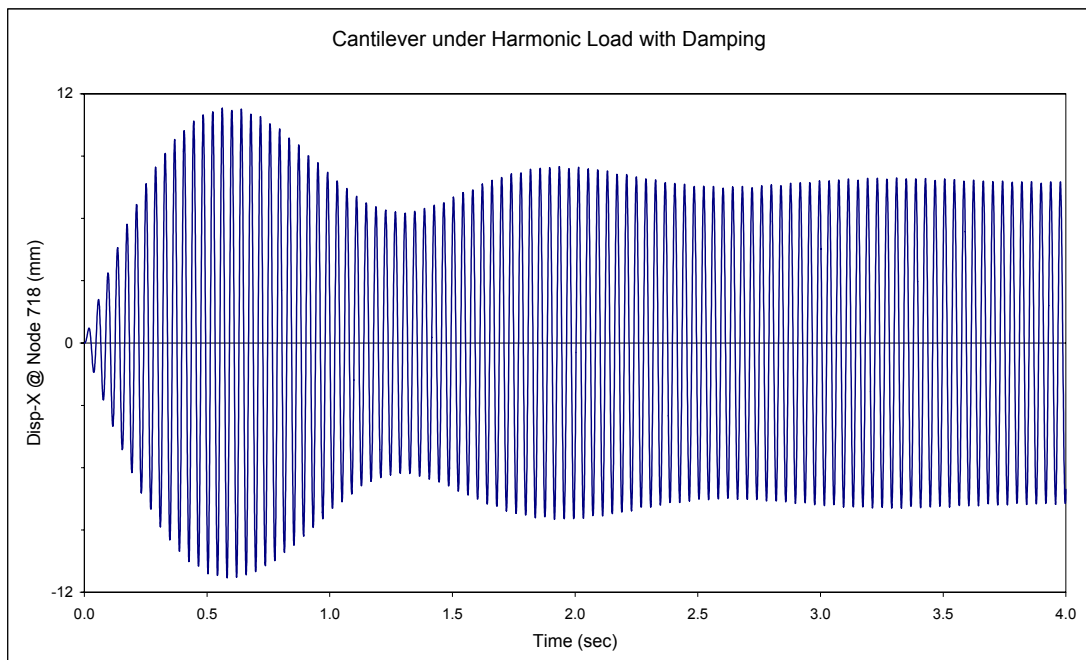(without damping)

Figure 5.4   Transient Response of Cantilever Beam under Harmonic Load
(with damping, by RPIM)

As shown in Figure 5.4, the computed time-history of X-displacement at node 718 is quite close to what is expected.

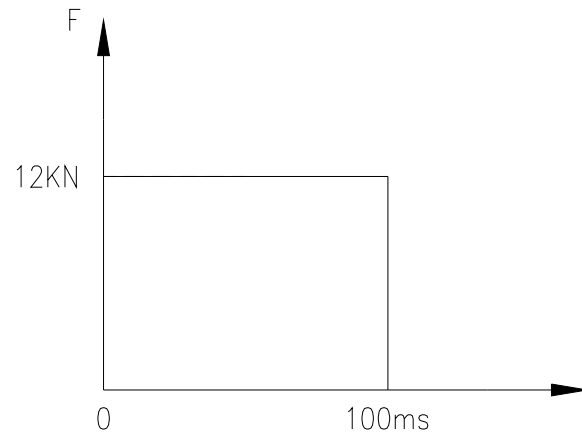### 5.2.3   Cantilever under Rectangular Impulse (without Damping)

Figure 5.5   12KN Rectangular Impulse with Duration 100ms

Assume that a rectangular impulse shown in Figure 5.5 is applied at the end of cantilever beam without consideration of damping. Both FEM and RPIM are used to solve this dynamic problem. For FEM, the time step is fixed at Δt = 1.0E-4 sec. For RPIM, the analysis parameters are chosen as

Type of Radial Basis Function	MQ
RBF shape parameters	α_c = 1.5 q = 1.9
Influence domain size parameter	1.5
Integration scheme	Newmark
Newmark parameters	α = 0.5 β = 0.25
Time step	1.0E-4 sec

The time-history of X-displacement at node 718 that are generated by FEM and RPIM are plotted on Figure 5.6 and Figure 5.7 respectively. By a direct comparison between these two figures, it can be concluded that RPIM can carry out the transient dynamic analysis as accurate as FEM does.
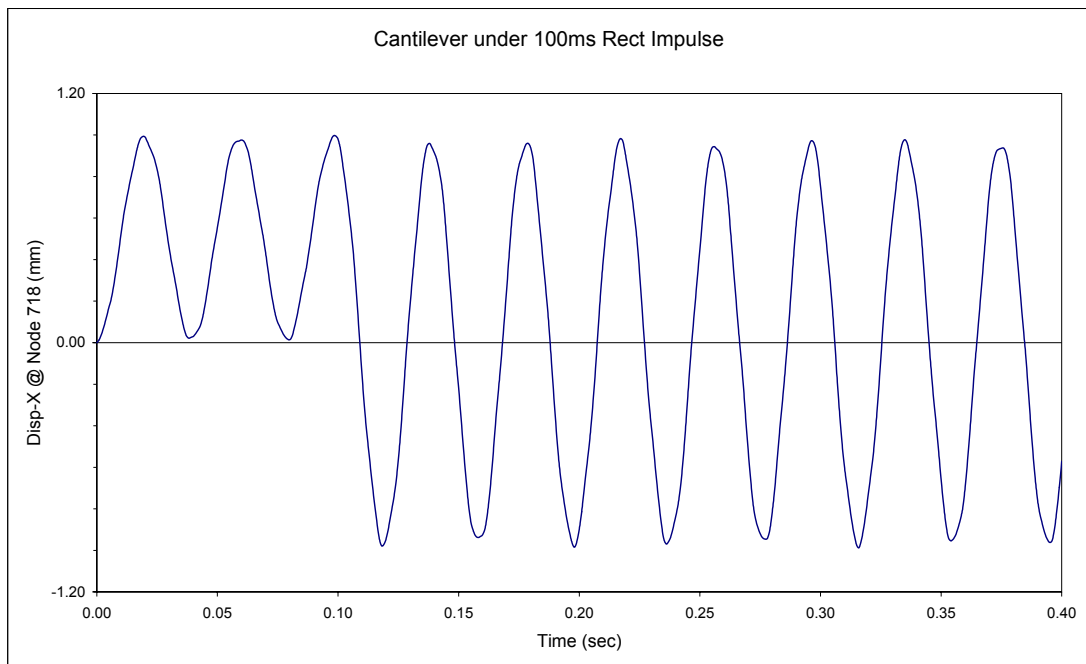
Figure 5.6   Transient Response of Cantilever Beam under Rectangular Impulse
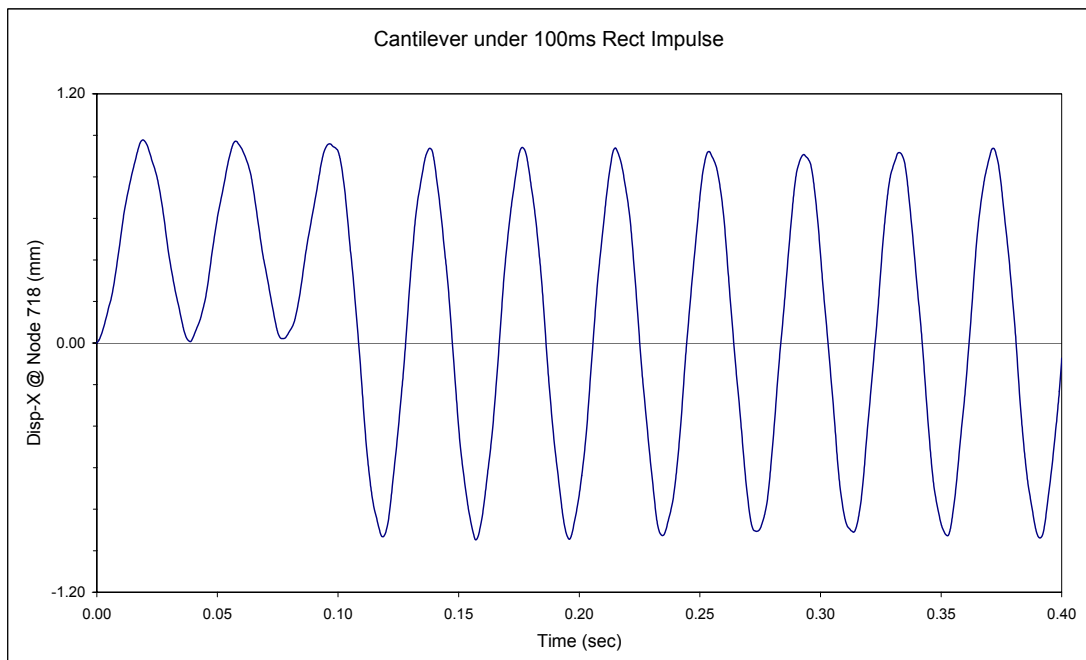(without damping, by FEM)

Figure 5.7   Transient Response of Cantilever Beam under Rectangular Impulse
(without damping, by RPIM)

5.2.4 Cantilever under Rectangular Impulse (with Damping)

Same rectangular impulse as before is applied at the cantilever end. However, structural damping is considered at this time. Both FEM and RPIM are used to solve this dynamic problem with the same damping coefficients. For FEM, the time step is fixed at $\Delta t = 2.0E-4$ sec. For RPIM, the analysis parameters are chosen as

Type of Radial Basis Function	EXP
RBF shape parameters	$\alpha_c = 0.2$
Influence domain size parameter	1.5
Integration scheme	Newmark
Newmark parameters	$\alpha = 0.5 \ \beta = 0.25$
Time step	2.0E-4 sec
Overall structural damping coefficient	0.015
Frequency corresponding to damping	157.08 rad/sec

The time-history of X-displacement at node 718 that are generated by FEM and RPIM are plotted on Figure 5.8 and Figure 5.9 respectively. By a direct comparison between these two figures, it can be concluded again that RPIM can carry out the transient dynamic analysis as accurate as FEM does.
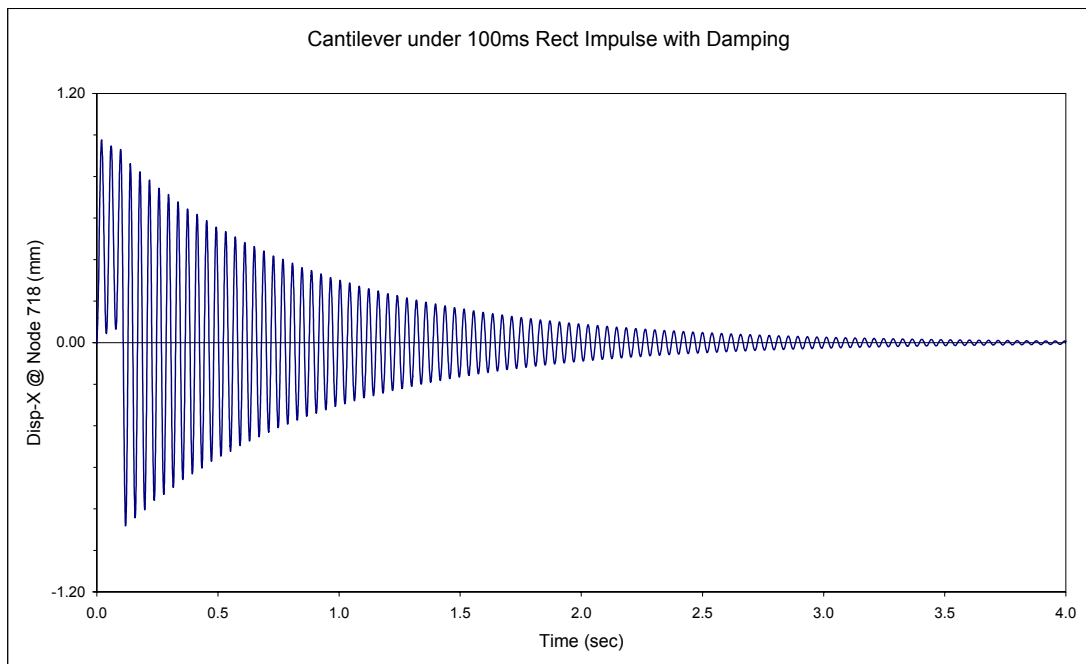
Figure 5.8   Transient Response of Cantilever Beam under Rectangular Impulse
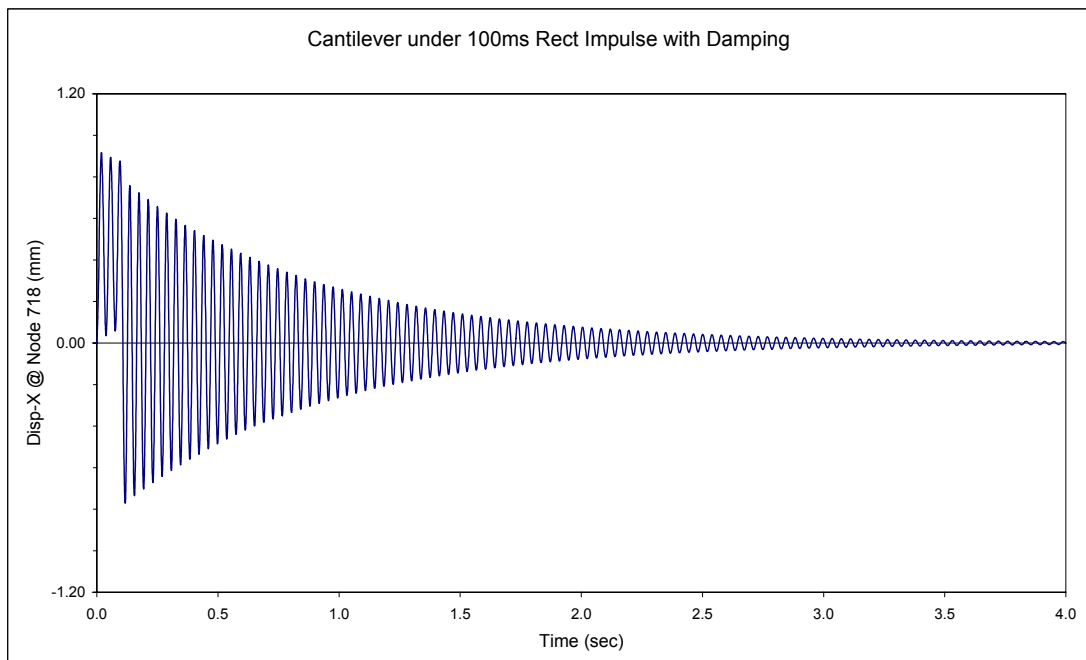(with damping, by FEM)

Figure 5.9   Transient Response of Cantilever Beam under Rectangular Impulse
(with damping, by RPIM)

5.2.5   Cantilever under Short Rectangular Impulse (without Damping)

The time-history plots shown so far are all dominated by the first mode of vibration without obvious effect of other modes. This might be attributed to the big dynamic loads we applied. By reducing the amplitude of dynamic load or shortening the duration of impulse, effect of other vibration modes may be seen clearly via RPIM.

Here, the rectangular impulse defined in Figure 5.5 is applied at the end of cantilever beam, but with very short duration of 2ms. The RPIM is used to solve this undamped dynamic problem with the setting of analysis parameters as follows:

Type of Radial Basis Function	MQ
RBF shape parameters	$\alpha_c = 1.5$ $q = 1.9$
Influence domain size parameter	1.5
Integration scheme	Newmark
Newmark parameters	$\alpha = 0.5$ $\beta = 0.25$
Time step	2.0E-5 sec

As shown in Figure 5.10, the computed time-history of X-displacement at node 718 does include the minor fluctuations caused by other vibration modes.
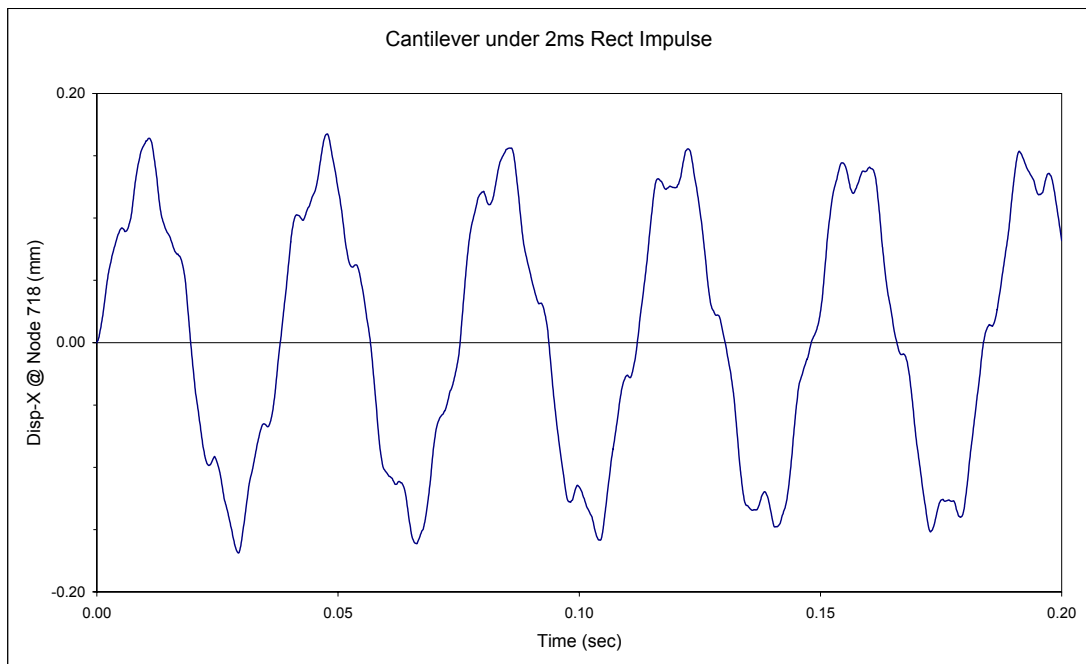
Figure 5.10   Transient Response of Cantilever Beam under Short Rectangular Impulse

(without damping, by RPIM)

Chapter 6   Numerical Examples

It has been shown in Chapter 4 & 5 that the Radial Point Interpolation Method (RPIM) can be used to solve the basic class of linear structural analysis problems in a meshless way. In this chapter, RPIM is again verified as an accurate and efficient numerical tool for structural mechanics problems through much more complex examples with more practical meaning. Moreover, an advantage of RPIM to deal with inconsistent meshes is demonstrated.

6.1 Square Plate with Center Hole

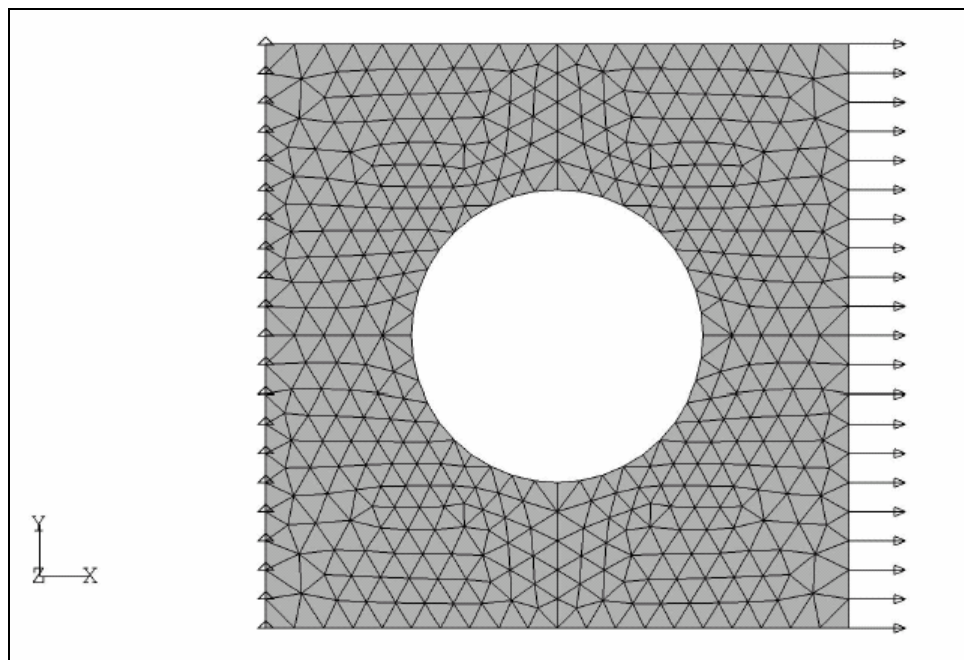A relatively simple example is shown first.

Figure 6.1   Square Plate with a Center Hole

As shown in Figure 6.1, a square plate that is made of steel is fixed along one side, and is applied with uniform distributed load on the opposite side. Nodes are generated by tetrahedral

mesher of FEMAP – the pre-processor for MSC-Nastran. RPIM is used to solve this static

problem with the setting of analysis parameters as follows:

Type of Radial Basis Function   EXP

RBF shape parameters $\alpha_c = 0.6$

Influence domain size parameter   2.7

The Figure 6.2 shows the color plot of the square plate with Von Mises stress superimposed
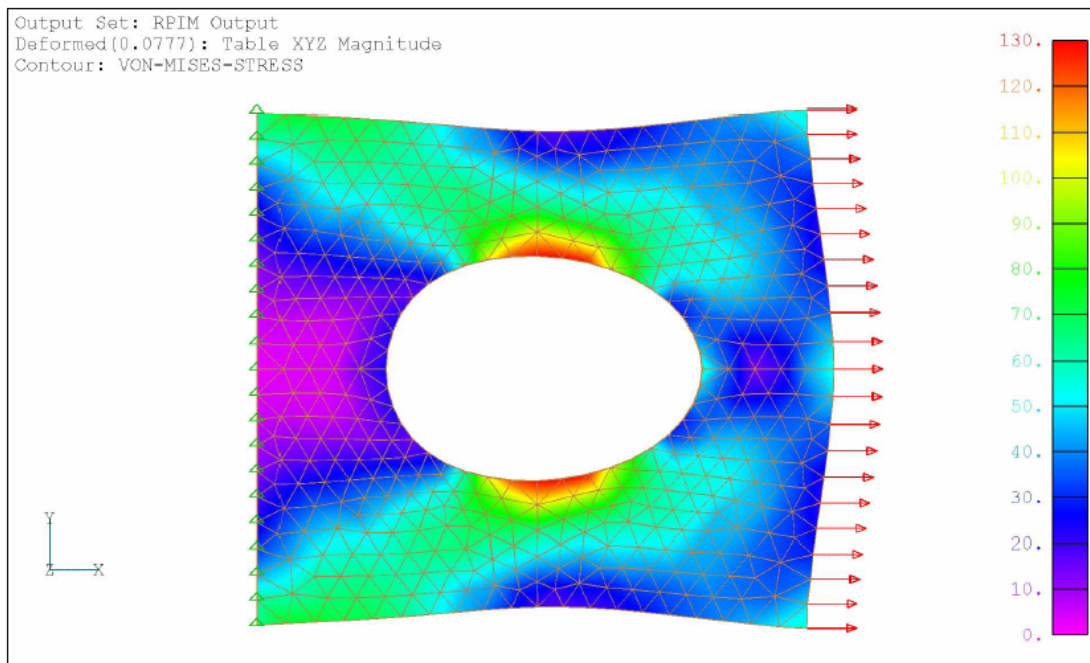
on the deflected shape.

Figure 6.2   Static Solution of Square Plate by RPIM

For comparison, MSC-Nastran is also used to generate the same plot as shown in Figure 6.3.
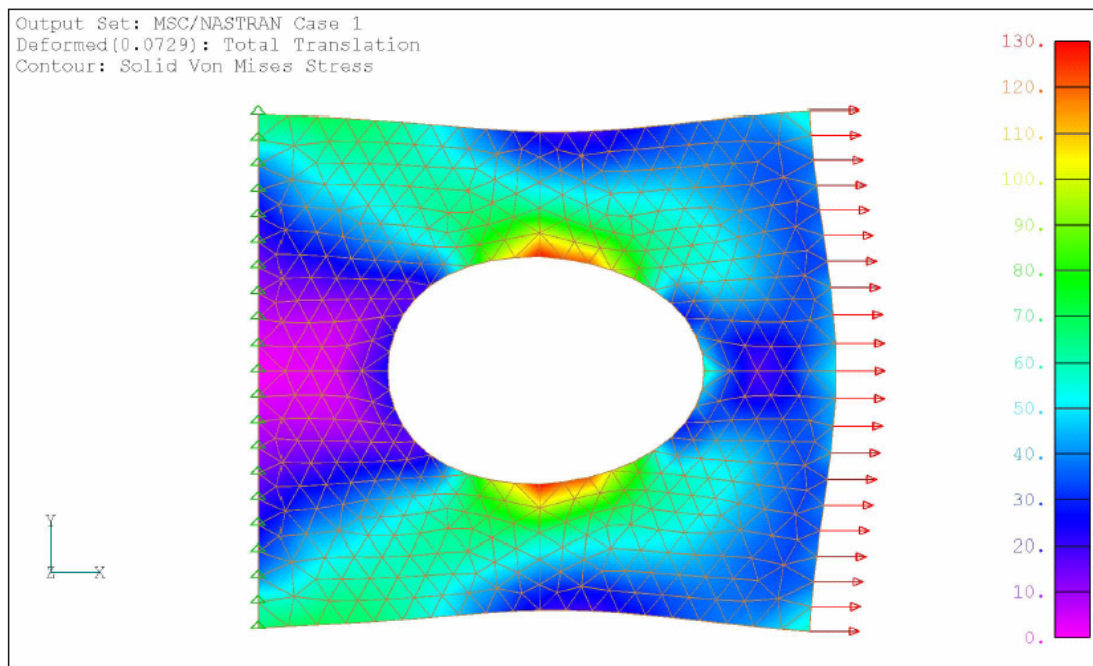
Figure 6.3 Static Solution of Square Plate by FEM

It can be seen that RPIM and FEM almost produce the identical plot of stress and deflection. Comparison numerically between these two methods is shown in Table 6.1, which indicates that RPIM gives similar results for this static problem as FEM does.

Table 6.1 Static Analysis Results of Square Plate by RPIM and FEM

	RPIM	**FEM**
Total Strain Energy	1892.0	1814.5
Maximum Deflection	0.0777	0.0729
Maximum Von Mises Stress	148.3	136.7

6.2 Riser Connector

The following example comes from a real offshore project of Floating Production and Storage Unit (FPSO). Fluid transfer between FPSO and subsea pipeline is carried out through a kind of flexible pipe called riser, which is attached to FPSO shipside by riser connector. A typical structure of riser connector is shown in Figure 6.4.
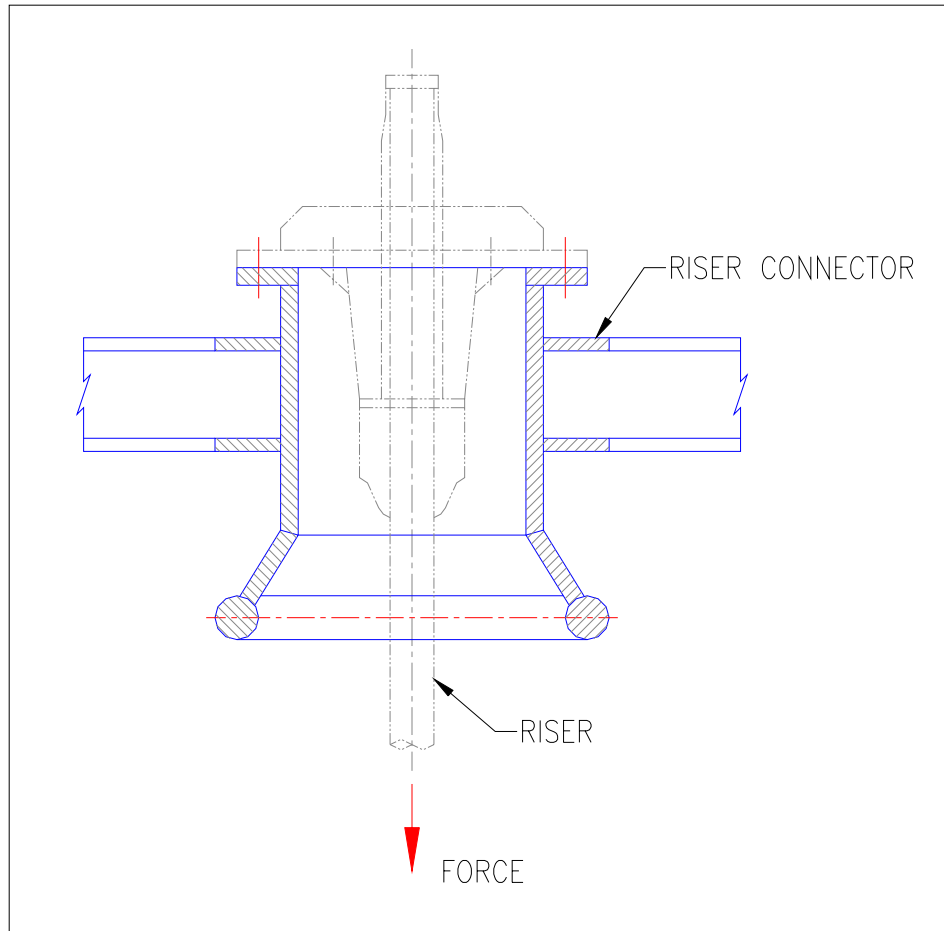
Figure 6.4 A Typical Structure of Riser Connector

A shock load on riser connector due to the emergency shut down of subsea pipeline can be simplified as a triangular impulse shown in Figure 6.5 below.
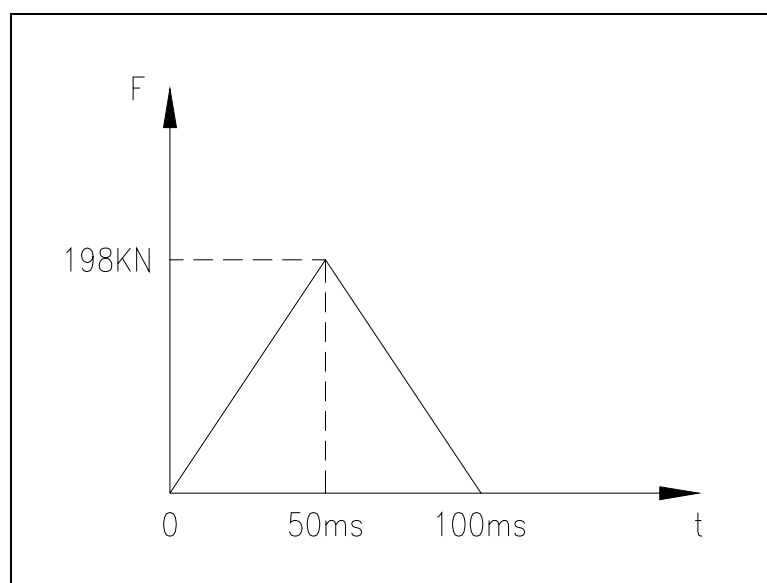

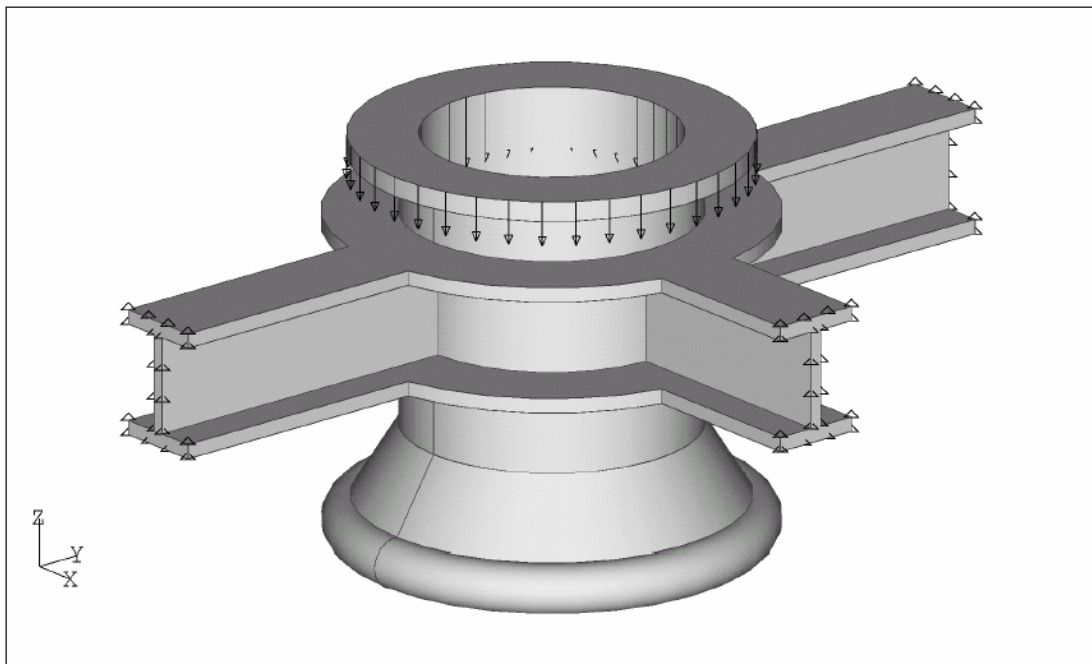**Figure 6.5** A Triangular Impulse on Riser Connector

Figure 6.6 Simplified Model of Riser Connector

The simplified model of riser connector is shown in Figure 6.6 with the shock load being applied on the top flange of riser connector. The boundary conditions are defined at the end of I-beams where riser connector is supported by other structures. This riser connector is made of steel material with Young's modulus $E = 2.0 \times 10^5$ N/mm^2, Poisson's ratio $\nu = 0.32$. The whole model is discretized into 2228 nodes via tetrahedral mesher of FEM pre-processor.

The structural behavior of riser connector is studied through the static analysis first, followed by modal analysis, and finally transient dynamic analysis.

6.2.1 Static Analysis

In this static analysis, the amplitude 198 KN of the shock load is assumed to be applied onto the riser connector statically. RPIM is used to perform this static analysis with the setting of analysis parameters as follows:

Type of Radial Basis Function   MQ

RBF shape parameters $\alpha_c = 0.5$ $q = 1.3$

Influence domain size parameter   2.7

Before the RPIM results being presented, the standard solution is obtained by MSC-Nastran

via a fine Tet-mesh with 27072 nodes. This standard solution of static analysis is plotted on

Figure 6.7, while the RPIM solution and FEM solution via coarse mesh are plotted on Figure

6.8 and Figure 6.9 respectively. It looks like that RPIM solution shown on Figure 6.8 is more

close to the standard solution shown on Figure 6.7 than FEM solution shown on Figure 6.9.

This observation is confirmed by Table 6.2, which shows the comparison of static analysis

results between RPIM and FEM. The error of RPIM solution is much less than that of FEM

solution if the same Tet-mesh pattern is used.

Table 6.2   Static Analysis Results of Riser Connector by RPIM and FEM

		MFree RPIM Coarse Mesh	MSC-Nastran Fine Mesh	MSC-Nastran Coarse Mesh
Strain Energy	N-mm	5.024E+04	5.128E+04	4.040E+04
Maximum Deflection	mm	1.041	1.034	0.755
CPU Time	Sec	589	468	39

Even though the present RPIM solver takes much longer time (589 seconds) to get the

solution than MSC-Nastran does (39 seconds) based on the same Tet-mesh, the RPIM is

much more accurate. In order for FEM to get the similar level of accuracy as RPIM, much

more nodes are necessary, thus much longer time (468 seconds) is needed. From this point of

view, the present RPIM solver is at least comparable with FEM in terms of analysis speed. As

mentioned in Section 4.3, longer computer time taken by RPIM is actually attributed to the

slow hard disk operations. If some modifications were made on the numerical method of

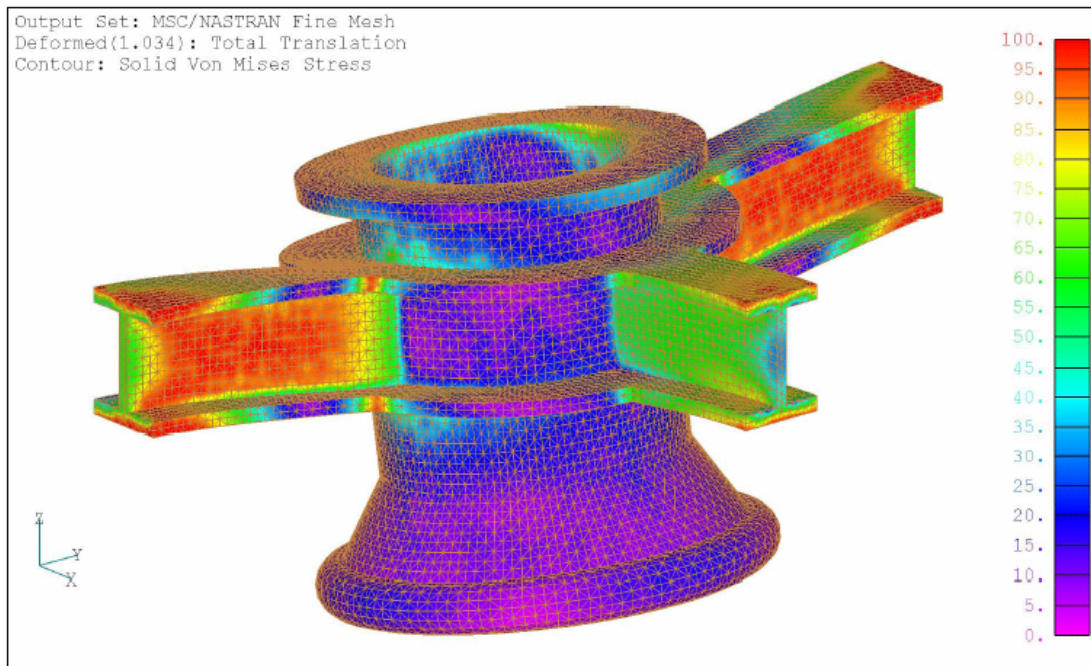RPIM, its performance could be greatly improved beyond FEM.

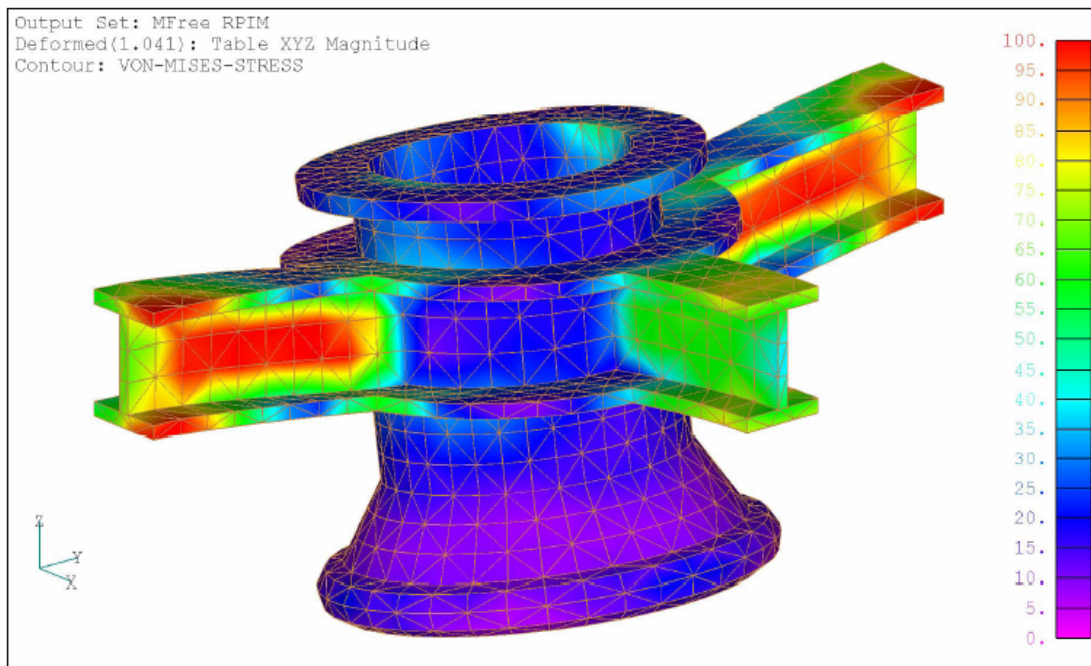**Figure 6.7**   Standard Static Solution of Riser Connector by FEM via Fine Mesh

Figure 6.8   Static Solution of Riser Connector by RPIM via Coarse Mesh
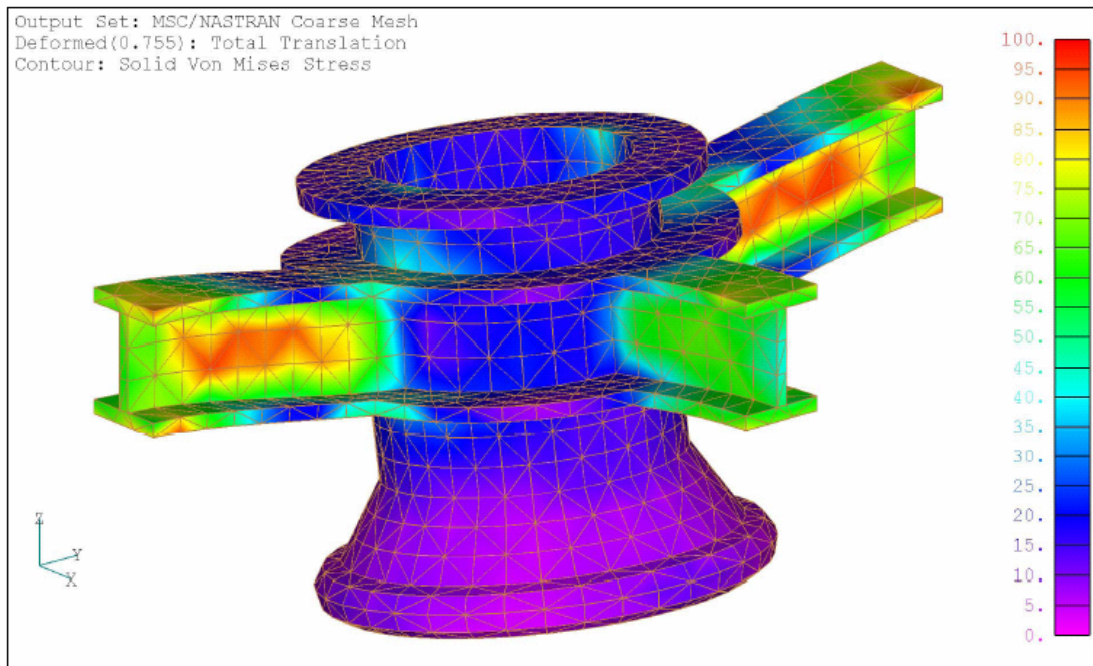
Figure 6.9   Static Solution of Riser Connector by FEM via Coarse Mesh

6.2.2 Modal Analysis

RPIM is used to perform the modal analysis for the riser connector with the setting of analysis parameters as follows:

Type of Radial Basis Function   MQ

RBF shape parameters $\alpha_c = 0.5$ $q = 1.3$

Influence domain size parameter   2.7

For comparison, the standard solution is obtained by MSC-Nastran via a fine Tet-mesh with 27072 nodes. This standard solution of modal analysis is plotted on Figure 6.10, while the RPIM solution is plotted on Figure 6.11. It can be seen from these two figures that RPIM and FEM generate similar mode shapes. The comparison of eigenvalues between RPIM and FEM is shown in Table 6.3, which also indicates that RPIM solution for modal analysis is much more accurate than that of FEM based on same Tet-mesh.
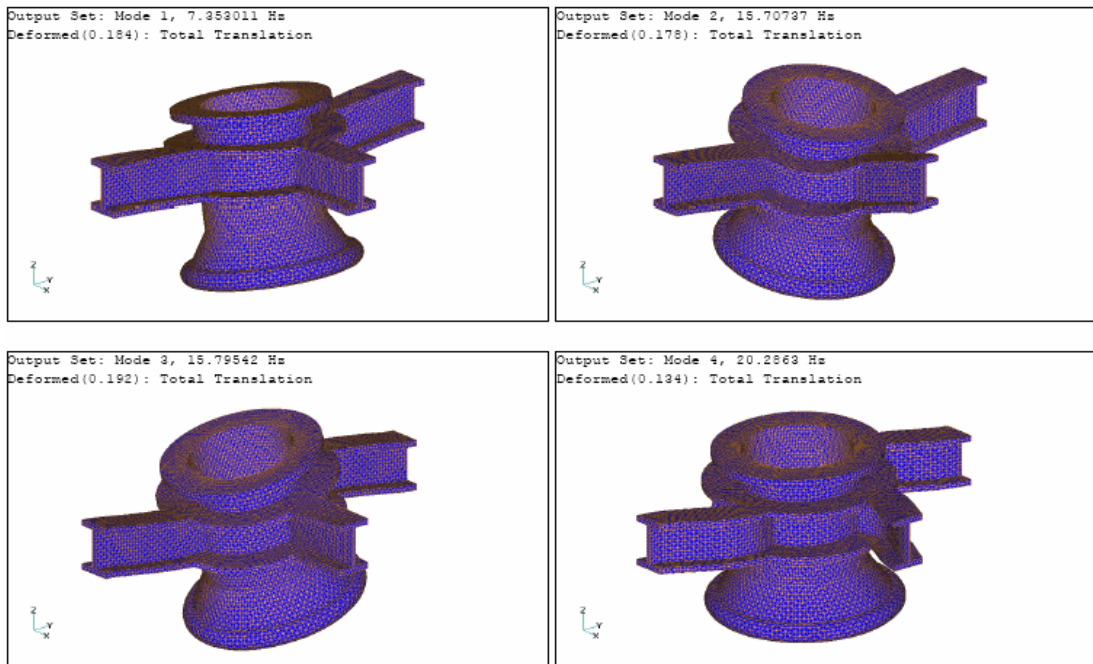
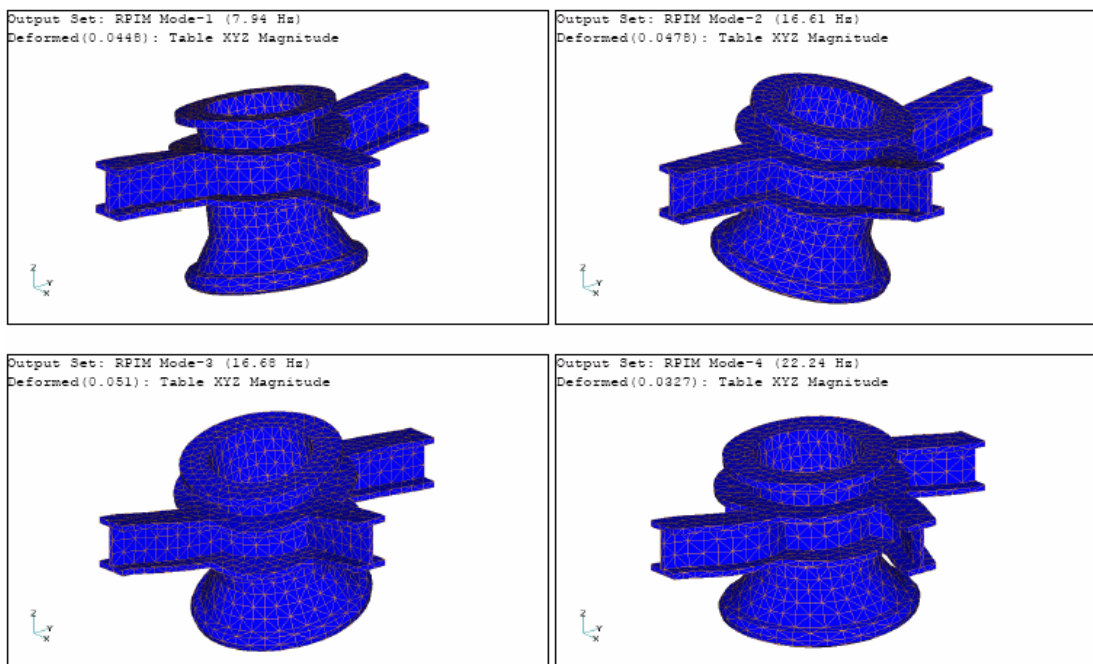**Figure 6.10**   Mode Shapes of Riser Connector by FEM via Fine Mesh

Figure 6.11   Mode Shapes of Riser Connector by RPIM via Coarse Mesh

Table 6.3 Modal Analysis Results of Riser Connector by RPIM and FEM

Mode No.		MFree RPIM Coarse Mesh	MSC-Nastran Fine Mesh	MSC-Nastran Coarse Mesh
1	Hz	7.94	7.35	8.79
2	Hz	16.61	15.71	17.45
3	Hz	16.68	15.80	17.67
4	Hz	22.24	20.29	23.65

6.2.3 Transient Dynamic Analysis

Finally, RPIM is used to perform the transient dynamic analysis for the riser connector under the triangular impulse defined by Figure 6.5. RPIM analysis parameters are chosen as

Type of Radial Basis Function	MQ
RBF shape parameters	$\alpha_c = 0.5$ $q = 1.3$
Influence domain size parameter	2.7
Integration scheme	Newmark
Newmark parameters	$\alpha = 0.5$ $\beta = 0.25$
Time step	1.0E-4 sec
Overall structural damping coefficient	0.2
Frequency corresponding to damping	62.8 rad/sec

The time-history of vertical displacement at the center of riser connector top flange is plotted on Figure 6.12, which is close to what is expected.
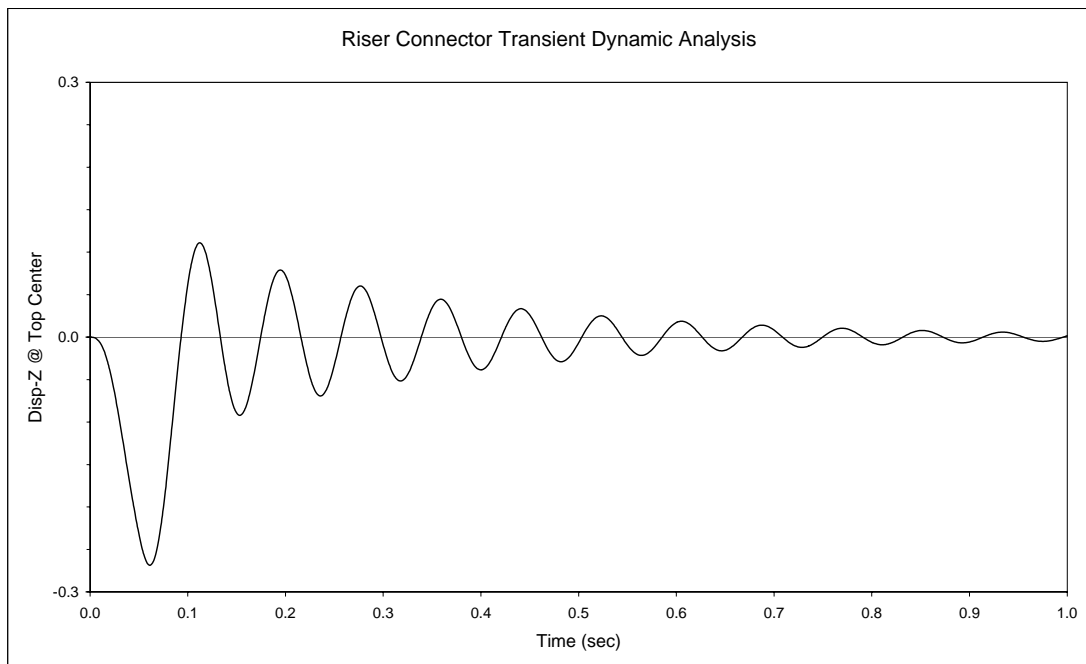
Figure 6.12   Transient Response of Riser Connector by RPIM

6.3 RPIM with Inconsistent Meshes

In FEM analysis, if a complex model is formed by several parts and meshes from different

parts do not match properly at the intersection surfaces, gaps will be contained in the model,

and serious analysis error will be caused. However, RPIM based on this kind of inconsistent

meshes can produce good results. This valuable potential of RPIM can be demonstrated in the

examples below.

6.3.1 Cantilever Beam with Inconsistent Meshes

At first, let us look at a simple, yet representative example of cantilever beam that is discussed

in Chapter 4. Here, nodes are generated in two steps, i.e. left half and right half of cantilever

beam are meshed separately, with inconsistent meshes at the middle plane. This special mesh

pattern is shown in Figure 6.13. It can be expected that FEM will produce wrong results with

very high stress concentration at the middle of cantilever beam due to inconsistent meshes.

However, RPIM with a typical setting of analysis parameters produces reasonable results as

shown in Figure 6.14. This solution satisfies all the necessary continuity and consistency requirements. The strain energy of 2940.2 N-mm obtained by RPIM based on inconsistent meshes is also close to the strain energy of 3027.8 N-mm in the standard solution.

The correct result by RPIM can be well explained by the basis of MFree methods. As described in Chapter 1, mesh is used to generate the nodes in our RPIM. In the process of formulating and solving the system equations, the mesh is not used at all. Therefore, inconsistent meshes have no effect on the RPIM results. In other words, RPIM can produce reasonable results regardless of inconsistent meshes.

6.3.2 Riser Connector with Inconsistent Meshes

The example of riser connector is used again to show that inconsistent meshes can be safely used by RPIM to produce accurate results. As shown in Figure 6.15, the model of riser connector is now made of 4 parts, whose nodes are generated separately with mesh inconsistency at their intersection surfaces. The static solution, mode shapes and transient response of this 4-part model by RPIM are shown in Figure 6.16, 6.17 and 6.18. By comparison of these figures with Figure 6.7, 6.10 and 6.12, it can be concluded that inconsistent meshes can be used to generate nodes for RPIM analysis without losing any accuracy.

This special feature of RPIM to deal with inconsistent meshes can bring us extra benefit. In solving engineering problems for industries, the three-dimensional solids are normally of complex shapes, which can be further divided into some sub-parts of simple shapes. It is a general procedure for FEM analysts to create the mesh sub-part by sub-part. Inconsistent meshes can easily happen on the interface between sub-parts, and thus a lot of time has to be spent to avoid these inconsistent meshes. On the contrary, we need not to worry about these inconsistent meshes at all if RPIM is used. As a result, the efficiency of our analysis works can be greatly improved.
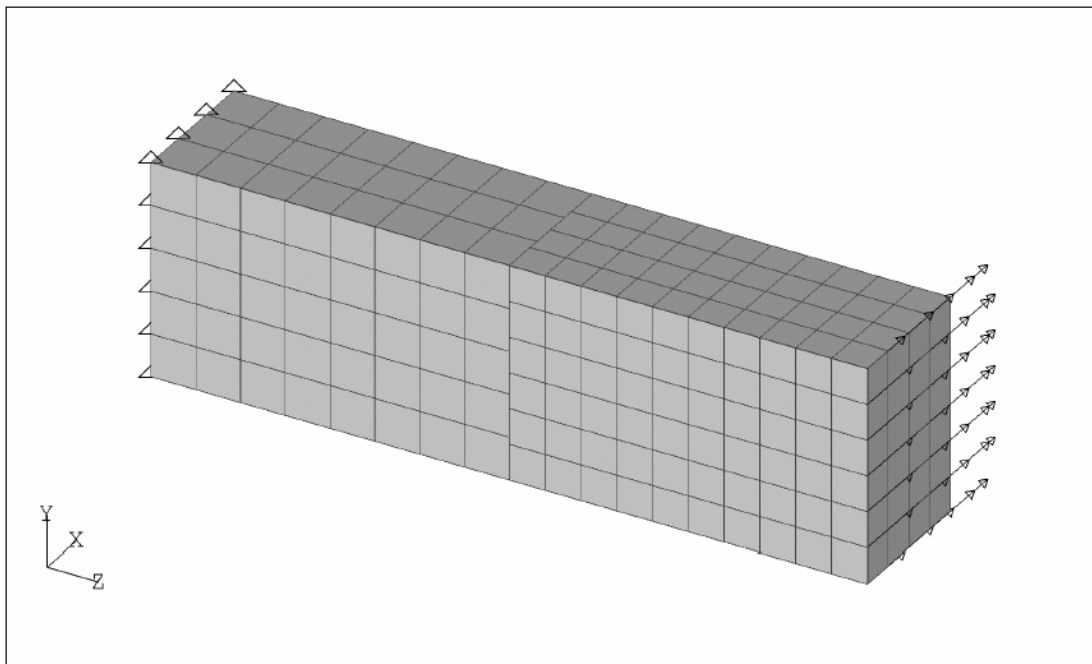
Figure 6.13 Cantilever Beam with Inconsistent Meshes at Middle Plane
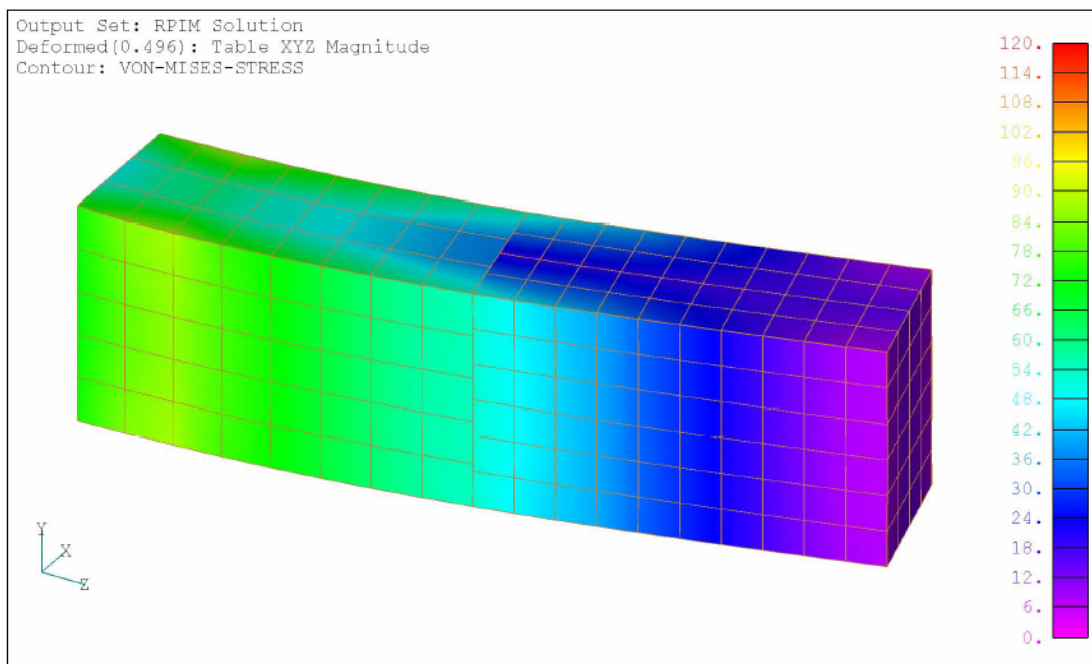

Figure 6.14 Static Solution of Cantilever Beam by RPIM via Inconsistent Meshes
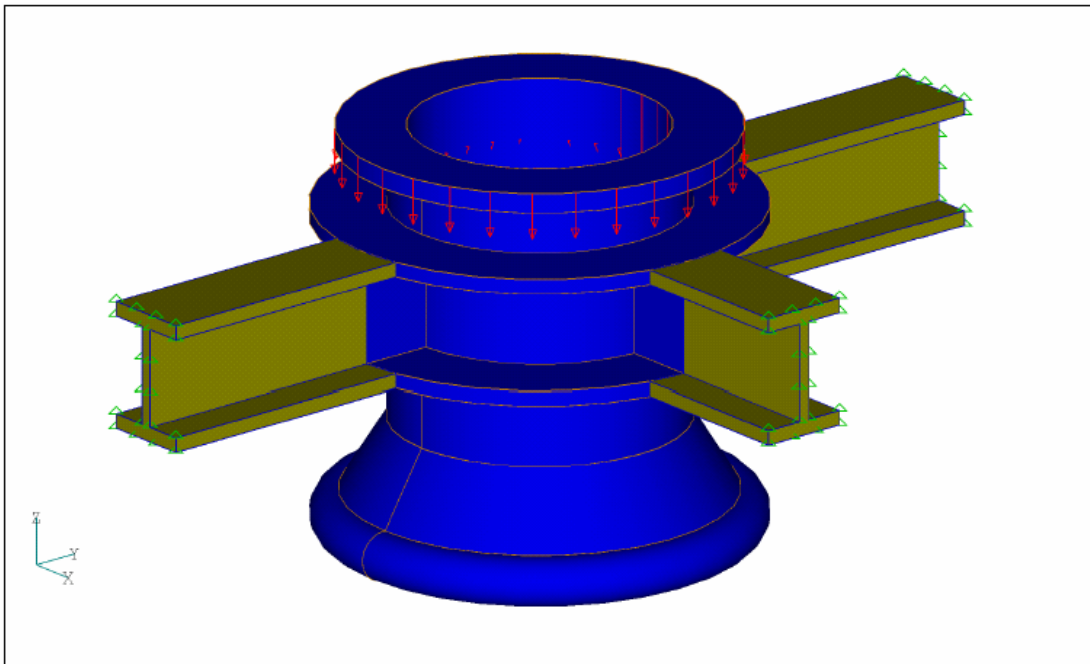
Figure 6.15 4-Part Model of Riser Connector
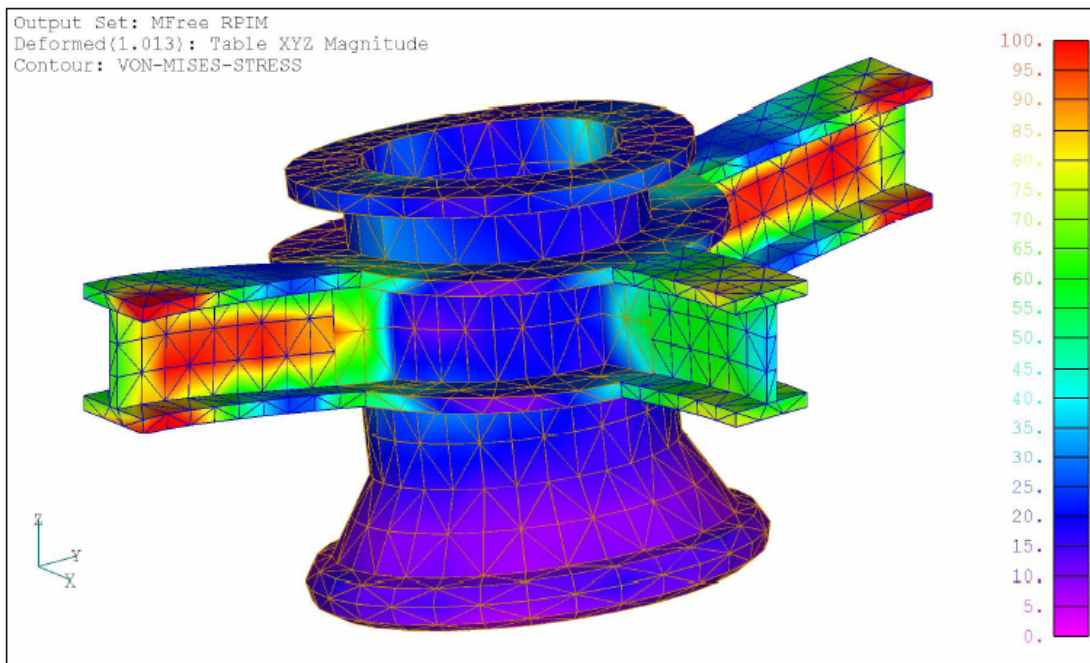
Figure 6.16 Static Solution of Riser Connector by RPIM via Inconsistent Meshes

Output Set: RPIM Mode-1 (7.83 Hz)
Deformed(0.0549): Table XYZ Magnitude

Output Set: RPIM Mode-2 (16.68 Hz)
Deformed(0.0539): Table XYZ Magnitude

Output Set: RPIM Mode-3 (16.87 Hz)
Deformed(0.0564): Table XYZ Magnitude

Output Set: RPIM Mode-4 (22.38 Hz)
Deformed(0.0379): Table XYZ Magnitude

Figure 6.17   Mode Shapes of Riser Connector by RPIM via Inconsistent Meshes

Figure 6.18   Transient Response of Riser Connector by RPIM via Inconsistent Meshes

Chapter 7   Conclusions and Future Study

7.1 Concluding Remarks

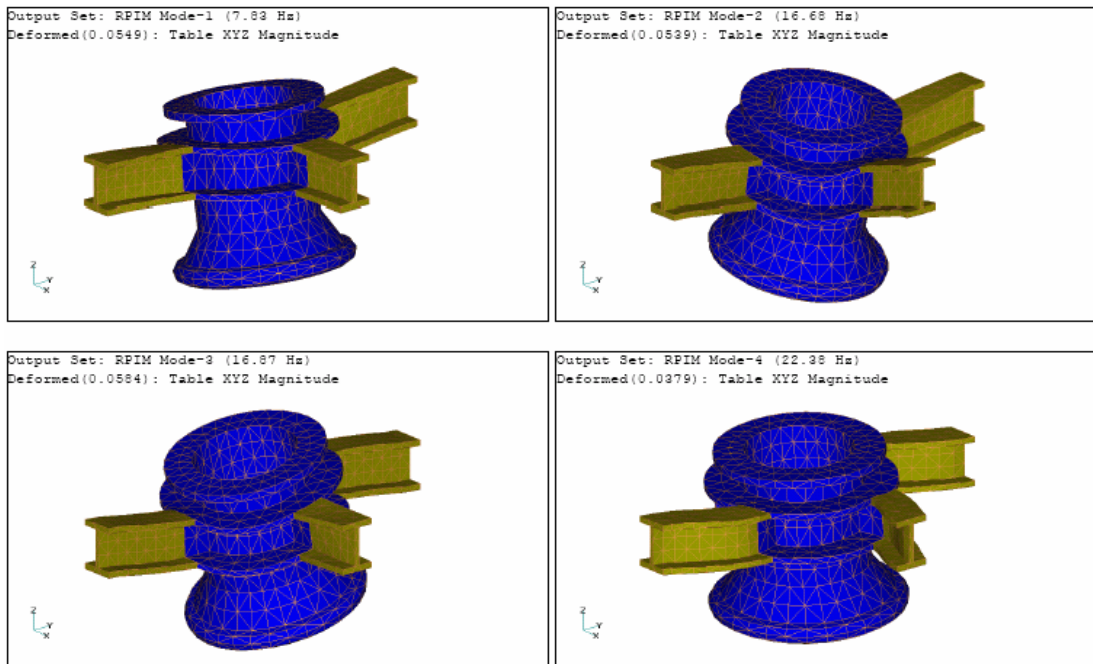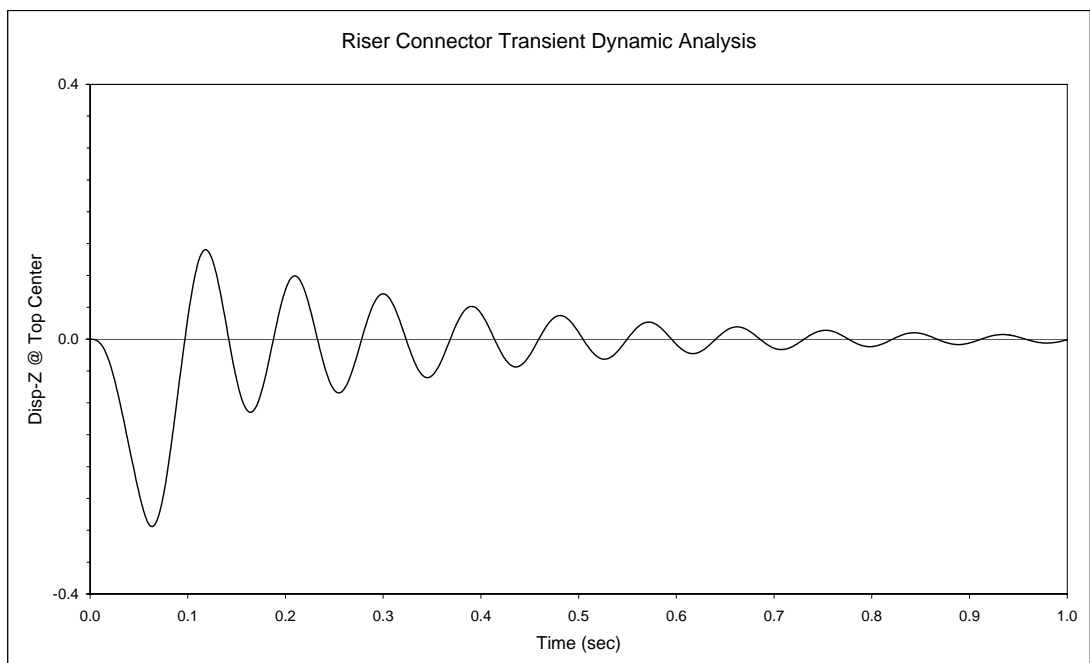This research project focuses on the development of Radial Point Interpolation Method (RPIM) for 3D solids. The RPIM procedure is coded using Fortran language and is complied as a fast and robust solver for the basic class of linear structural analysis problems in three-dimension. It is verified as an efficient and accurate numerical tool for 3D solid mechanics via its application to some analysis examples. Through these studies, the following conclusions can be drawn.

- The Point Interpolation Method (PIM) using radial-polynomial basis is formulated and proved to be accurate in constructing the MFree shape functions with the Kronecker delta function property. The RPIM is numerically stable for both regular and irregular nodal distributions. Through the example of 3-D function fitting, it is shown that radial basis functions of EXP and MQ could be used in the RPIM formation to produce good fitting quality, as long as the preferred ranges of shape parameters are used in the interpolation.

- RPIM shape functions are employed together with the Galerkin weak form to formulate the analysis method for 3D solid mechanics. Procedures to perform the linear static analysis, modal analysis and transient dynamic analysis for 3D solids are developed in detail. These procedures are coded numerically using Fortran language and are complied as an analysis solver for 3D solid mechanics.

- The accuracy and efficiency of the RPIM solver are firstly investigated through the static analysis of 3D solids, via patch test and a benchmark example of cantilever beam. It is found that various analysis parameters will affect the performance of RPIM to some

extent. By a complete parametric study of all these factors, the preferred ranges of different analysis parameters are recommended as follows:

Shape parameters for EXP $\qquad$ $\alpha_c = 0.2 \sim 1.0$

Shape parameters for MQ $\qquad$ $\alpha_c = 0.5 \sim 2.0$, $q = 0.4 \sim 2.2$ except integers

Influence domain size parameter $\qquad$ 1.5 for Hex-mesh and 2.7 for Tet-mesh

Number of Gauss points $\qquad$ 8 for Hex-element and 4 for Tet-element

By use of analysis parameters within the preferred ranges shown above, RPIM can produce analysis solutions with accuracy and efficiency comparable or better, in some cases, than FEM.

- The excellent performance of RPIM is then demonstrated again through the modal analysis and transient dynamic analysis of 3D solids, via the same benchmark example of cantilever beam. The Newmark method (constant-average acceleration method) is recommended for the various kinds of transient dynamic analysis after a comparison study among several direct integration schemes.

- Finally, the RPIM is shown to be of practical use through much more complex examples from industries. By the way, an advantage of RPIM to deal with inconsistent meshes is demonstrated.

In conclusion, RPIM has better computational performance over FEM on the structural analysis of 3D solids, in terms of accuracy, efficiency and convenience.

7.2 Recommendations for Future Study

It should be noted that 3D-RPIM is still under development and its potential has not yet been explored fully. There is much room for improvement on the following areas:

- Modification can be made on the numerical implementation of RPIM so as to make full use of computer resources and thus improve the analysis efficiency further.

- RPIM solver for 1D and 2D structures can be incorporated into the 3D-RPIM solver so that the combined RPIM solver can be used for problems with mixed dimensionality (solids, shells and beams in a single model).

- RPIM shape functions can be used with other energy principles, such as constrained Galerkin weak form or local Petrov-Galerkin weak form, to formulate new varieties of RPIM for 3D solids.

- One of the distinctive features of MFree methods is that they evaluate the field variables entirely based on a group of discrete nodes and require no predefined nodal connectivity. This is particularly suitable for adaptive analysis. Therefore, the adaptive scheme can also be incorporated into the 3D-RPIM formulation so that nodes may be moved, inserted and deleted freely during the analysis to capture the stress concentration automatically.

- Having successfully implemented the RPIM on the basic class of linear structural analysis problems in three-dimension, the application of 3D-RPIM can be extended to the advanced class of structural analysis, such as nonlinear analysis, contact analysis and etc.

- RPIM can be used to simulate other physical phenomena in three-dimension, such as heat flux, fluid flow, seepage and etc.

References

Atluri, S.N. and Zhu, T., A new meshless local Petrov-Galerkin (MLPG) approach in computational mechanics, Comput. Mech., 22, 117-127, 1998.

Belytschko, T., Lu, Y.Y. and Gu, L., Element-free Galerkin methods, Int. J. Numer. Methods Eng., 37, 229-256, 1994.

Chen, X.L., Liu, G.R. and Lim, S.P., An Element Free Galerkin Method for the Free Vibration Analysis of Composite Laminates of Complicated Shape, Compos. Struct. 59 (2), pp.279-289, Feb 2003.

Dai, K.Y., Liu, G.R., Lim, K.M. and Gu, Y.T., Comparison between the Radial Point Interpolation and the Kriging Interpolation used in Meshfree Methods, Computational Mechanics, 32 (1-2), pp.60-70, 2003.

Dai, K.Y., Liu, G.R., Lim, K.M. and Chen, X.L., A Mesh-Free Method for Static and Free Vibration Analysis of Shear Deformable Laminated Composite Plates. Journal of Sound and Vibration, 269 (3-5), pp.633-652, 2004.

Dai, K.Y., Liu, G.R., Lim, K.M., Han, X. and Du S.Y., A Meshfree Radial Point Interpolation Method for Analysis of Functionally Graded Material (FGM) Plates. Computational Mechanics, 34 (3), pp.213-223, 2004.

Gingold, R.A. and Monaghan, J.J., Smooth particle hydrodynamics: theory and applications to non-spherical stars, Mon. Not. R. Astron. Soc., 181, 375-389, 1977.

Gu, Y.T. and Liu, G.R., A Meshless Local Petrov-Galerkin (MLPG) Method for Free and Forced Vibration Analyses for Solids. Computational Mechanics 27 (2001) 3, pp.188-198.

Gu Y.T. and Liu G.R., A Coupled Element Free Galerkin / Boundary Element Method for Stress Analysis of Two-Dimension Solid. Computer Methods in Applied Mechanics and Engineering, Vol.190 (34), pp.4405-4419, 2001.

Gu, Y.T. and Liu, G.R., A Local Point Interpolation Method (LPIM) for Static and Dynamic Analysis of Thin Beams. Computer Methods in Applied Mechanics and Engineering, Vol.190, 2001, pp.5515-5528.

Gu, Y.T. and Liu, G.R., A Meshless Local Petrov-Galerkin (MLPG) Formulation for Static and Free Vibration Analyses of Thin Plates. Computer Modeling in Engineering & Sciences, 2(4), 2001, pp.463-476.

Gu, Y.T., Development of Meshfree Techniques for Computational Mechanics. Ph.D Thesis, National University of Singapore 2002

Gu, Y.T. and Liu, G.R., A Boundary Radial Point Interpolation Method (BRPIM) for 2-D Structural Analyses. Structural Engineering and Mechanics, 15 (5), pp.535-550, May 2003.

Gu, Y.T. and Liu, G.R., Hybrid Boundary Point Interpolation Methods and their Coupling with the Element Free Galerkin Method, 27 (9), pp.905-917, 2003.

Gu, Y.T. and Liu, G.R., A Meshfree Weak-Strong (MWS) Form Method for Time Dependent Problems. Computational Mechanics, 35 (2), pp.134-145, 2005.

Reddy, J.N., An Introduction to the Finite Element Method, Second Edition. McGraw Hill 1993

Liu, G.R. and Gu, Y.T., A Local Point Interpolation Method for Stress Analysis of Two-Dimensional Solids. Structural Engineering and Mechanics, Vol.11, No.2, 2001, pp.221-236.

Liu, G.R. and Gu, Y.T., A Point Interpolation Method for Two-Dimensional Solids. Int. J. Num. Methods in Engrg. Vol.50, 2001, pp.937-951.

Liu, G.R. and Chen, X.L., A Mesh Free Method for Static and Free Vibration Analyses of Thin Plates of Complicated Shape. Journal of Sound and Vibration, 241 (5) 2001, pp.839-855.

Liu, G.R. and Gu, Y.T., A Local Radial Point Interpolation Method (LRPIM) for Free Vibration Analyses of 2-D Solids, Journal of Sound and Vibration, (2001) 246 (1), pp.29-46.

Liu, G.R. and Gu, Y.T., Comparisons of Two Meshfree Local Point Interpolation Methods for Structural Analyses. Computational Mechanics, 29(2), 2002, pp.107-121.

Liu, G.R. and Chen, X.L., Buckling of Symmetrically Laminated Composite Plates using the Element-Free Galerkin Method. International Journal of Structural Stability and Dynamics, 2(3), 2002, pp.281-294.

Liu, G.R. and Tu, Z.H., An Adaptive Procedure based on Background Cells for Meshless Methods. Computer Methods in Applied Mechanics and Engineering, 191, 2002, pp.1923-1943.

Liu, G.R., Dai, K.Y., Lim, K.M. and Gu Y.T., A Point Interpolation Mesh Free Method for Static and Frequency Analysis of Two-Dimensional Piezoelectric Structures. Comput. Mech. 29 (6), pp.510-519, Nov 2002.

Liu, G.R., Yan L., Wang J.G., et al., Point Interpolation Method based on Local Residual Formulation using Radial Basis Functions. Struct. Eng. Mech. 14 (6) pp.713-732, Dec 2002.

Liu, G.R., Dai, K.Y., Lim K.M. and Gu Y.T., A Radial Point Interpolation Method for Simulation of Two-Dimensional Piezoelectric Structures. Smart Materials and Structures, 12, pp.171-180, 2003.

Liu, G.R. and Gu, Y.T., A Matrix Triangularization Algorithm for the Polynomial Point Interpolation Method. Computer Methods in Applied Mechanics and Engineering, 192 (19), pp.2269-2295, 2003.

Liu, G.R. and Gu, Y.T., A Meshfree Method: Meshfree Weak-Strong (MWS) Form Method for 2-D Solids. Computational Mechanics, 33 (1), pp.2-14, 2003.

Liu, G.R., Mesh Free Methods, Moving beyond the Finite Element Method. CRC Press 2003

Liu, G.R., Wu, Y.L. and Ding, H., Meshfree Weak-Strong (MWS) Form Method and its Application to Imcompressible Flow Problems. International Journal for Numerical Methods in Fluids, 46, pp.1025-1047, 2004.

Liu, G.R. and Gu Y.T., Boundary Meshfree Methods based on the Boundary Point Interpolation Methods. Engineering Analysis with Boundary Elements, 28 (5), pp.475-487, 2004.

Liu, G.R., Zhang, G.Y., Gu, Y.T. and Wang, Y.Y., A Meshfree Radial Point Interpolation Method (RPIM) for Three-Dimensional Solids, Computational Mechanics, 36(6), pp.421-430, 2005.

Liu, G.R., Zhang, G.Y., Dai, K.Y., Wang, Y.Y., Zhong, Z.H., Li, G.Y. and Han, X., A Linearly Conforming Point Interpolation Method (LC-PIM) for 2D Solid Mechanics Problems, International Journal of Computational Methods, 2(4), pp.645-665, 2005.

Liu L., Liu G.R. and Tan V.B.C., Element Free Method for Static and Free Vibration Analysis of Spatial Thin Shell Structures. Computer Methods in Applied Mechanics and Engineering, 191, pp.5923-5942, 2002.

Liu, M.B., Liu, G.R. and Lam, K.M., A One-Dimensional Meshfree Particle Formulation for Simulating Shock Waves. Shock Waves, 13 (3), pp.201-211, 2003.

Liu, M.B., Liu, G.R., Lam, K.Y. and Zong, Z., Computer Simulation of Shaped Charge Detonation using Meshless Particle Method. International Journal for Blasting and Fragmentation, 7 (3), pp.181-202, 2003.

Lucy, L., A numerical approach to testing the fission hypothesis, Astron. J., 82, 1013-1024, 1977.

Nayroles, B., Touzot, G. and Villon, P., Generalizing the finite element method: diffuse approximation and diffuse elements, Comput. Mech., 10, 307-318, 1992.

Wang, J.G., Liu, G.R. and Wu Y.G., A Point Interpolation Method for Simulating Dissipation Process of Consolidation. Computer Methods in Applied Mechanics and Engineering, Vol.190, 2001, pp.5907-5922.

Wang, J.G. and Liu, G.R., A Point Interpolation Meshless Method based on Radial Basis Functions. International Journal for Numerical Methods in Engineering, 54, 2002, pp.1623-1648.

Wang, J.G. and Liu, G.R., On the Optimal Shape Parameters of Radial Basis Functions used for 2-D Meshless Methods. Computer Methods in Applied Mechanics and Engineering, 191, 2002, pp.2611-2630.

Wang, J.G., Liu, G.R. and Lin, P., Numerical Analysis of Biot's Consolidation Process by Radial Point Interpolation Method. International Journal of Solids and Structures 39(6), 2002, pp.1557-1573.

Wu, Y.L. and Liu, G.R., A Meshfree Formulation of Local Radial Point Interpolation Method (LRPIM) for Incompressible Flow Simulation. Computational Mechanics, 30 (5-6), pp.355-365, 2003.

Tirupathi R. Chandrupatla and Ashok D. Belegundu, Introduction to Finite Elements in Engineering, Third Edition. Prentice Hall 2002.